Title

Triangular Cross-Section Photonics in 4H-Silicon Carbide for Quantum Information Processing

Author

Majety, Sridhar

Publication Date

2024

Triangular Cross-Section Photonics in 4H-Silicon Carbide for Quantum Information Processing

By

SRIDHAR MAJETY

DISSERTATION

Submitted in partial satisfaction of the requirements for the degree of

DOCTOR OF PHILOSOPHY

in

Electrical and Computer Engineering

in the

OFFICE OF GRADUATE STUDIES
of the

UNIVERSITY OF CALIFORNIA

DAVIS

Approved:

Marina Radulaski, Chair

S. J. Ben Yoo

Saif Islam

Committee in Charge

2024

Abstract

Defects in wide bandgap semiconductors, known as color centers, are prominent candidates for solid-state quantum technologies due to their attractive properties, including near identical single photon emissions, optical interfacing, long coherence times, and scalability potential. Among the available host materials, silicon carbide (SiC) is desirable for its quantum-grade wafer availability and advanced processing capabilities. To realize the full potential of the color centers in SiC, the efficiencies of emission, collection and detection of the single photons need to significantly enhance compared to those values in bulk. This enhancement can be achieved through photonic integration of color centers, which increases the light-matter interaction. Challenges in maintaining the pristine quality of color centers have led to photonic integration moving away from the established nanofabrication processes and toward alternative approaches that require non-standard sample preparation and lack scalability. Bulk processing techniques such as the Faraday cage-assisted angle etching and ion beam etching produce suspended photonic structures with triangular cross-section. Ion beam etching has been used to illustrate a wafer-scale process in diamond, leading to significant advancements in quantum information processing experiments. However, a similar wafer-scale etching process is currently unavailable in SiC, and there is limited understanding of the behavior of light in these novel triangular photonics.

This dissertation presents the development of novel, wafer-scale, triangular cross-section photonics for color centers in SiC suitable for quantum information processing applications, studied through modeling, nanofabrication, and 4f confocal spectroscopy. This includes modeling efficient photonic devices such as waveguides, photonic crystal mirrors and nanopillars for improving collection efficiencies, photonic crystal cavities for enhancing the single photon emission, photonic molecule appropriate for studying cavity quantum electrodynamics systems, and superconducting nanowire single photon detectors integrated with waveguides for efficient detection of color center emission. Next, we develop a nanofabrication process to generate and integrate nitrogen vacancy centers in 4H-SiC into nanopillars for the first time and confirmed the enhancement in collection efficiency through 4f confocal spectroscopy. As a crowning achievement of this effort, we develop a novel wafer-scale ion beam etching process to fabricate triangular cross-section photonics in 4H-SiC, that does not interfere with the integrated color center emission properties.

Acknowledgements

Firstly, I extend my heartfelt gratitude to my supervisor, Marina Radulaski, for providing me the invaluable opportunity to work with her as her first PhD student. Her unwavering optimism and passion for the field served as a constant source of motivation during my PhD journey. Her steadfast support played an instrumental role in realizing my research objectives, providing access to cutting-edge facilities, fostering domestic and international collaborations and encouraging conference attendance. These experiences have profoundly contributed to my development both as a researcher and as an individual.

I am very grateful to all the members of the Molecular Foundry community at the Lawrence Berkeley National Laboratory especially Scott Dhuey and Selven Virasawmy from the Nanofabrication facility and Tevye Kuykendall from the Inorganic Nanostructures facilty for offering their technical expertise and invaluable contributions to my nanofabrication efforts. I am thankful to Ryan Anderson, Vishal Narang and other staff members at the UC Davis Center for Nano-MicroManufacturing (CNM2) for their unwavering assistance in my pursuit of achieving wafer-scale etching in SiC using the Intlvac Nanoquest II.

I would like to thank my international collaborators: Jörg Wrachtrup, Florian Kaiser (University of Stuttgart, Germany) and their group members Charles Babin, Marcel Krumrein, Jonathan Körber for collaboration on the 4H-SiC triangular cross-section devices; Jonathan J Finley, Kai Müller (Technical University of Munich, Germany) and their group members Stefan Strohauer, Fabian Wietschorke, Rasmus Flaschmann, Lucio Zugliani for collaboration on integrating superconducting nanowire single photon detectors on 4H-SiC.

I am thankful to my group members for being exceptional teammates and researchers. It was an incredible experience building a new research lab together and I learned a lot from each one of them. Working with Victoria Norman on free-space optics and cryogenics while building our initial 4f-confocal microscopy setup was both enjoyable and enlightening. Pranta Saha offered great inputs and ideas in developing our FDTD triangular photonic models, alongside being a great friend with whom I had insightful conversations. Collaborating with Alex Rubin has been a fantastic learning experience, and he has significantly boosted our experimental efforts. Mentoring talented undergraduate students like Liang Li, Miranda Bell, and Zbynka Kekula was highly rewarding, as they made significant contributions to our photonic modeling efforts.

I consider myself fortunate to have formed wonderful friends during my time in Davis. I had enriching scientific and philosophical conversations with Bharadwaj Nandakumar and enjoyed exploring Davis area with Anshuman and Jugal. My roommates, Prudhvi and Surya, created a positive and joyous atmosphere that helped me unwind from all the ups and downs during these years.

I am forever indebted to my parents and my lovely wife, Shravya, who supported all my careers decisions and have been an anchor in this long journey. I am blessed to have a strong group of friends Prajit Reddy, Harith Shantan, Praneeth Chakravarthula, Krishna Vamsi, Dolar, Hemant Ghadi, Kalyan, Vivek, Naveen, Gopi, Teja, Rahul, Kuladeep, Shashank, my undergraduate friends - Sai Kumar, Saideep, Pradeep Kumar Reddy, Manoj, Siva, Pavan, Vijayendra, and many others, who have continuously inspired and supported me.

Contents

List of Figures

Chapter 1

Introduction

Quantum mechanical effects such as superposition and entanglement open the doors to novel quantum information processing (QIP) technologies in communication, computation, sensing, and metrology, that are hard or impossible to build using conventional classical technologies. Several implementations of QIP technologies have been demonstrated, such as superconducting qubits, which leverage the quantum behavior of superconducting Josephson junctions [1–3], trapped ions in electromagnetic fields [4–6], topological qubits, which rely on exotic states of matter [7–9], and linear quantum computing using photons [10]. Solid-state systems with optically-addressable spin states (quantum dots and crystal defects) capable of emitting single photons have gained a lot of attention recently. They possess a great combination of solid-state spins as memory qubit for extending coherence times and photons as flying qubits for carrying the quantum information. Moreover, solid-state systems offer on-chip integration and scalability.

1.1 Motivation

For the purposes of QIP, one of the primary requirements is the ability of a single photon emitter to generate indistinguishable photons that can be mutually entangled. Notable strides have been made using quantum dots for this purpose [11, 12]; however, the significant variability in the emission wavelengths (with the quantum dot size, charge, and temperature) has been challenging to overcome in a scalable fashion. On the other hand, color centers, which are point defects in wide bandgap semiconductors that behave like quasi-atoms, have nearly identical and well reproducible properties.

Color center platforms have not yet realized their full QIP potential. Several remarkable demonstrations have been made in this regard, such as spin-photon entanglement [13], remote entanglement of solid-state spins separated by 1.3 km [14], a multinode quantum network [15], implementation of fault-tolerant operation of a logical qubit [16], memory-enhanced quantum communication [17], and a quantum register that uses nine nuclear spins coupled to a single electron spin, with quantum memory nearing one minute [18]. Most of these demonstrations were made using the nitrogen-vacancy center in diamond, which has defined the color center field that is now populated by a variety of quantum emitters with complementary or advanced properties. Color centers in silicon carbide (SiC) have gained a lot of interest for their long spin coherence times and emission wavelengths in the near-infrared and telecommunication bands, suitable for sending in the existing fiber optic cable network. Moreover SiC is attractive as a host material because of its mature nanofabrication, availability as wafers, and compatibility with CMOS processes.

Among the variety of color centers available in 4H-SiC, nitrogen vacancy (NV) centers [19–22] and vanadium impurities [23, 24] have emission wavelengths in the telecommunication wavelengths range, making their photons suitable for long-distance transmission over existing fiber network with minimal losses. However, most of the QIP demonstrations in SiC utilize silicon vacancy centers [25–29] and divacancy centers [30–32], with studies involving NV centers primarily conducted in bulk [33–37]. Further research is required in the nanophotonic integration of NV centers and vanadium impurities in 4H-SiC to leverage the fiber-friendly emission wavelengths of these color centers.

The implementation of large-scale QIP technologies using color centers require efficient emission, collection and detection of single photons emitted by the color center. Efficient emission and collection can be achieved by integrating color centers into nanophotonic structures, which enhance the light-matter interaction. Nanophotonic cavities improve the emission rate of the single photons into desired optical modes, and waveguides can guide these emitted photons with minimal losses. A higher number of available photons improves the fidelity of single-shot readouts of spin states, the reliability and efficiency of quantum gate operations and entanglement generation, and the bandwidth of the quantum communication channel. Detection involves coupling the photons in the waveguide to a fiber or into an objective for off-chip measurements. However, there are coupling and fiber losses involved in these processes, which can be eliminated by having on-chip superconducting nanowire single photon detectors (SNSPDs).

Solid-state systems offer scalability, but no major breakthroughs have been made in terms of a wafer-scale nanofabrication process in SiC. Nanophotonic integration of color centers in SiC has been demonstrated [38–42] through processes that required special processing (photoelectrochemical etch, wafer bonding and polishing, Smart-cut method), making them difficult to scale. Bulk nanofabrication processing technique, Faraday cage-assisted angle etching was used to integrate color centers into suspended, triangular cross-section devices in both diamond [43] and SiC [29, 44, 45]. However, this method is limited to small chip areas. The angle etching process can be brought to scale using ion beam etching (IBE) method, demonstrated in diamond [46] and requires development in SiC.

1.2 Contribution

The results presented in this dissertation advance our understanding of the electromagnetic behavior of novel triangular cross-section photonics, fill critical gaps in the existing nanofabrication processing techniques to produce suspended photonic devices in bulk SiC on a wafer scale, and demonstrates nanophotonic integration of NV centers in 4H-SiC for the first time.

From a modeling perspective, I investigated less-explored triangular cross-section photonic devices, designing single-mode waveguides with ∼90% coupling to the fundamental transverse electric mode of the waveguide, photonic crystal mirrors to enhance color center collection efficiencies, robust and tunable photonic crystal cavities with ultra-high quality factors and small mode volumes, and waveguides with integrated SNSPD detectors. These designs improve the overall emission, collection, and detection efficiencies of photons, essential for implementing large-scale QIP technologies. In an international collaboration between Prof. Marina Radulaski and Prof. Florian Kaiser (University of Stuttgart, Germany), I undertook the modeling of triangular cross-section waveguides suitable for integration of silicon vacancy centers. Additionally, I modeled the fabricated waveguides to elucidate experimental observations from silicon color centers in Faraday cage angle-etched triangular waveguides.

From a nanofabrication perspective, I developed and tested ion beam etch recipes for etching triangular cross-section devices in 4H-SiC, utilizing the Intlvac Nanoquest II tool at the Center for Nano-MicroManufacturing (CNM2), UC Davis. I devised the entire process flow, demonstrating the first wafer-scale bulk processing in 4H-SiC to fabricate suspended photonic devices, a significant milestone for the scalability of color center nanophotonics in 4H-SiC. In another international collaboration between Prof. Marina Radulaski and Prof. Kai Mueller (Technical University of Munich, Germany), I led the modeling and development of the process flow for integration of NbTiN SNSPDs onto triangular cross-section SiC waveguides. Our collaborators successfully deposited NbTiN films on 4H-SiC for the first time and measured the optical and transport properties, confirming its suitability for developing integrated SNSPDs on 4H-SiC. This is a crucial advancement addressing the challenges in efficiently detecting color center single photons, offering a path forward for scalability and production of chip-scale quantum photonic circuits. Furthermore, I was the leading researcher (again, Marina was the PI on those proposals) on multiple Molecular Foundry User Proposals (Lawrence Berkeley National Laboratory), where I created the entire process flow for generating and integrating NV centers in 4H-SiC into nanopillars for the first time and developed the first wafer scale photonic device fabrication process that maintains active color centers in SiC. I conducted photoluminescence measurements on the nanophotonic-integrated NV centers, showing enhanced collection efficiencies compared to NV centers in bulk 4H-SiC.

1.3 Outline

Chapter 1 of this thesis introduces the field and the motivation for this work. Chapter 2 introduces the fundamentals of color centers and photonics. Chapter 3 outlines the modeling and experimental (nanofabrication and optical characterization) methods used in this work. Chapters 4-7 detail the modeling results of various triangular cross-section photonic devices in 4H-SiC (waveguides, photonic crystal mirrors, photonic crystal cavities, beam splitters, waveguides with integrated SNSPDs), suitable for color center integration. Chapter 8 discusses the modeling of nanopillars, fabrication of nanopillars with integrated NV centers in 4H-SiC and their optical characterization. Chapter 9 presents the first wafer-scale nanofabrication results in 4H-SiC using ion beam etching. Chapter 10 provides an outlook.

Chapter 2

Color Centers and Nanophotonics

Solid-state defect-based emitters, color centers, have attracted great interest over other implementations of quantum information processing technologies like superconducting Josephson's junction and trapped ion technologies for their long coherence times, scalability, and room temperature operation. These color centers with the ability to generate single photons and optically addressable spin states emitters, find applications in quantum communication, computing, and sensing. In this chapter we first review the fundamentals of color centers, specifically in silicon carbide (SiC), followed by an overview of nanophotonics and their necessity for improving the color center single photon emission and collection.

2.1 Color Centers

Color centers are point defects (vacancy, impurity, interstitial, or atom-vacancy complexes) in wide bandgap semiconductors such as diamond and SiC. The defect localizes the electronic orbitals, resembling quasi-atoms, to produce energy levels (ground, excited, and intermediate shelving state) within the bandgap of the host material, as shown in Figure 2.1a. The electrons in the ground level can be optically addressed using lasers. The excited electrons, upon spontaneous emission through both radiative and non-radiative pathways, would result in an emission spectrum with two features: the zero-phonon line (ZPL) and the phonon sideband (PSB), as shown in Figure 2.1b. ZPL is a narrow

Lorentzian peak corresponding to the zero-phonon transition, producing indistinguishable photons necessary for QIP applications. PSB is a broad peak originating from all the transitions from the excited state to the other vibronic levels of the ground state. The proportion of radiative emission occurring through the zero-phonon transition compared to the transitions to all vibronic levels is given by the Debye-Waller (DW) factor ξ.

For instance, the nitrogen vacancy (NV) in 4H-SiC consists of a substitutional nitrogen atom in the carbon site adjacent to a silicon vacancy, denoted as $\mathrm{N_C V_{Si}}$. A negatively charged NV center ($\mathrm{NV^-}$) has the same electronic structure as $\mathrm{NV^-}$ center in diamond with a spin S = 1, spin-triplet ground and excited states ($m_\mathrm{s} = 0, \pm 1$), and an intermediate singlet state ($m_\mathrm{s} = 0$) within the SiC bandgap, as shown in Figure 2.1a. Upon optical illumination (blue), the electrons are excited from the spin-triplet ground state to the spin-triplet excited state and radiatively decay back (red), conserving the spin during these transitions. However, the lower brightness associated with the decay of the $m_\mathrm{s} = \pm 1$ state compared to that of $m_\mathrm{s} = 0$ is attributed to the non-radiative, spin-flipping decay path through the intermediate shelving state (grey), as shown in Figure 2.1a.

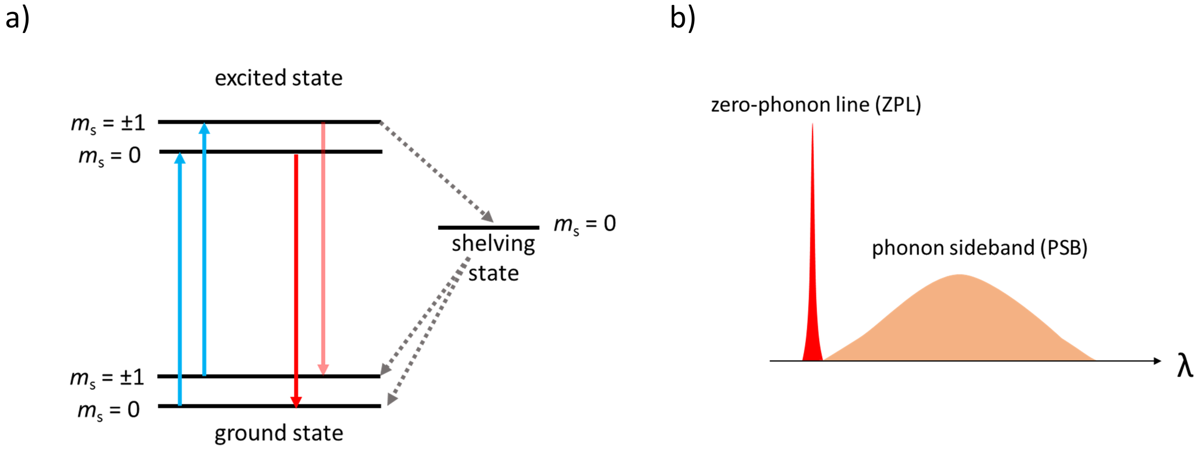

Figure 2.1: a) Simplified energy level diagram of the spin = 1 nitrogen vacancy center in 4H-SiC in zero magnetic fields. b) Emission spectrum of a color center showing the zero-phonon line and the phonon sideband.

Color centers hold great promise for implementing QIP hardware due to their capability of creating entanglement between the electron spin and a photon, which serves as a stationary and a flying qubit respectively. Photons, being immune to thermal noise and capable of traveling extended distances through fiber-optic cable without mutual interaction, are highly suitable as carriers of quantum information. Spin-entangled photons from two distant systems can be relayed to an intermediate location to perform entanglement swapping, thereby establishing remote entanglement between the systems without requiring direct interaction. The milli-seconds coherence times of the color centers can be improved by using isotopically purified material, which minimizes the impact of the nuclear spins associated with the naturally existing isotopes (such as ^{13}C in diamond, and ^{13}C, ^{29}Si, ^{30}Si in SiC) on the electron spins [25, 27, 32, 47]. Further extension of coherence times can be achieved by swapping the electron spin onto a longer-lived nuclear spin (memory qubit) [48].

After the demonstration that a negatively charged nitrogen vacancy (NV^{-}) center in diamond can be individually initialized, manipulated, and measured with high fidelity at room temperature [49], color centers emerged as a potential candidate for solid-state quantum emitters. However, due to the unavailability of single-crystal diamond wafers and color centers with emission wavelengths in the telecommunication bands, alternative materials have been investigated as potential hosts for defects. In this regard, silicon carbide has garnered attention for its color centers with long spin coherence times, excellent brightness, and availability of nuclear spins. Additionally, SiC offers benefits such as a large bandgap, strong second-order non-linearity, excellent thermal conductivity, and a decades-long industry presence. Importantly, SiC hosts color centers with emissions in the telecommunications wavelength range, and these photons can be distributed using the existing fiber optics infrastructure for QIP applications.

Silicon carbide is available in 250 polytypes, with the most common being 3C, 4H, and 6H, and the majority of color centers studied in 4H-SiC. Figure 2.2 shows some of the prominent color centers studied in 4H-SiC, including the silicon vacancy [40, 50–52], divacancy [39, 53], nitrogen vacancy [19, 21, 22], and transition metal defects like chromium [54–56], molybdenum [57–59], vanadium [23, 24], with emission wavelengths in the near-infrared region. Color centers may occur naturally in an as-grown material or be induced through in-situ doping during crystal growth or via implantation into the material. For the purposes of QIP, color centers with emission wavelengths in the telecommunication bands are most suitable, as their photons can be sent over long distances using the existing fiber network while experiencing lower losses. Hence, in this work, we are interested in the nitrogen vacancy and vanadium defect in 4H-SiC, which have emissions close to the O-band of the telecommunication wavelength (1260-1360 nm).

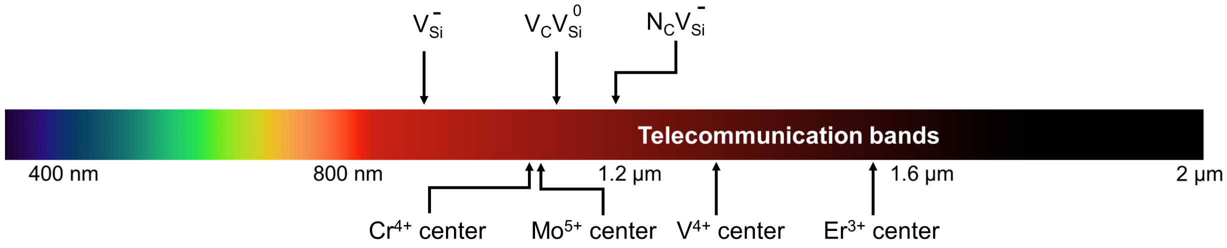

Figure 2.2: Color centers in 4H-SiC and their emission wavelengths on the electromagnetic spectrum.

Each atomic bilayer of SiC consists of hexagonally arranged carbon atoms tetrahedrally bonded to three silicon atoms in the bilayer and one silicon atom in the bilayer stacked above it. The plane formed by the bilayer is called the a-plane (with the a-axis in this plane), and the plane perpendicular to the a-plane is called the c-plane (with the c-axis in this plane). A bilayer stacked on top of another bilayer can have three possible orientations: "A", "B", and "C", while maintaining the tetrahedral bonding. In 4H-SiC, the stacking sequence of the bilayers is ABCB, as shown in Figure 2.3. Each atom in this lattice structure is labeled as 'h'(hexagonal) or 'k'(cubic), depending on the quasi-hexagonal and quasi-cubic environments they are present in. In the polytype notation 4H, the number "4" corresponds to the number of atomic bilayers required for the lattice to repeat itself, and the letter "H" corresponds to the hexagonal lattice type.

The nitrogen vacancy (NV) center in 4H-SiC, being a two-site defect with two inequivalent sites (h, k) in 4H-SiC, can exist in four possible configurations: *hh, kk, hk,* and *kh*, as shown in Figure 2.3. NV centers in the *hh* and *kk* configurations have their dipoles oriented along the c-axis, whereas those in *hk* and *kh* configurations have their dipoles oriented at an angle of 71° to the c-axis. The emission spectrum of the NV center in 4H-SiC exhibits four ZPLs corresponding to the four configurations of the NV center.

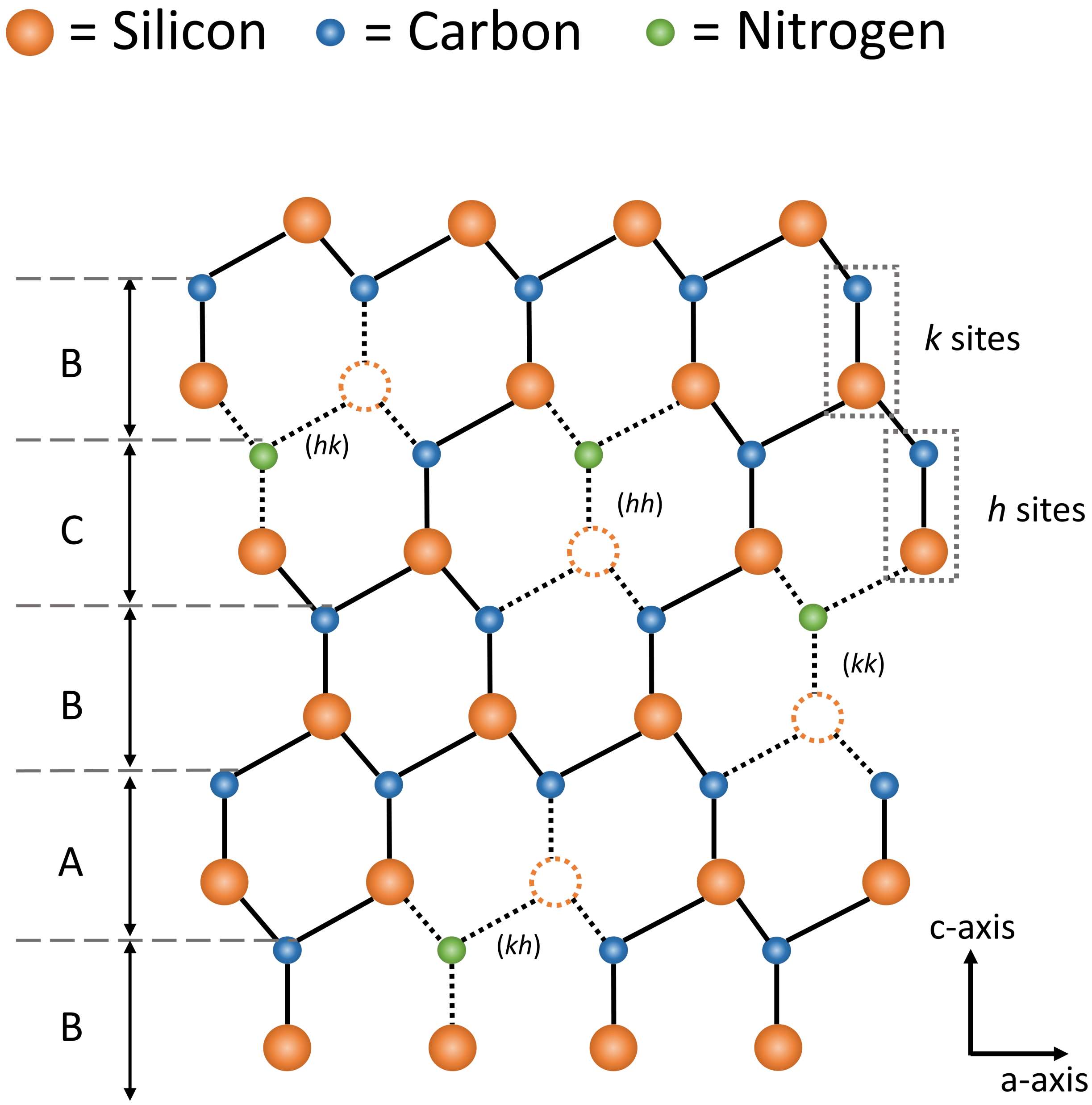

Figure 2.3: Two-dimensional view of the 4H-SiC lattice showing the stacking of the atomic bilayers in the ABCB sequence and the inequivalent "h" and "k" lattice sites. The figure also shows the four possible configurations of the nitrogen vacancy center in 4H-SiC, *hh, kk, hk, kh.*

The emission wavelengths are in the range of 1176 - 1242 nm [34], closer to the O-band of the telecommunication wavelengths. These photons can thus be transmitted over the existing fiber optic cable network without experiencing much loss, making the NV center in 4H-SiC a suitable candidate among the variety of color centers investigated for applications in QIP.

2.2 Nanophotonics

Color centers are single photon emitters and are suitable for applications in quantum light generation, spin-photon entanglement, and entanglement distribution. To build a large quantum network with photon-based entanglement distribution, an important criterion is the availability of network nodes with efficient spin–photon interfaces. However, the properties of color centers are sensitive to their environment including neighboring crystal defects, nuclear spins, surface-related charges, and coupling to phonons. This sensitivity presents a challenge to achieving the theoretically calculated spin-optical properties in their naturally existing forms. Integration of color centers into nanophotonic structures offers a solution, enhancing light-matter interaction to improve spin–photon interfaces, and spin-optical characteristics such as the generation of more indistinguishable photons, efficient optical initialization of spin, longer coherence times, on-chip integration, and scalability. Depending on the intensity of light-matter interaction, photonic devices can be classified as passive or active devices. Passive devices facilitate the coupling of light into an optical mode to enhance collection efficiencies and promote low-loss guiding of the photons. Active devices, on the other hand, enhance the spontaneous emission rates of color centers. Figure 2.4 shows scanning electron microscope (SEM) images of passive and active devices is SiC with integrated color centers.

2.2.1 Passive Photonic devices

Color center emission in a high refractive index bulk is directed based on its dipole orientation, and when a fraction of this emission reaches the bulk-air interface, it undergoes total internal reflection, resulting in low collection efficiencies of the emitted photons. Passive photonic devices direct the photons emitted by the color center and improve the light coupling efficiency into the optical mode of the device. Passive photonic devices in 4H-SiC like solid immersion lens [62, 63] and nanopillars [40, 60, 64] were used to demonstrate enhanced light collection efficiencies. Waveguides can be used for coupling

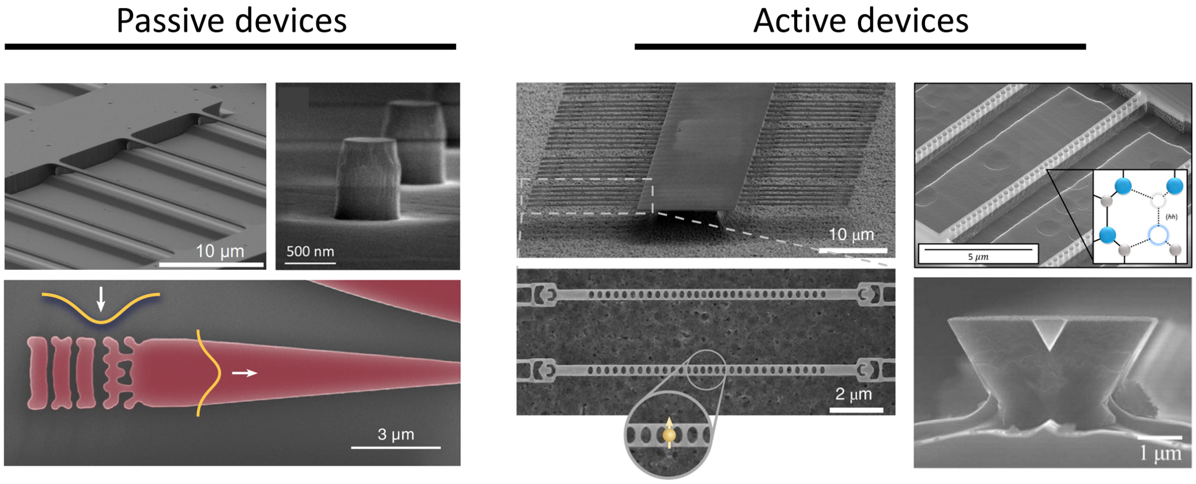

Figure 2.4: The SEM images of silicon carbide photonic devices realized in literature. **Passive devices** (clockwise from top left): Triangular cross-section waveguide in 4H-SiC with integrated silicon vacancies [29], nanopillars in 4H-SiC with silicon vacancies [60], vertical coupler fabricated in 4H-SiCOI to convert free-space Gaussian beam into fundamental waveguide mode [61]; **Active Devices:** Suspended nanobeam array fabricated in 4H-SiCOI and (below) magnified image of individual nanobeam PCC with integrated silicon vacancies [40], nanobeam PCC in 4H-SiC with integrated neutral divacancies [39], triangular cross-section nanobeam PCC fabricated in 4H-SiC [44].

dipole-like color center emission into well-defined optical modes to be routed on-chip in a nearly lossless way. The light coupled into this optical mode can be coupled into fiber for off-chip processing using free space grating couplers and tapered fiber couplers. Deterministic positioning of the color center in the passive devices can further enhance the collection efficiencies, resulting in higher bandwidths of the quantum channel.

2.2.2 Active Photonic Devices

Active devices like photonic crystal cavities (PCC) create light-matter interaction by confining light to sub-wavelength volumes, resulting in an increased density of states at the resonant wavelength of the cavity. When the ZPL wavelength of the color center is resonant with the cavity, the spontaneous emission rate of the color center is enhanced through the Purcell effect. The enhancement in radiative emission is given by the Purcell factor(F_P):

$$F_P = \left[\frac{3}{4\pi^2}\left(\frac{\lambda}{n}\right)^3\left(\frac{Q}{V}\right)\right]\left[\left|\frac{E}{E_{\max}}\right|\cos(\phi)\right]\xi$$

F_P can be maximized by integrating a color center into a cavity with a high-quality factor (Q) and low cavity mode volume (V). F_P can be further boosted by optimally positioning the emitter inside the cavity, which corresponds to the spatial overlap ($|E/E_{\max}|\cos(\phi)$) term in the equation. It should be noted from the equation above that the Q/V value required to achieve the same F_P value for different color centers depends on the DWF of the color center (ξ).

The Purcell factor considers only the radiative emission resonant with the cavity, which might not be the only path for the emitter to decay from the excited state. Other pathways, like non-radiative decay, emission into the phonon sideband, and pure dephasing, might exist. Cooperativity (C) is the ratio of radiative emission rate through the cavity to the total decay rate of the emitter in the absence of the cavity [65, 66]. Although the spontaneous emission is enhanced through the Purcell effect ($F_P > 1$), the emission through the cavity can still be smaller compared to the overall emission - weak coupling regime (C $<$ 1). To achieve deterministic atom-photon interactions, the coupling between the cavity and emitter should be stronger than all the other dephasing mechanisms - strong coupling regime ($C > 1$) [66, 67]. Furthermore, emitter ensembles in a cavity with collective coupling rates to the cavity resonant mode comparable to the inhomogeneous broadening exhibit longer storage times, apt for quantum memory applications [68].

2.2.3 Triangular Cross-Section Photonics

Nanophotonic integration of color centers offers scalability by leveraging the combination of a solid-state platform and the nearly identical optical properties of ensembles, a feature previously inaccessible in studied systems. Additionally, there are further benefits such as reduction in lifetime, spectral diffusion, and homogeneous broadening, along with an increased number of indistinguishable photons, necessary to achieve high-fidelity measurements for applications in QIP.

A key requirement for nanophotonic integration is the ability to grow or place high-quality, high-refractive-index thin films on a contrasting substrate, enabling high optical confinement in nanostructures. For instance, the ability to bond silicon on insulator in a scalable manner has positioned silicon as a strong material platform for photonics applications [69]. Although commercial-scale production of high-quality crystalline SiC wafers using homoepitaxy (MBE, CVD) or sublimation has been employed in color center research, such as *in situ* doping of vanadium centers in 4H-SiC [70], this approach does not provide an undercutting layer needed to generate freestanding photonic devices. Conversely, the growth of 3C-SiC on silicon has been established in MEMS research [71], but has not lent itself well for color center formation in nanoscale films due to the lattice mismatch damage [41]. These substrate limitations have been addressed through photo-electrochemical etching [72] and SiC thinning and bonding to an insulator [40]. While these approaches successfully integrated and manipulated color centers in a nanocavity, the fabrication processes have been restricted either in terms of substrate type or size, necessitating a specific doping profile or limiting the chip area.

Another bulk substrate nanofabrication approach, initially championed in diamond [43], has been emerging in silicon carbide: the angle-etching method [44, 52]. In contrast to the more traditional (rectangular) profile, the photonic devices created via angle-etch have a triangular cross-section. Such SiC processing methods are currently based on the Faraday-cage assisted etching; still, wafer scale processes could be implemented using ion beam etching [46].

Angle-etched devices with integrated color centers have been demonstrated in diamond using both Faraday cage method and ion beam etching method. These color center-integrated photonic systems have been used to make several remarkable demonstrations necessary to implement QIP technologies, such as, nanocavities with cooperativities exceeding 100 [17], >99% single-shot readout and spin initialization fidelities [17], cavity-coupled two-qubit registers with seconds-long coherence times [73–75], generation of single photons with highly tunable temporal wave packets and high spectral purity useful for generation of cluster states [76], > 90% outcoupling efficiencies from emitter-cavity system into fiber [17, 77], memory enhanced quantum communication [17], strain control for emitter tuning [78, 79], and quantum frequency conversion to telecom band with high distinguishability [80].

Triangular device geometry resolves the problem of the unavailability of heteroepitaxial thin film color center substrates because it can be implemented in bulk substrates of any polytype or doping level. However, due to the novelty of the approach, not much is known about the optical properties and parameters related to the color center integration into angle-etched SiC devices. In this dissertation, we focus on modeling of triangular cross-section photonics (waveguides, photonic crystal mirrors, beamsplitters, photonic crystal cavities) and developing a wafer-scale ion beam etch process to fabricate triangular cross-section photonics, suitable for nanophotonic integration of NV center in 4H-SiC.

Chapter 3

Numerical and Experimental Methods

Traditional photonic devices typically have either rectangular or circular cross-sections, and little is known about the electromagnetic properties of triangular cross-section photonics. Triangular cross-section devices fabricated in 4H-SiC [44, 52] employed Faraday-cage assisted angle etching, where reactive ions are directed at an angle by the Faraday cage to etch underneath the device, resulting in suspended photonic devices. However, this approach is not scalable, as it is limited to small chip areas and would require machining a separate Faraday cage for each of the triangular cross-sections needed to be fabricated. Nevertheless, angle etching can be brought to scale using ion beam etching (IBE), which was used to demonstrate triangular cross-section devices in diamond [46].

Triangular photonics with integrated color centers in diamond paved the way for important demonstrations, including spin-photon entanglement [17, 78, 80], high-fidelity operations [17], and multi-qubit quantum registers [73–75]. However, the development of an ion beam etch process to angle etch SiC and the understanding of the electromagnetic fundamentals of triangular photonics in SiC are lacking. In this dissertation, our focus is on understanding the electromagnetic behavior of triangular cross-section photonics through modeling and the fabrication of color center integrated nanophotonics in 4H-SiC. This chapter discusses the fundamentals of the numerical methods used for modeling, nanofabrication process and equipment, and the cryogenic optical characterization setup.

3.1 Numerical Approach

Triangular cross-section photonics are less explored. In this dissertation, we utilize finite-difference time-domain (FDTD) simulations to predict the behavior of electromagnetic fields in photonic structures and their evolution over time, employing the FDTD and MODE software packages of Ansys Lumerical. Various triangular cross-section photonic devices in SiC, such as waveguides, photonic crystal mirrors, photonic crystal cavities, photonic molecules, waveguides with integrated superconducting nanowire single photon detectors, beamsplitters, were simulated. The device geometries were optimized for integration of color centers, specifically nitrogen vacancy center and silicon vacancy in SiC. The results of the simulations will be discussed in the upcoming chapters.

3.1.1 Finite-Difference Time-Domain Simulations

The Finite-Difference Time-Domain (FDTD) method was introduced by Kane S. Yee to solve time-dependent Maxwell's equations within a finite spatial domain [81]. This method approximates the time and spatial derivatives in Maxwell's equations to finite differences. The continuous electric and magnetic fields are represented as discrete values on the spatial grid and are advanced in time. By sampling the spatial field into a suitable grid, the discrete values of electric and magnetic fields used in Maxwell's equations can provide reliable numerical solutions for a broad range of frequencies in a single run.

Finite Difference Approximation

The Taylor's expansion of a function *f(x)* expanded about the point x_0 with an offset of ±Δ *x/2* is given by [81]:

$$f(x_0 + \frac{\Delta x}{2}) = f(x_0) + \frac{\Delta x}{2} f'(x_0) + \frac{1}{2!}\left(\frac{\Delta x}{2}\right)^2 f''(x_0) + \frac{1}{3!}\left(\frac{\Delta x}{2}\right)^3 f'''(x_0) + ... \tag{3.1}$$

$$f(x_0 - \frac{\Delta x}{2}) = f(x_0) - \frac{\Delta x}{2} f'(x_0) + \frac{1}{2!}\left(\frac{\Delta x}{2}\right)^2 f''(x_0) - \frac{1}{3!}\left(\frac{\Delta x}{2}\right)^3 f'''(x_0) + ... \tag{3.2}$$

Calculating the difference between the first and second equation gives:

$$f(x_0 + \frac{\Delta x}{2}) - f(x_0 - \frac{\Delta x}{2}) = \Delta x f'(x_0) + \frac{2}{3!}\left(\frac{\Delta x}{2}\right)^3 f'''(x_0) + ... \tag{3.3}$$

Dividing both sides by Δx gives:

$$\frac{f(x_0 + \frac{\Delta x}{2}) - f(x_0 - \frac{\Delta x}{2})}{\Delta x} = f'(x_0) + \frac{1}{3!}\left(\frac{\Delta x}{2}\right)^2 f'''(x_0) + ... \tag{3.4}$$

The left-hand side of the equation is a sum of the derivative of the function *f(x)* at $x = x_0$ and an infinite number of terms with $(\Delta x)^2$ as the lowest order of Δx, denoted by $O((\Delta x)^2)$.

$$\left.\frac{df}{dx}\right|_{x=x_0} = \frac{f(x_0 + \frac{\Delta x}{2}) - f(x_0 - \frac{\Delta x}{2})}{\Delta x} + O((\Delta x)^2) \tag{3.5}$$

If Δx is sufficiently small, the $O((\Delta x)^2)$ can be ignored to arrive at the finite difference equation given by:

$$\left.\frac{df}{dx}\right|_{x=x_0} \approx \frac{f(x_0 + \frac{\Delta x}{2}) - f(x_0 - \frac{\Delta x}{2})}{\Delta x} \tag{3.6}$$

Yee's algorithm

The arrangement of electric (E) and magnetic (H) fields with respect to the center of the cell within a spatial grid of the FDTD method is shown in Figure 3.1. The staggered orientation of E- and H-fields in the spatial grid is based on the integral form of Maxwell's curl equation (Faraday's and Ampere's law), where each E-field component is encompassed by circulating H-field components and vice versa.

To begin the construction of a FDTD algorithm for a non-dispersive and isotropic system, consider the Faraday's and Ampere's law:

$$\frac{\partial}{\partial t}\boldsymbol{H}(\boldsymbol{r}, t) = -\frac{1}{\mu(\boldsymbol{r})}\nabla \times \boldsymbol{E}(\boldsymbol{r}, t) \tag{3.7}$$

$$\frac{\partial}{\partial t}\boldsymbol{E}(\boldsymbol{r}, t) = \frac{1}{\epsilon(\boldsymbol{r})}(\nabla \times \boldsymbol{H}(\boldsymbol{r}, t) - \sigma(\boldsymbol{r})\boldsymbol{E}(\boldsymbol{r}, t)) \tag{3.8}$$

which can be written as a set of six scalar equations, one for each component of E- and

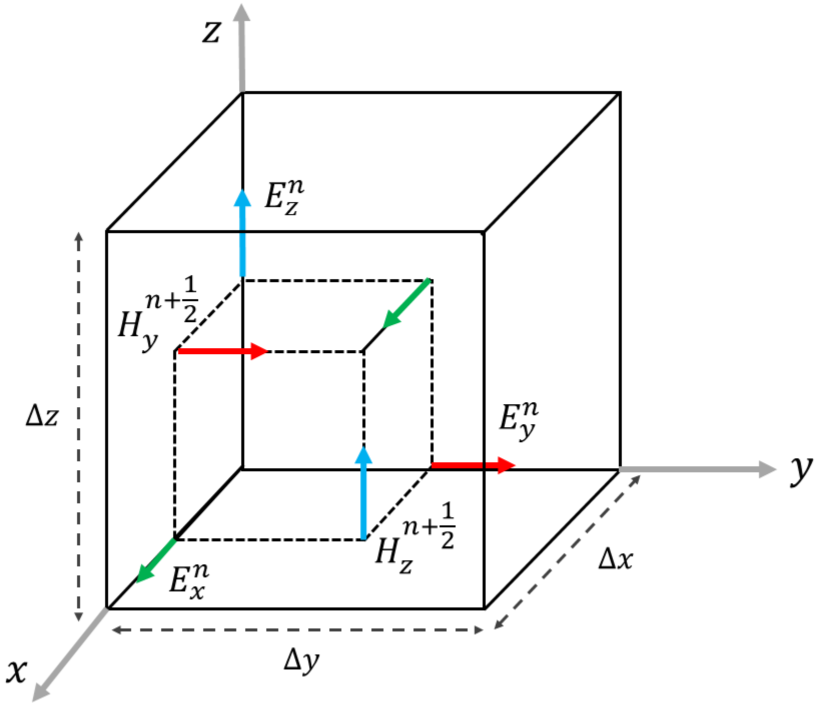

Figure 3.1: The placement of staggered electric and magnetic fields within a Yee's unit cell with mesh dimensions Δx, Δy, Δz in x, y, z directions respectively.

H-field. In Yee's work [81], a grid point in a uniform orthogonal mesh is defined as

$$(i, j, k) = (i\Delta x, j\Delta y, k\Delta z) \tag{3.9}$$

and any function of space and time is denoted as

$$F^n(i, j, k) = F(i\Delta x, j\Delta y, k\Delta z, n\Delta t) \tag{3.10}$$

where Δx, Δy, Δz are the spatial increments of the mesh in x, y, z directions respectively and Δt is the time step increment and i, j, k, n are integers. Using the finite difference approximation for partial derivatives in equation 3.6, the x-components of E - and H -

fields for a perfectly conducting boundary condition are:

$$
\begin{aligned}
H_x^{n+1/2}(i+1/2,j,k) = H_x^{n-1/2}(i+1/2,j,k) - &\frac{\Delta t}{\mu(i+1/2,j,k)} \\
&\left[\frac{E_z^n(i+1/2,j+1/2,k) - E_z^n(i+1/2,j-1/2,k)}{\Delta y}\right. \\
&\left. - \frac{E_y^n(i+1/2,j,k+1/2) - E_z^n(i+1/2,j,k-1/2)}{\Delta z}\right]
\end{aligned}
\tag{3.11}
$$

$$
\begin{aligned}
E_x^{n+1}(i,j+1/2,k+1/2) = E_x^n(i,j+1/2,k+1/2) - &\frac{\Delta t}{\epsilon(i,j+1/2,k+1/2)} \\
&\left[\frac{H_z^{n+1/2}(i,j+1,k+1/2) - H_z^{n+1/2}(i,j,k+1/2)}{\Delta y}\right. \\
&\left. - \frac{H_y^n(i,j+1/2,k+1) - H_y^n(i,j+1/2,k)}{\Delta z}\right]
\end{aligned}
\tag{3.12}
$$

Similar equations can be formulated for E_y, E_z, H_y, H_z. At the beginning of the simulation, all the E- and H-field values at each grid point are initialized to zero. Each of the six equations is enforced independently for every cell in the grid. It is important to note that the H-fields are computed at (integer + 1/2) values of the temporal step, while E-fields are computed at integer values of the temporal step. In equation 3.11, the future value of H-field ($H_x^{n+1/2}$) is determined using the previous values of H-field at that point ($H_x^{n-1/2}$) and the previous values of E-fields at adjacent points (E_x^n). This updated value of $H_x^{n+1/2}$ is used to calculate the future value of E-field (E_x^{n+1}) in equation 3.12. This process is repeated iteratively to track the time evolution of the electromagnetic fields across the simulation region.

One primary advantage of this method over frequency domain approaches is its ability to easily model non-linear dielectric and magnetic materials by assigning arbitrary permittivity and permeability values to each lattice point [82]. However, this method introduces non-physical numerical dispersion due to the disparity in velocities of the numerical wave and the actual speed of light, which varies depending on the wavelength, wave's propagation direction, and mesh dimensions. The numerical dispersion error decreases with the cell size of the Yee grid and must be much smaller than the shortest wavelength available in the model or the minimum scatterer dimension [82].

The numerical stability of the Yee's algorithm depends on the mesh dimensions (Δx, Δy, Δz) and the temporal step size (Δt) and is expressed by [82]:

$$\Delta t < v_{max}^{-1}\left(\frac{1}{(\Delta x)^2}+\frac{1}{(\Delta y)^2}+\frac{1}{(\Delta z)^2}\right)^{-1/2} \tag{3.13}$$

where v_{max} is the maximum velocity of light in the FDTD lattice.

3.2 Nanofabrication

To build scalable QIP technologies, photonic devices need to be fabricated in a repeatable manner on chip-scale. SiC is commercially available as wafers, owing to its decades-long presence in the semiconductor industry. In this dissertation, we use a 4-inch diameter, 500 μm thick wafer of on-axis (c-axis normal to the wafer surface), high-purity-semi-insulating (HPSI) 4H-SiC from Norstel AB (now ST Microelectronics). We initiate the processing by dicing the wafer into 5 mm × 5 mm chips, using the Disco DAD 321 Dicing Saw. Subsequent nanofabrication steps are performed on these individual chips. Before the nanofabrication processing begins, color centers are generated through ion implantation and activated by annealing.

3.2.1 Ion Implantation

Most of the studied color centers are generated through implantation where projectiles (electrons, protons, neutrons, ions) with sufficient energy penetrate through the material surface. The implantation process is typically followed by annealing in a vacuum or inert atmosphere to activate the implants and repair some of the crystal lattice damage caused during implantation, although not completely [83]. The residual damage can create pathways for decoherence of the electron spin, which is a disadvantage while building QIP hardware. This challenge can be partly overcome by using lighter projectiles like electrons, protons (instead of heavier ions) on *in situ* doped substrates. Further, more controlled defect generation methods, such as focused ion beam [84], laser writing [85–

87], proton beam writing [88], and ion implantation on patterned substrates [89], can also enable optimal emitter distribution.

In this work, nitrogen vacancy centers were generated in 4H-SiC through commercial implantation (CuttingEdge Ions, LLC) of the 4H-SiC chips with $^{14}N^{+}$ ions. The implantation doses were selected as $2.5 \times 10^{11} cm^{-2}$ and $1 \times 10^{14} cm^{-2}$ for the generation of single color centers [37] and ensembles [33], respectively. The implantation energy was determined based on the optimal depth of the color center required for the fabricated photonic device. For nanopillars, the aim was to position the color centers at a depth of 500 nm below the surface, corresponding to the longitudinal midpoint of the 1 μm nanopillars. For the triangular cross-section devices, the target depth for color center implantation was $\sim$ 100 nm for optimal positioning in these devices. The implantation energies were calculated using stopping and range of ions in matter (SRIM) simulations [90], resulting in energies of 375 keV and 65 keV, with a peak nitrogen concentration at depths of 500 nm and 100 nm, respectively, as shown in Figure 3.2. Subsequently, the implants were activated through annealing of the samples in a 1-inch Lindberg Blue tube furnace at 1050 °C in a nitrogen atmosphere for 60 minutes [33].

3.3 Nanofabrication Process Flow

After the ion implantation and annealing, the samples were cleaned in a 4:1 piranha solution at 80 °C. Subsequently, a 7 nm titanium layer was deposited using a CHA electron beam evaporator. This thin metal layer improves the quality of the electron beam lithography (EBL) by acting as a conductive layer for the charge accumulated on the semi-insulating SiC substrate during EBL. Importantly, this thin layer does not interfere with the etch time, as it is removed within seconds during all the SF_6-based etch processes conducted. Following this, the samples were then spin-coated with e-beam resist (PMMA C4) at 2000 rpm and baked in an oven at 180 °C for 5 minutes. Next, an anti-static agent, aquaSAVE, was spin-coated onto the samples at 2000 rpm and then baked on a hotplate at 100 °C for 1 minute. The patterns were then transferred

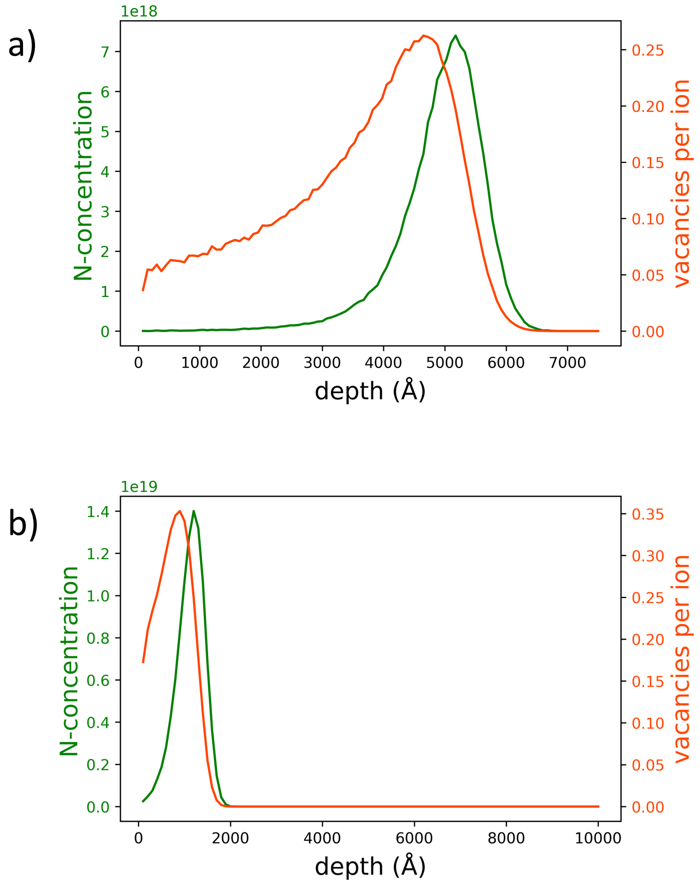

Figure 3.2: SRIM simulations for $^{14}N^{+}$ ion distribution in 4H-SiC for ion energies a) 375 keV, b) 65 keV.

onto the 350 nm PMMA layer using EBL in the Vistec VB300 EBL system followed by development in 3:1 IPA:MIBK solution for 1 min.

The developed samples were then coated with a 5 nm titanium adhesion layer followed by a nickel hard mask layer, using a CHA electron beam evaporator. Next, the pattern was transferred to this metal layer using lift-off method, involving rinsing and sonicating the samples in dicholormethane and acetone, respectively. This was followed by etching the samples using either the Oxford PlasmaLab 150 inductively coupled plasma reactive ion etching (ICP-RIE) tool or the Intlvac Nanoquest II ion beam etching tool, depending on the type of photonic device being fabricated. The thickness of the nickel hard mask was chosen based on the selectivity of the etch in the respective etching tool. After the etching was completed, the nickel and titanium layers were etched away using Transene's nickel etchant TFB and titanium etchant TFTN, at 40 °C for 30 seconds. The entire process flow for fabrication of nanopillars and triangular cross-section devices is shown in Figure 3.3.

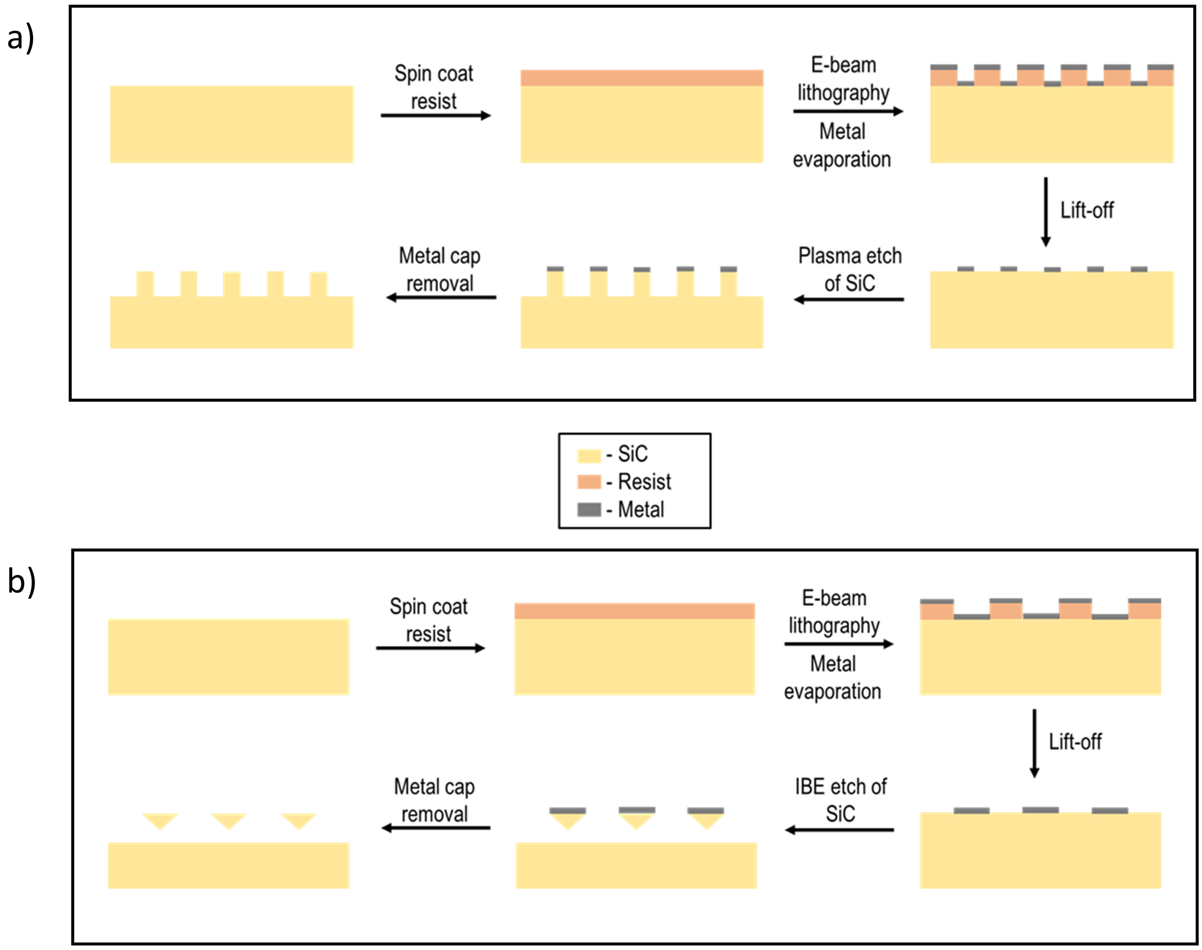

Figure 3.3: Process flow for fabrication of a) nanopillars, b) triangular cross-section photonic devices.

3.4 Inductively Coupled Plasma Reactive Ion Etching

SiC is a chemically inert material with a strong silicon-to-carbon bond energy of 4.6 eV, requiring dry etching methods involving SF_6 and O_2 gas chemistries for top-down processing [91, 92]. The etch process happens through the reaction:

$$\mathrm{SiC} + \mathrm{xF} + \mathrm{yO} \longrightarrow \mathrm{SiF_4} + (\mathrm{CO}, \mathrm{CO_2}, \mathrm{COF_2})$$

The addition of oxygen to the gas mixture enhances etch rates by introducing a pathway for volatalizing C in the forms of CO, CO_2 and COF_2, while also increasing the availability of flourine species for the etching process. However, excess oxygen in the chamber can lead to the formation of SiO_x, which redeposits and reduces the etch rates. In this work, we use an SF_6:O_2 ratio of 4:1 to achieve optimal results [91, 92].

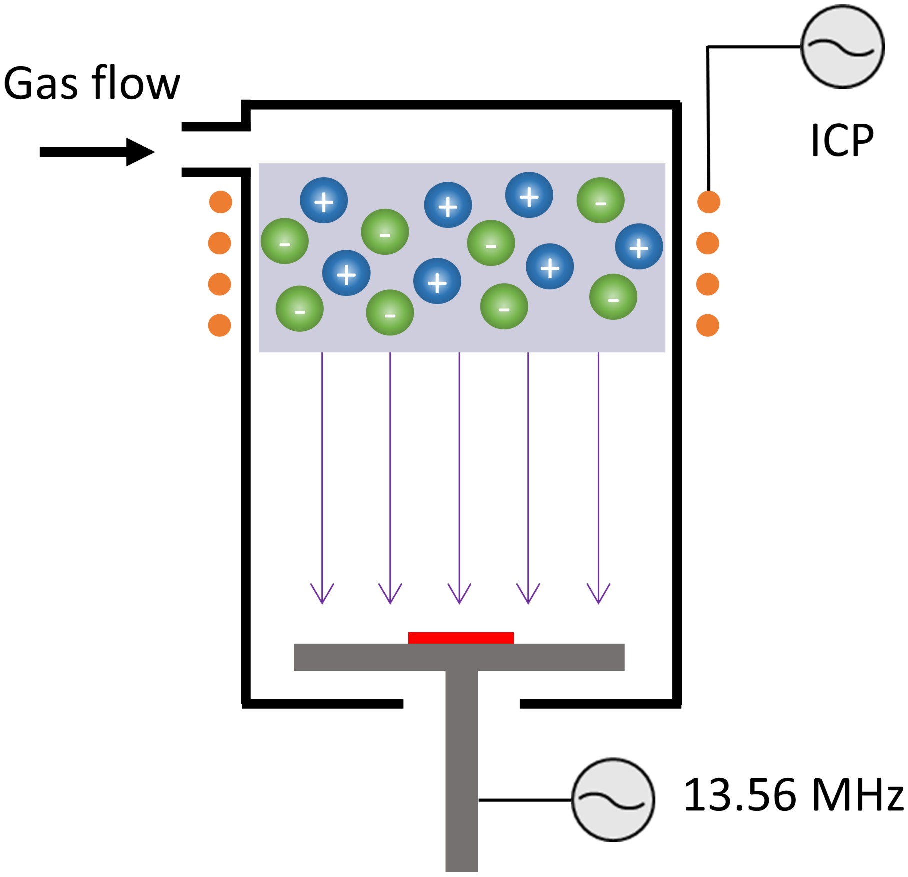

Figure 3.4: Illustration of an ICP-RIE process. Plasma is generated from the gases flowing through the inlet by the ICP source. The ions in the plasma are then accelerated towards the target substrate by the 13.56 MHz RF supply applied to the substrate holder to achieve etching of the target substrate.

An inductively coupled plasma reactive ion etching (ICP-RIE) process begins with the introduction of a gas mixture into a vacuum chamber containing the target substrate. A high-frequency electric current passing through coils positioned above the chamber generates an oscillating magnetic field, that ionizes the gas molecules and creating a plasma composed of ions, electrons and neutral species. The ions in the plasma are accelerated toward the substrate by applying an RF (13.56 MHz) bias to the substrate holder, as shown in Figure 3.4. Upon reaching the substrate, the ions etch the target substrate through a combination of physical sputtering and chemical etching.

Several parameters, such as ICP power, bias voltage, chamber pressure, and gas flow composition, can be independently controlled to achieve the desired etching profiles of the target substrate [91–94]. Higher ICP power results in an increased plasma density, thereby enhancing chemical etching in the chamber. A higher bias voltage accelerates the ions to higher energies, increasing both the physical etching in the chamber and the directionality of the etch. Increasing chamber pressure reduces the mean free path and lifetime of the ions, affecting the directionality of the etch and etch rates, respectively. In this work, the optimized ICP-RIE parameters in Oxford PlasmaLab 150 were as follows: ICP power = 1000 W, bias voltage = 300 V, chamber pressure = 5 mTorr, and SF_6 and O_2 flow rates = 40 and 10 standard cubic centimeters per minute (SF_6:O_2 ratio of 4:1), to achieve a SiC etch rate of $\sim$ 300 nm/min.

3.5 Ion Beam Etching

Ion beam etching (IBE) involves directing a focused beam of energetic ions generated from inert gases (such as Argon) or reactive gases (such as SF_6, O_2, CHF_3, Cl_2), causing physical milling or chemical etching to remove the target substrate. The etch begins when the gas mixture is introduced into a discharge chamber, where plasma is created by the ionizing these gases using the RF power source. The ions are then extracted from the discharge chamber and accelerated towards the target substrate using a combination of two grids, as shown in Figure 3.5a. A key difference between the IBE and ICP-RIE processes is that in IBE, the plasma is created in a separate environment (discharge chamber) from the one the target substrate is present in.

The initial grid, known as the screen grid, makes contact with the plasma and establishes a positive beam voltage of the ions. The subsequent grid, called the accelerator grid, which is set to a negative voltage, accelerates the ions towards the target substrate and reflects the electrons back into the plasma. Finally, an electron neutralizer injects a

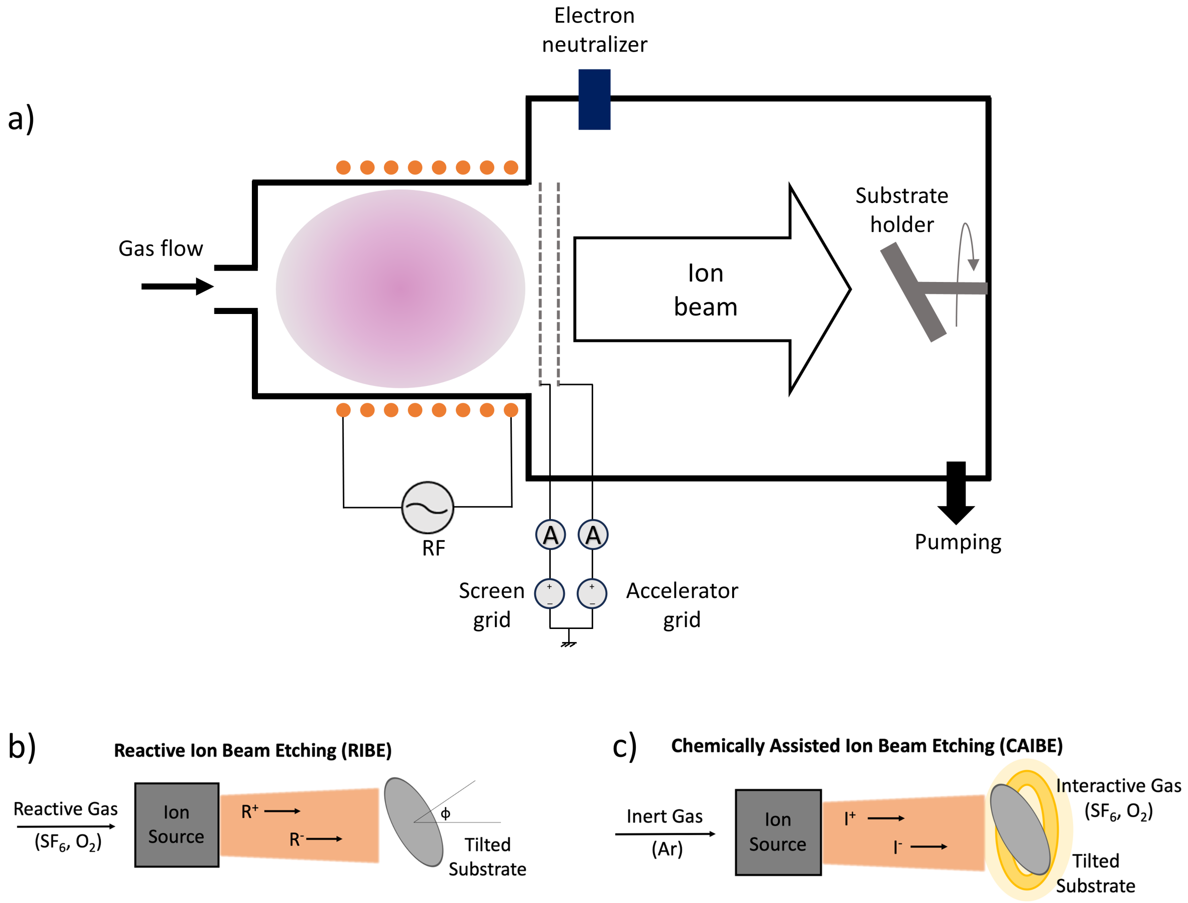

Figure 3.5: Illustration of a) Ion beam etching tool, b) Reactive ion beam etching, c) Chemically assisted reactive ion beam etching.

stream of electrons into the positive ion beam to balance space charge effects and assist in maintaining the collimation of the ion beam. The ion beam then strikes the target, placed on the substrate holder, which can be tilted to generate angled etching and rotated to ensure uniform etching.

Because of the proximity of the positive screen grid and the negative accelerator grid, the accelerator grid must maintain a voltage well below 0 V to ensure that the voltage at the center of the accelerator grid apertures to be negative ($V_{\min} < 0$). This configuration prevents the flow of electrons from the neutralized ions back into the discharge chamber. Typically, accelerator voltage values of about 10-20 percent of the beam voltage are needed to achieve this [95]. The potential variation inside the IBE chamber is shown in Figure 3.6. The control of ion energy and divergence within the beam is governed by the voltage applied to the grids. The beam current, which represents the ion flux exiting the source, depends on the ion density established by the plasma source. Consequently, ion energy, flux, and divergence can be finely tuned independently across a wide range of operational parameters in an IBE system, allowing for a highly customizable ion etching process [95, 96].

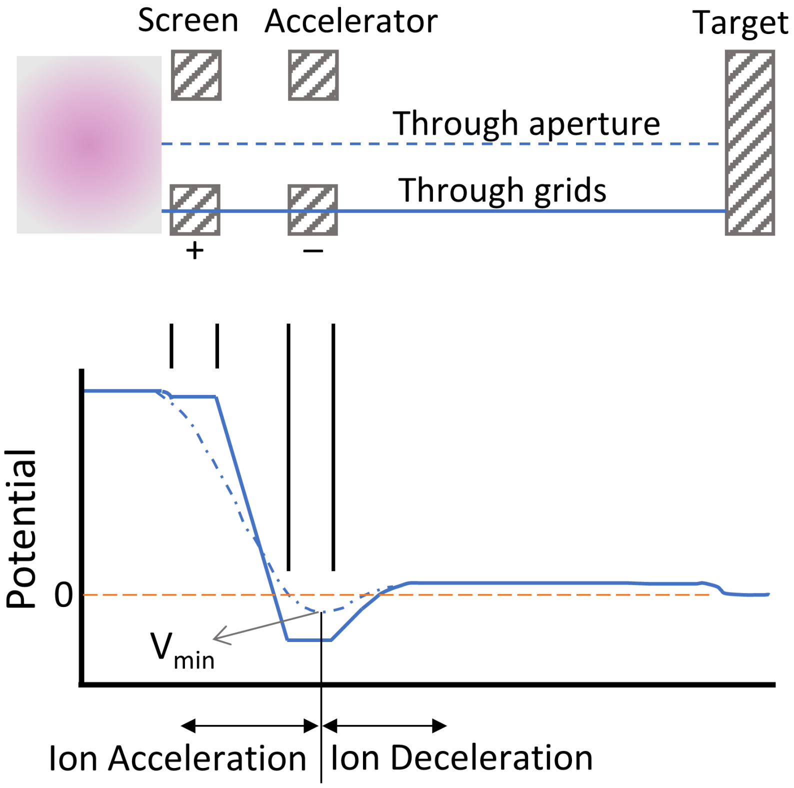

Figure 3.6: Potential variation through the grids and through the center of the aperture in an IBE chamber [95]. V_{min} is the minimum potential at the center of the accelerator grid aperture.

Reactive ion beam etching (RIBE) and chemically assisted ion beam etching (CAIBE) are two derivatives of IBE, particularly useful for etching materials that are hard to remove using physical sputtering and when selective etching is necessary. In an RIBE process, reactive gases are introduced into the discharge chamber instead of inert gases, and the reactive species in the ion beam etch the target substrate, as shown in Figure 3.5b. In a CAIBE process, inert gases inside the discharge chamber are used to create the ion beam, while reactive gases are separately directed into a gas ring close to the target substrate, independent of the ion beam, as shown in Figure 3.5c. The ion beam collides with the gas molecules in the gas ring to generate reactive species that etch the target substrate. While both RIBE and CAIBE processes produce desirable etch results, RIBE offers superior etch mask selectivity and wafer-scale uniformity [97], whereas CAIBE requires low maintainance for the ion source [95]. In this dissertation, we utilize an RIBE process involving SF_6 and O_2 gas with an SF_6:O_2 ratio of 4:1 in Intlvac Nanoquest II, to etch triangular cross-section photonic devices in SiC.

3.6 Optical Characterization

Photoluminescence (PL) is an optical characterization method used to investigate the optical properties of a color center by exciting the color center with above-band photons and analyzing the photons emitted during the color center's spontaneous relaxation. Above-band excitation (pump laser) is achieved using either a 785 nm continuous-wave (CW) laser or a 1080 nm picosecond pulsed laser. The pump laser is incident on a dichroic beamsplitter, which reflects the wavelengths of the pump laser and transmits the color center emission wavelengths. The pump is then directed onto a XY rotating mirror (Newport FSM-300 fast steering mirror), allowing for the scanning of randomly positioned color centers in the sample. A 4f confocal setup comprises a mirror, two lenses (focal length f), and a microscope objective, which is used to precisely translate the rotation by the FSM onto the sample. In a 4f configuration, a total length of 4f is achieved by placing the first lens 1f away from the FSM-300 mirror, the second lens 2f from the first lens, and the microscope objective 1f from the second lens.

The excitation light passing through the objective lens is incident on the sample placed inside a Montana Cryostation (XP-100) model, which features a 2-inch diameter sample space and a base temperature of 1.56 K. The microscope objective is housed inside the vacuum shroud, enabling the utilization of an objective with a high numerical aperture of 0.85 to maximize collection efficiency. The incident excitation light results in emission from the color centers in the sample, which is collected by the same objective lens and traces the same path as the excitation laser. At the dichroic beamsplitter, the color center emission light is transmitted through the dichroic to be coupled into the fiber, which can then either connect to a spectrometer or the superconducting nanowire single photon detectors (SNSPDs) in the cryostat. The schematic of the setup is shown in Figure 3.7. The emission spectrum is captured using a spectrometer, while SNSPDs are employed to measure lifetimes. The SNSPDs, fiber feed-through, and SNSPD control electronics employed are from Quantum Opus and have maximum efficiency at 1310 nm, functioning at temperatures of 2.5 K or lower. The SNSPDs were integrated into the same cryostat as the sample, enabling the construction of an Integrated Cryogenic system for Emission, Collection And Photon-detection - ICECAP [98].

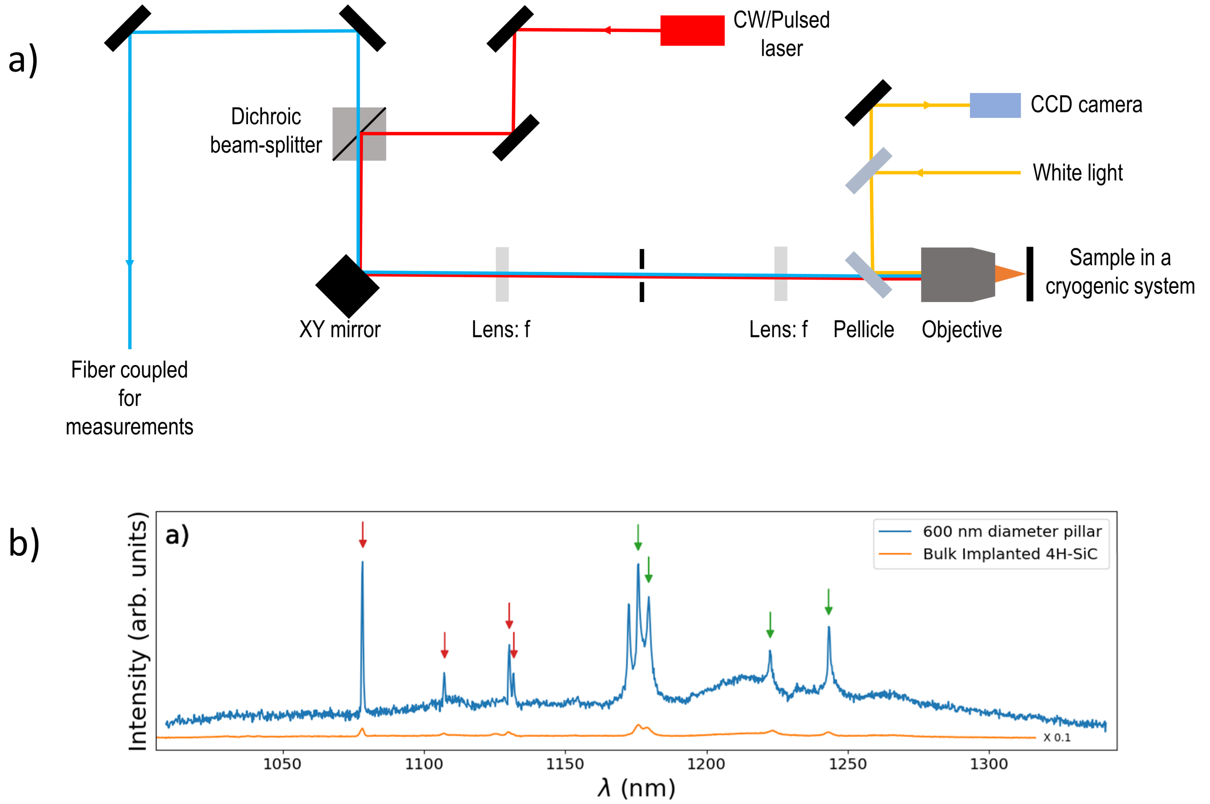

Figure 3.7: a) Two-dimensional scanning 4f confocal microscopy setup. b) Photoluminescene spectrum of NV centers in 4H-SiC measured using the 4f confocal microscopy setup [98].

Chapter 4

Triangular Waveguides and Photonic Crystal Cavities

Waveguides and photonic crystal cavities improve light collection and emission efficiency, respectively, for color centers integrated into them. In this chapter, we analyze the optimal positioning of color centers within the modes of these devices and provide estimates on achievable Purcell enhancement in nanocavities with applications in quantum communications. These results are part of the publication titled "Quantum photonics in triangular-cross-section nanodevices in silicon carbide" [99].

4.1 Triangular cross-section SiC waveguide

A waveguide uses total internal reflection to confine propagating light in the high refractive index material. The triangular cross-section waveguide modeled in this study using Finite-Difference Eigensolver (Lumerical MODE) was parameterized by the wavelength to the top-width ratio λ/d and the half-angle α. The fundamental TE and TM modes were studied for $0.5 \leq \lambda/d \leq 2$ and $30^\circ \leq \alpha \leq 40^\circ$ with obtained mode profiles shown in Figure 4.1.

To find the optimal positioning of the color center in the waveguide, we analyzed the depth h at which the electric field intensity maximum ($|E|^2_{\max}$) of a mode is positioned relative to the waveguide's top plane. As λ/d increases, $|E|^2_{\max}$ for the fundamental TE

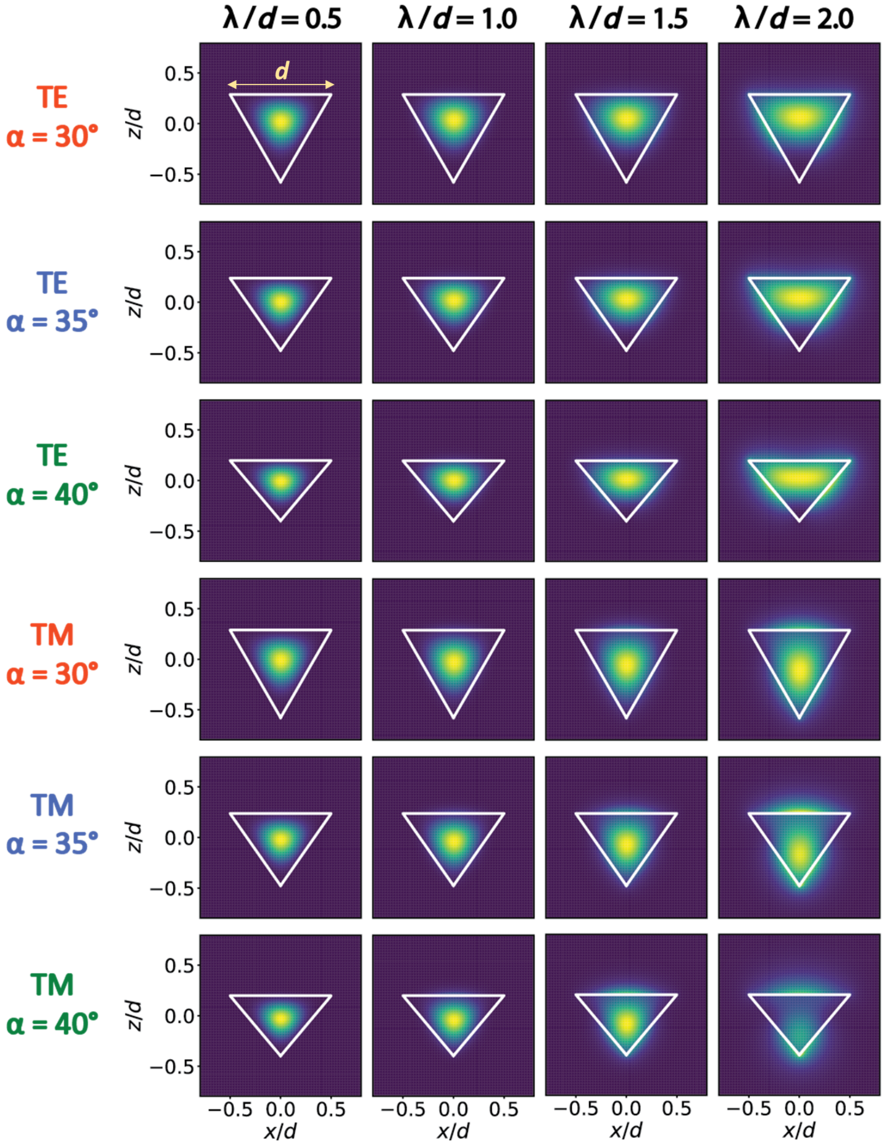

Figure 4.1: Electric field intensity profiles $|E|^2$ of TE and TM polarized modes supported by triangular-cross-section SiC waveguides with $0.5 \leq \lambda/d \leq 2$ and $30^\circ \leq \alpha \leq 40^\circ$. A mesh dimension of 10 nm was used in the x, y, z directions and a constant width $d = 0.754$ μm was used. Color bar is the same as in Figure 4.4.

(TM) polarized mode shifts towards (away from) the top waveguide surface i.e., the depth h decreases (increases). This behavior is consistent for all studied half-angle values α, as shown in Figure 4.2a. For higher values of λ/d, the mode becomes less confined and the evanescent losses into the surrounding medium dominate, as can be observed in mode profiles in Figure 4.1. These observations are consistent with the trend in the effective refractive index (n_{eff}) values shown in Figure 4.2b. The effective refractive index for a mode is given by the ratio of propagation constant of that mode (β) to the wavenumber in vacuum (k_0). When $n_{\mathrm{eff}} \sim 1.5$, significantly below the SiC refractive index $n = 2.6$, $|E|^2_{\mathrm{max}}$ for the TM mode lies outside the waveguide and results in a lossy propagation. These results give an understanding into the range of half-angle and λ/d values suitable for fabricating triangular cross-section waveguides that are able to couple the fundamental TE/TM modes with other photonic elements.

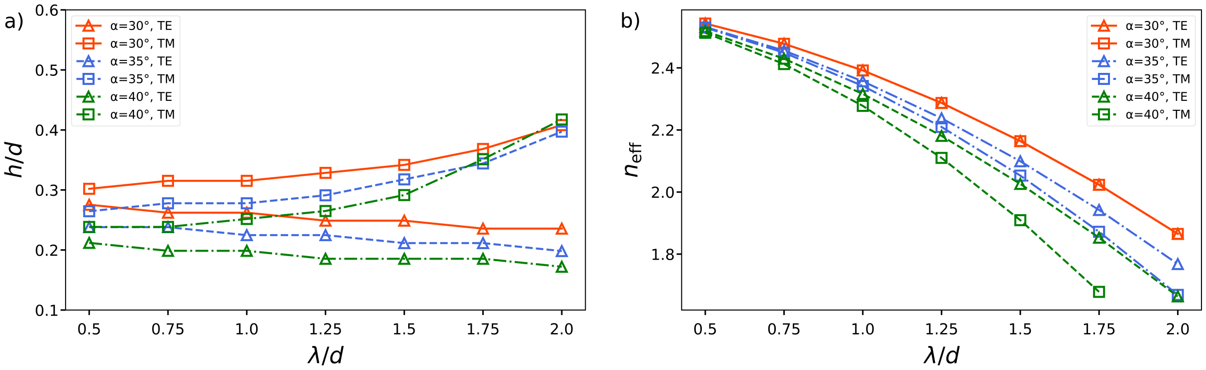

Figure 4.2: Normalized depth h/d of the electric field intensity maximum $|E|^2_{\mathrm{max}}$ and the effective index of refraction of TE and TM modes supported in a triangular-cross-section SiC waveguide, as a function of the geometry parameters.

4.2 Triangular cross-section SiC photonic crystal cavity

Photonic crystal cavities are nanostructures with periodic variation of refractive index which localize photons to sub-wavelength mode volumes. The triangular nanobeam photonic crystal cavities explored in this study have elliptical air holes whose major axis radius is tapered along the device, which have proved successful in diamond color center research in achieving ultra-high Q-factors and ultra-small mode volumes [100, 101] and more importantly, offer better mode confinement and scalability than the well-explored methods. As shown in Figure 4.3, the cavity has a width $d = 1.94a$ and consists of 30 through holes on either side of the center of the cavity with uniform spacing between the holes, lattice constant $a = 387.8$ nm. The minor radius of the holes is $0.292a$ and to minimize scattering and maximize Q-factor, the major radius is quadratically varied from $r_1 = 0.486a$ to $r_{30} = 0.292a$ over 30 holes. The beam has a triangular cross-section with a half-angle $\alpha = 35°$.

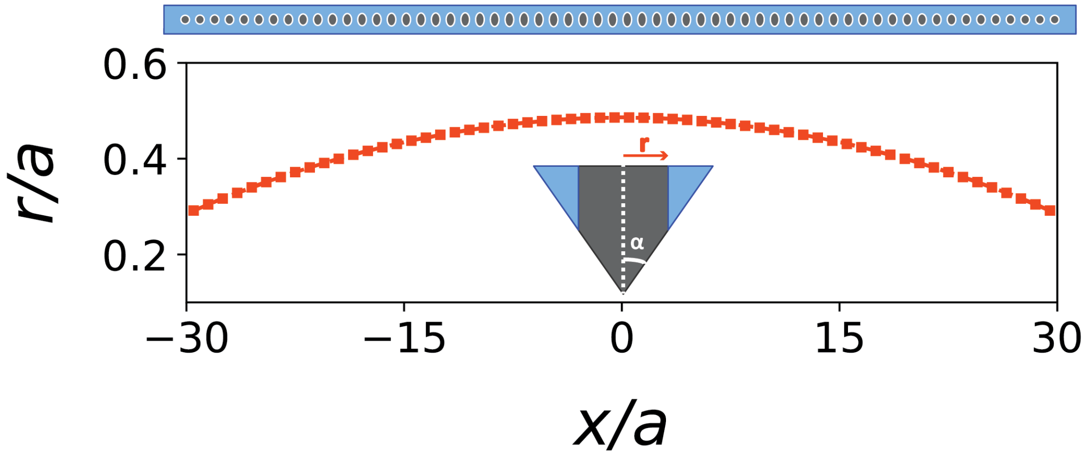

Figure 4.3: Triangular nanobeam cavity structure and the parabolic variation of its hole's major radius r along the length of the beam.

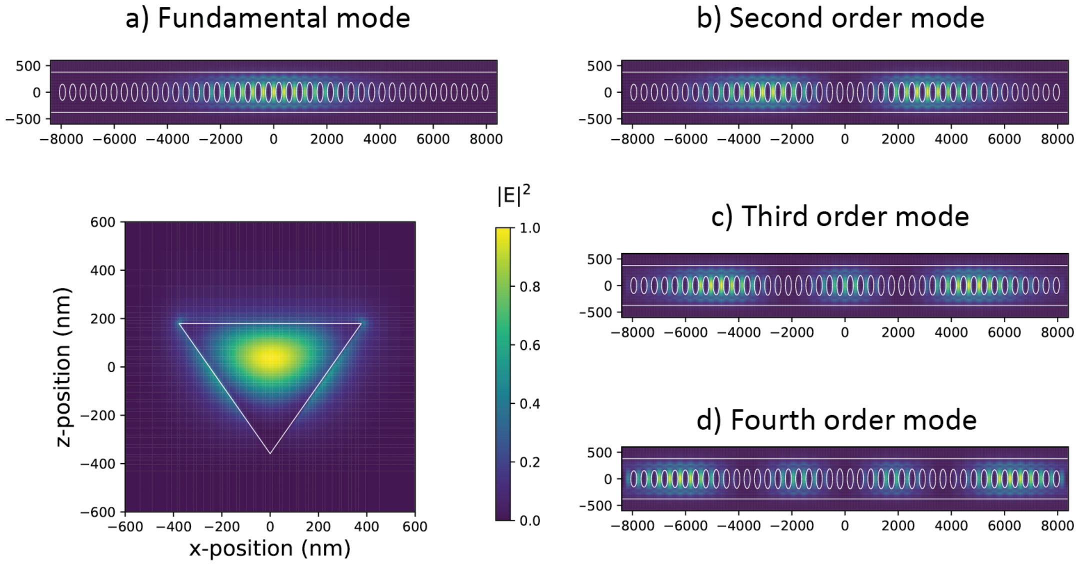

Figure 4.4: a) The top and the cross-sectional profile of the fundamental resonant mode. b-d) Top-view profile of the first three higher order modes in the cavity.

The optical response of the triangular nanobeams was modeled using the Finite-Difference Time-Domain method in the Lumerical FDTD software package. In the simulations, SiC was defined as a dielectric with a constant refractive index $n = 2.6$. The electric field profile of the fundamental mode is shown in Figure 4.4a. The fundamental cavity resonance occurs at $\lambda = 1324$ nm with a quality factor of $Q \sim 1.05 \times 10^7$ and mode volume of $V \sim 2(\lambda/n)^3$. Higher order TE-polarized longitudinal modes, useful for nonlinear optics processes involving multiple modes such as frequency conversion [40, 102–104], are also supported in the cavity, as shown in Figure 4.4b-d, where the cross-sectional profile is representative of the profiles of the electrical field nodes in all modes. Cavities with half-angle $30° \leq \alpha \leq 40°$ were simulated while maintaining the lattice constant and radii of the holes. It was observed that the resonant wavelength of the fundamental mode decreased with increasing α, whereas the Q-factor and mode volume remained almost the same, as shown in Figure 4.5. The impact of a changing lattice constant was studied across a range of 100 nm, which tuned the resonant wavelength from 1200 nm to 1500 nm, as shown in Figure 4.5. The Q-factor and mode volume of the fundamental resonance for varying values of a remained nearly constant (less than a factor of 2 for Q and within 10% for V). Thus, for different technological implementations of the inclines in angled etching, this tapered-hole design of a photonic cavity can be used to integrate various SiC color centers in the telecommunications wavelength range with strong Purcell enhancement of $F_{\max}$ in the range of 2.7×10^5 - 5.3×10^5 when the spatial and spectral overlap terms are unity. Figure 4.6 compares the simulated Q and V values in this work to other photonic crystal cavities fabricated in SiC. The cavities without emitters achieved quality factors up to 630,000 [44, 105–111] and those with emitters achieved up to 19,300 with Purcell enhancement up to 120 [39–42, 72], showing that our design bridges the gap between color center platforms and high Purcell enhancement devices.

Triangular photonic crystal geometry lends itself well toward the 1D coupled cavity array fabrication. To study the coupling between the neighboring cavities, a photonic crystal molecule was designed by stacking two photonic crystal cavities side-by-side with a reduced number of holes in the interior ($M < 30$) as shown in Figure 4.7a. The major axis radius of the M holes is tapered using the same parabolic variation as the 30 holes with the M largest holes kept and 30-M holes discarded. The coupling between the two cavities causes the resonant mode splitting. We observe in the transmission spectra

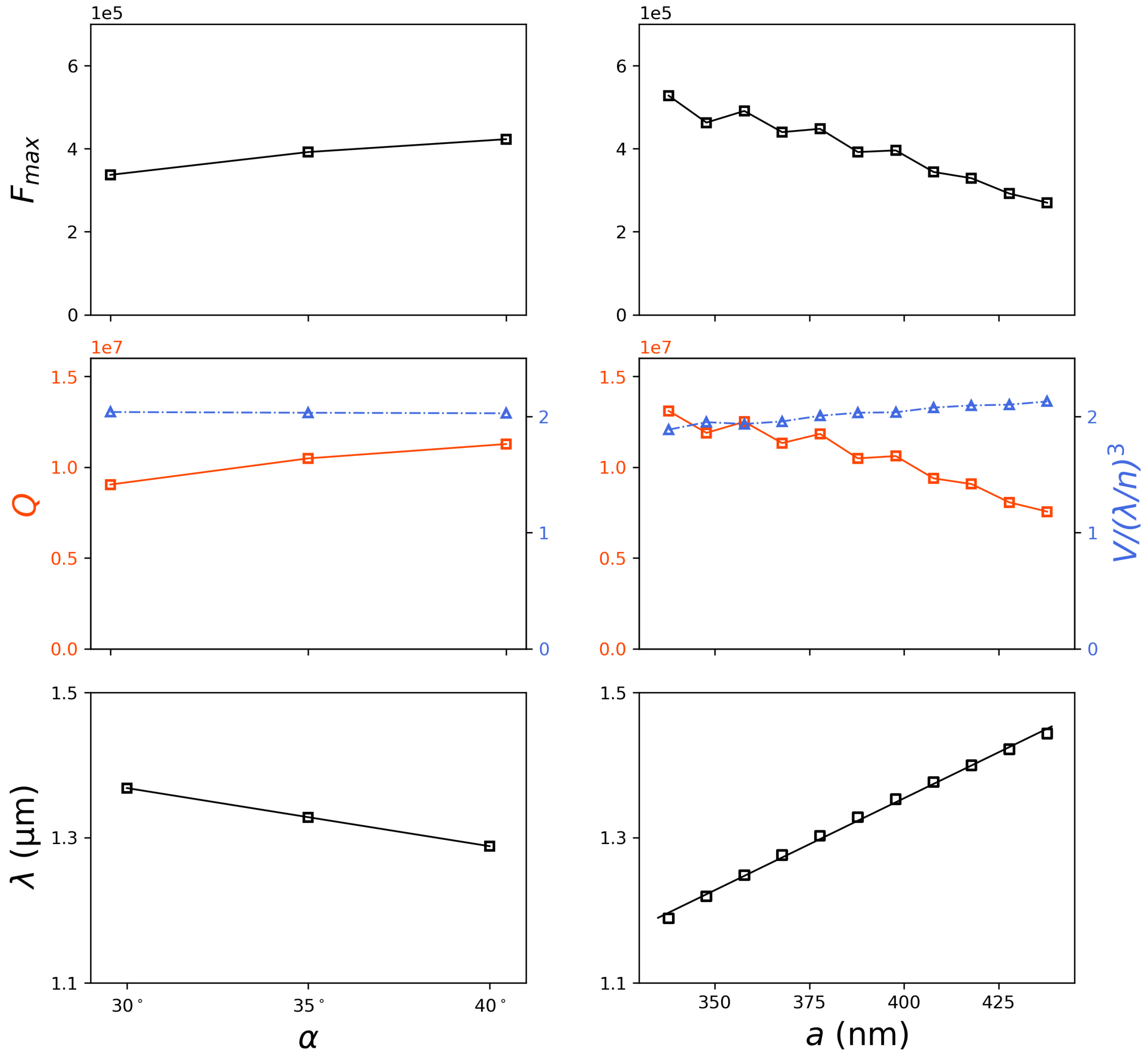

Figure 4.5: Dependence of the resonant wavelength λ, the quality factor Q, the mode volume $V/(\lambda/n)^3$ and the maximum Purcell enhancement F_{max} on the half-angle α of the triangular cross-section and the lattice constant in the triangular nanobeam SiC cavity.

that as the separation between the two cavities is reduced (M decreases), the coupling strength between the cavities represented in the wavelength separation between the two resonances increases [112]. By integrating emitters into the photonic crystal molecule, the designed structures can be employed for investigation of cavity Quantum Electrodynamics (cQED) effects [113]. Using open quantum system modeling, we find that the simulated nanocavities and photonic molecules are strong candidates for quantum information and simulation platforms [99].

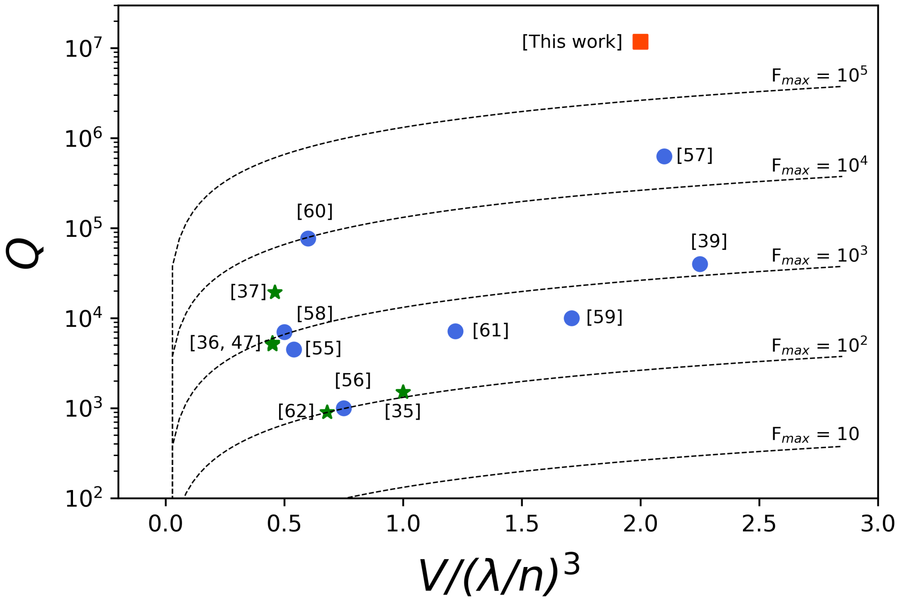

Figure 4.6: Comparison of experimentally demonstrated Q and V values of photonic crystal cavities in SiC - without color centers (blue circles) [44, 105–111], with integrated color centers (green stars) [39–42, 72] and simulated value at 1300 nm in this work (red square). The dashed black lines indicate the different regions of maximally achievable Purcell factor values.

4.3 Discussion

Our modeling results provide insights into color center integration with triangular SiC photonic devices, as well as quantum optical phenomena in cavity QED systems. This geometry is of great interest because it overcomes the limitations of color center platforms requiring implementation in bulk substrates.

Triangular-cross-section waveguides are found to efficiently guide the light emission from color centers embedded at optimal depths. The waveguides support propagation of both TE and TM polarized modes, thus serving a variety of color center crystalline orientations. Fabrication imperfections in the curvature of the apex affect only the modes present in the lower half of the triangular cross-section. Similar designs fabricated in diamond have successfully combined triangular waveguide geometry with suitable grating couplers for efficient collection of light into a high numerical aperture objective, as well as tapered down for coupling to an optical fiber [114]. They can also be designed for

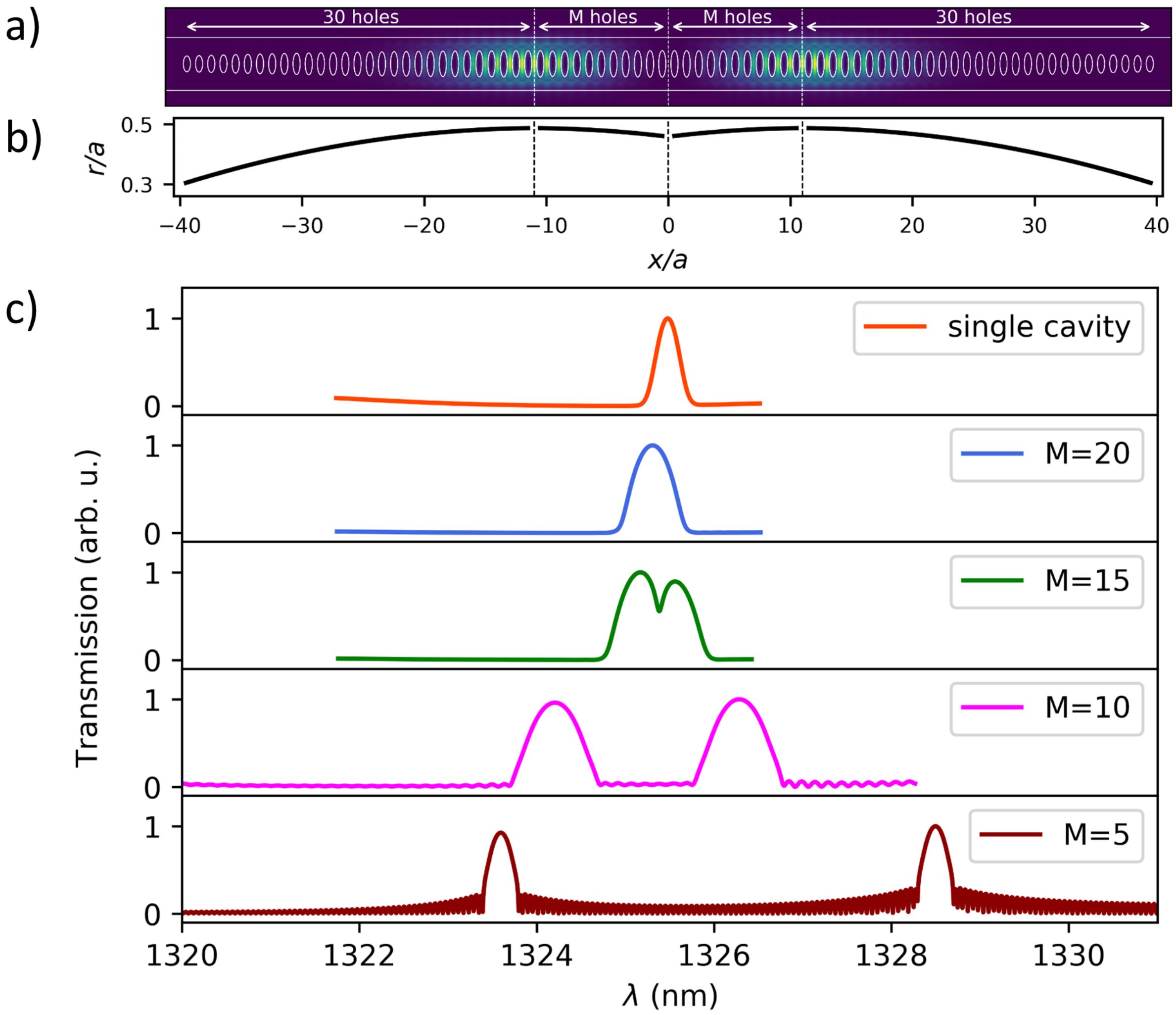

Figure 4.7: a) Top-view profile of the resonant mode of the photonic molecule. Color bar is the same as in Figure 4.4. b) Variation of r along the length of the beam. c) Transmission spectrum of a photonic crystal molecule connected via $2M$ holes, in comparison with a single cavity case.

integration with the emerging superconducting nanowire single-photon detectors [115].

The modeled triangular nanobeam photonic crystal cavities have high Q/V ratio with promising applications in high-speed and indistinguishable photon generation. For the same triangular geometry, altering of the lattice constant is found to tune the resonant wavelength without reduction in the quality factor, meaning that many different high-performing devices can be simultaneously fabricated on the same chip. Interestingly, in literature on diamond and SiC nanobeam devices, the fabricated quality factors fell 2-3 orders of magnitude short of their theoretical predictions [44, 101]. The reduced performance can be attributed to fabrication errors such as mask alignment imperfections [44].

This indicates that additional efforts in nanofabrication process development need to be invested to realize the full application potential of these designs. Purcell enhancement of the zero-phonon line emission would play a crucial role in realizing quantum systems that require two-photon interference and quantum entanglement, such as quantum repeaters [116] and cluster-entangled states [117, 118]. The photonic crystal cavities modeled in this work potentially provides a tie-in between high Q/V designs and platforms that host color centers, a necessary step for color center-based quantum information technologies in SiC.

The open quantum system modeling of a single nanocavity and a photonic crystal molecule integrating non-identical color centers confirmed that cavity-protection effects can support polariton physics even in the presence of realistic inhomogeneous broadening in SiC structures. Extensions to larger 1D coupled-cavity-arrays can provide a simulation testbed for proposals of strongly-correlated systems, such as the 1D Mott insulator to superfluid transition [119], and could be extended to waveguide QED simulations of the many-body localization phase [120].

Our simulations of triangular cross-section waveguides and cavities in 4H-SiC demonstrate that this geometry can achieve similar figures of merit (e.g. $Q \sim 10^6$) as other state-of-the-art geometries in both 4H- and 3C-SiC polytype. Since, the thickness and width of these devices are related through the etch angle, global scaling is possible without affecting the figures of merit as much. The benefit to our approach is that 4H-SiC can host color centers without damaging the lattice unlike 3C-SiC and the geometry is highly scalable using angle RIE etching unlike some of the more complex 2D photonic crystal cavities. In fact, triangular cross-section nanophotonics have already been successfully fabricated in diamond; the work already performed in diamond has illuminated some shortfalls in nanofabrication that need to be overcome before we can fully realize our simulated results. The prior experiments and our work in this paper pave the way toward high quality, color center integrated, highly scalable nanophotonic devices in 4H-SiC.

Chapter 5

Triangular Waveguides for Integration of Silicon Vacancy Centers in 4H-SiC

Color centers, despite their excellent spin-optical properties, encounter a challenge in preserving these properties upon integration into nanophotonic structures. This degradation is caused by coupling to nearby spins and charge traps, which are present in the material or generated during nanofabrication [39, 121–125]. This makes wavefunction symmetry-protected color center, such as the silicon vacancy in 4H-SiC [126, 127], a promising candidate for nanophotonic integration. Moreover, the silicon vacancy center has other attractive properties, like millisecond spin-coherence times [128] and coherent coupling to nuclear spins [27].

The negatively charged silicon vacancy (${V_{Si}}^{-}$) in SiC is formed at the site of a missing Si atom in the lattice and is a spin-3/2 defect. In 4H-SiC, ${V_{Si}}^{-}$ has two inequivalent lattice sites (h, k), resulting in emission spectrum consisting of two ZPLs i.e., V1 (861.6 nm) and V2 (916.5 nm) [50, 51]. This chapter presents collaborative work on nanophotonic integration of silicon vacancy color centers in 4H-SiC into triangular waveguides. Our collaborators fabricated triangular cross-section waveguides in 4H-SiC using Faraday cage-assisted angle etching method with integrated ${V_{Si}}^{-}$ generated through He^{+} implantation [29]. The experimental results demonstrate that the intrinsic spin-optical properties of the silicon vacancy did not degrade upon integration into the triangular cross-section waveguides. I was the lead researcher in modeling the optimal waveguide design to achieve maximum color center emission coupling for each α, at the emission wavelengths of V2 center (916 nm). Additionally, we explored the dependence of waveguide coupling on the emitter position within the waveguide to explain the experimental observations. These results are part of the publication titled "Fabrication and nanophotonic waveguide integration of silicon carbide colour centres with preserved spin-optical coherence" [29].

5.1 Optimized waveguide design

In this section, we discuss ideal waveguide designs based on the demonstrated implantation and nanofabrication techniques. In color center integration with triangular waveguides, highly efficient single-mode light propagation is a crucial prerequisite for quantum applications. The relationship between device profile and its supported mode wavelength has been modeled recently [125]. Here, we expand on those findings to propose efficient design guidelines for V2 center emission propagation, robust to the demonstrated implantation uncertainties. In particular, we analyze the coupling efficiency of light emitted by a centrally located horizontal dipole at 917 nm into the transverse electric (TE) modes of a triangular waveguide. We find the existence of the preferential waveguide width d for each studied etch angle α, as presented in Figures 5.1, 5.2a. Interestingly, the mode shape of the optimal device appears more rectangular than circular, and localized within silicon carbide. For the waveguides fabricated in this work ($\alpha = 45°$, d = 1000 nm) the coupling efficiency into the fundamental TE mode is approximately 30% (15% in each propagation direction in the waveguide). The efficiency would rise to 82% if those waveguides were minimized to 500 nm width. We note that these coupling efficiencies assume a defect in the center of the waveguide, i.e., at a depth of 125 nm along the vertical symmetry axis of the devices with $\alpha = 45°$ and d = 500 nm. Figures 5.1, 5.2a show additional results for V2 centers positioned in at the center of different waveguide geometries ($\alpha = 30°$ - 75°, d = 400 nm - 1000 nm). Devices with optimal collection efficiency are highlighted by a red box in Figure 5.1. Figure 5.2a shows further that waveguides with steeper etching angle

α provide high optimal efficiencies over a larger range in d.

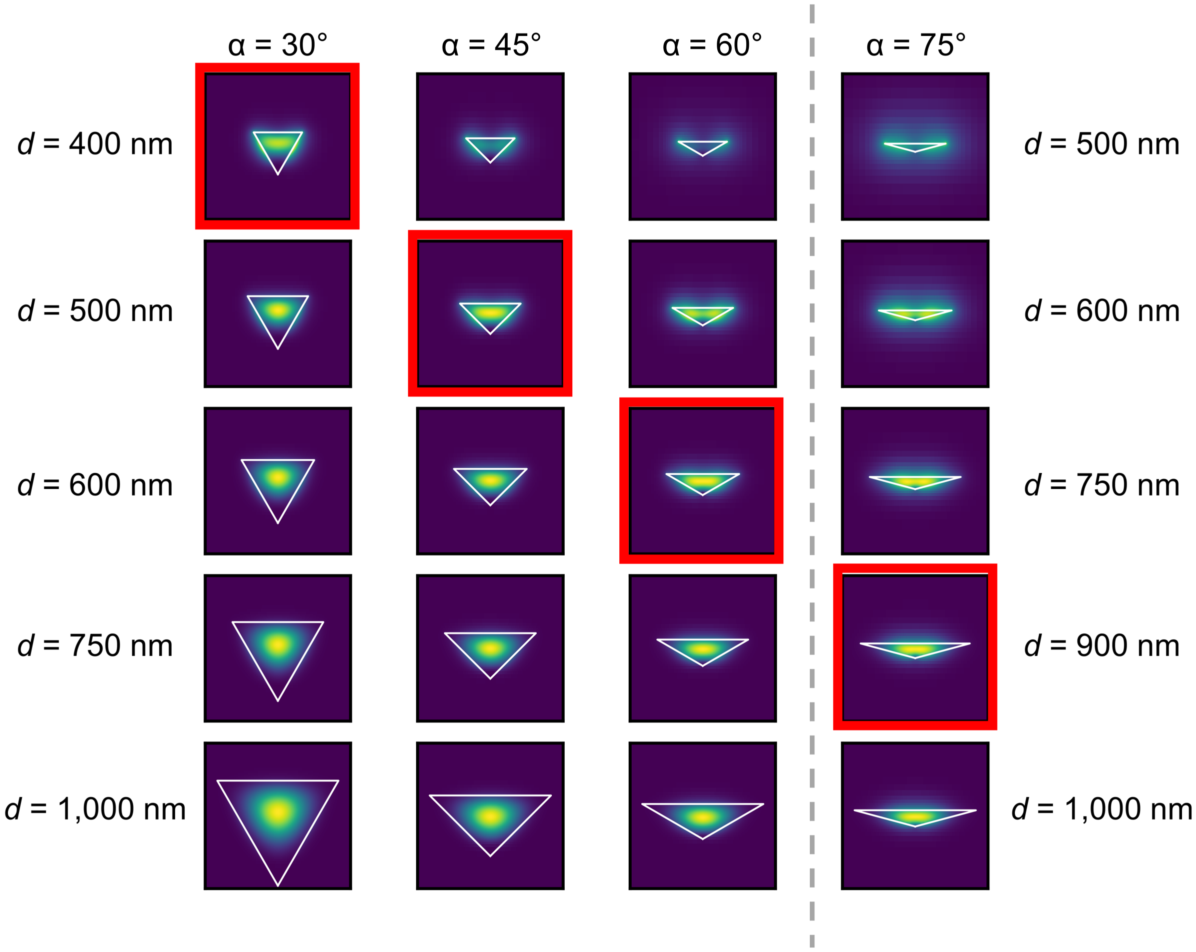

Figure 5.1: TE mode profiles of triangular waveguides with variable etch angle α and width d. Highest waveguide-coupling efficiency is achieved for the devices that are highlighted by a red box.

To account for the demonstrated He^+ ions implantation technique that results in a preferred V2 center creation at 30 - 40 nm depth, we now provide additional simulation results to identify the optimal geometry. As presented in Figure 5.2b, the coupling efficiency does not change significantly in the investigated depth range (d = 30 - 40 nm). Devices with higher etch angles result in consistently better coupling efficiencies (up to 80%). Remarkably, the $\alpha = 75°$ devices show very robust coupling efficiencies, especially with regards to the waveguide width d = 900 - 1000 nm, as shown in Figure 5.2b. We also consider the demonstrated lateral defect creation accuracy which was determined to be ±54 nm in this work and mainly limited by the implantation mask's hole size (100 nm

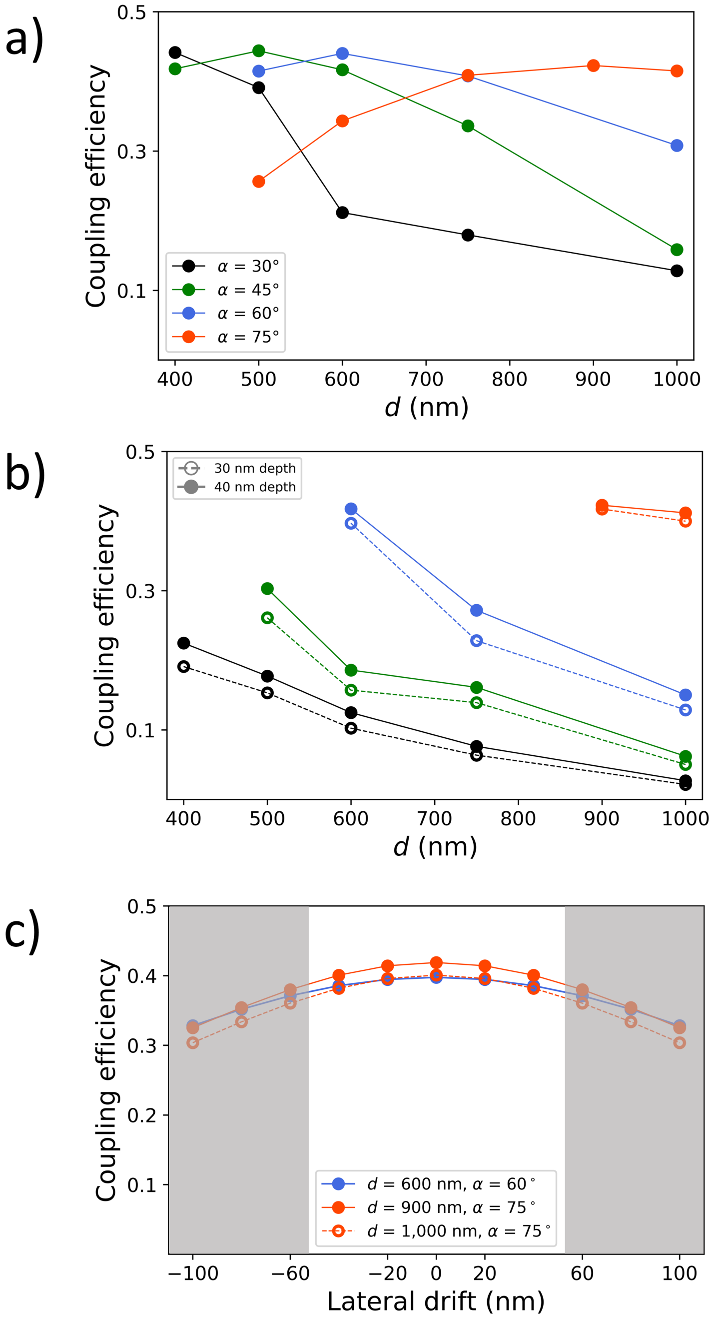

Figure 5.2: a) The coupling efficiency of light emitted by a centrally located V2 center for variable waveguide geometry. b) The coupling efficiency of light emitted by a V2 center on the vertical symmetry axis for variable emitter depth and waveguide geometry; the color legend in a applies to the plot. c) The coupling efficiency of light emitted by a 30 nm deep V2 center laterally shifted from the central position for variable waveguide geometry.

diameter). As shown in Figure 5.2c, lateral displacement of the emitters does not play a significant role, i.e., fundamental TE mode coupling efficiencies remain within 10% of their peak value. The lost photons couple to the fundamental transverse magnetic (TM) mode and can, in practice, be filtered out by polarisation.

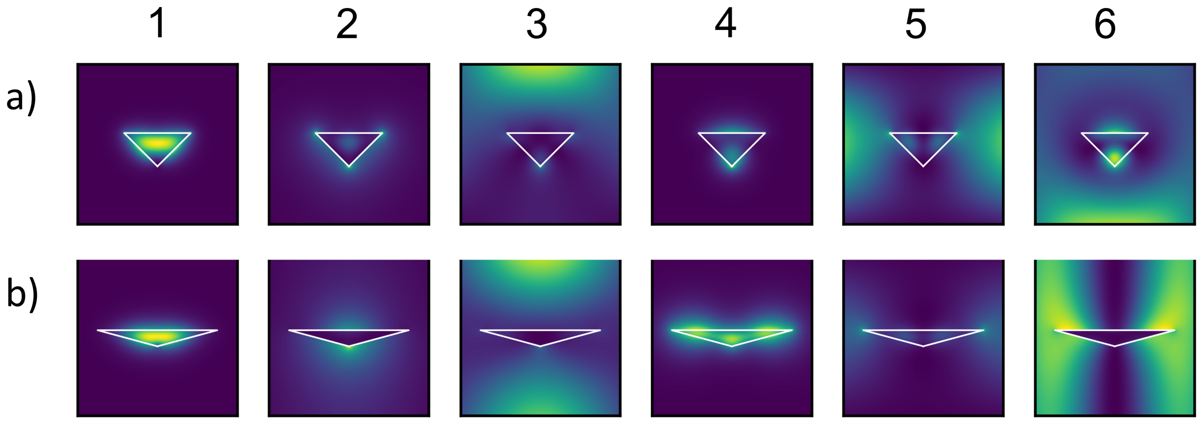

Figure 5.3: Single mode operation of optimized triangular waveguides. a) Profiles of the six lowest energy modes supported in a triangular waveguide with etch angle $\alpha = 45°$ and width d = 500 nm and b) etch angle $\alpha = 75°$ and width d = 900 nm; mode #1 is the fundamental TE polarized mode.

For optimal coupling of light out of the waveguides into single-mode optical fibres, it is important to ensure single TE mode operation. To this end, we simulate the first six TE modes for devices with ($\alpha = 45°$, d = 500 nm) and ($\alpha = 75°$, d = 900 nm), respectively. The results are shown in Figure 5.3a and b, respectively. The coupling efficiency of from a 30 nm deep emitter to the different modes and varying d is shown in Figure 5.4a and b, respectively. We find that both preferred geometries ($\alpha = 45°$, d = 500 nm) and ($\alpha = 75°$, d = 900 nm), provide $\sim 80\%$ coupling efficiency into the first TE mode without noticeable excitation of higher-order modes.

Our modelling results show that the demonstrated Faraday cage etching techniques and He^+ ion implantation provide a rich toolset for integrated SiC color center photonics. The single TE mode operation of triangular waveguides is highly efficient and robust in multiple degrees of freedom: vertical and lateral emitter displacement, fabrication dimension and surface roughness imperfections. Moreover, these waveguides can be coupled to triangular photonic crystal cavities which are known to provide strong Purcell enhancement utilized to boost the generation of indistinguishable single photons in color centers [114, 125, 129].

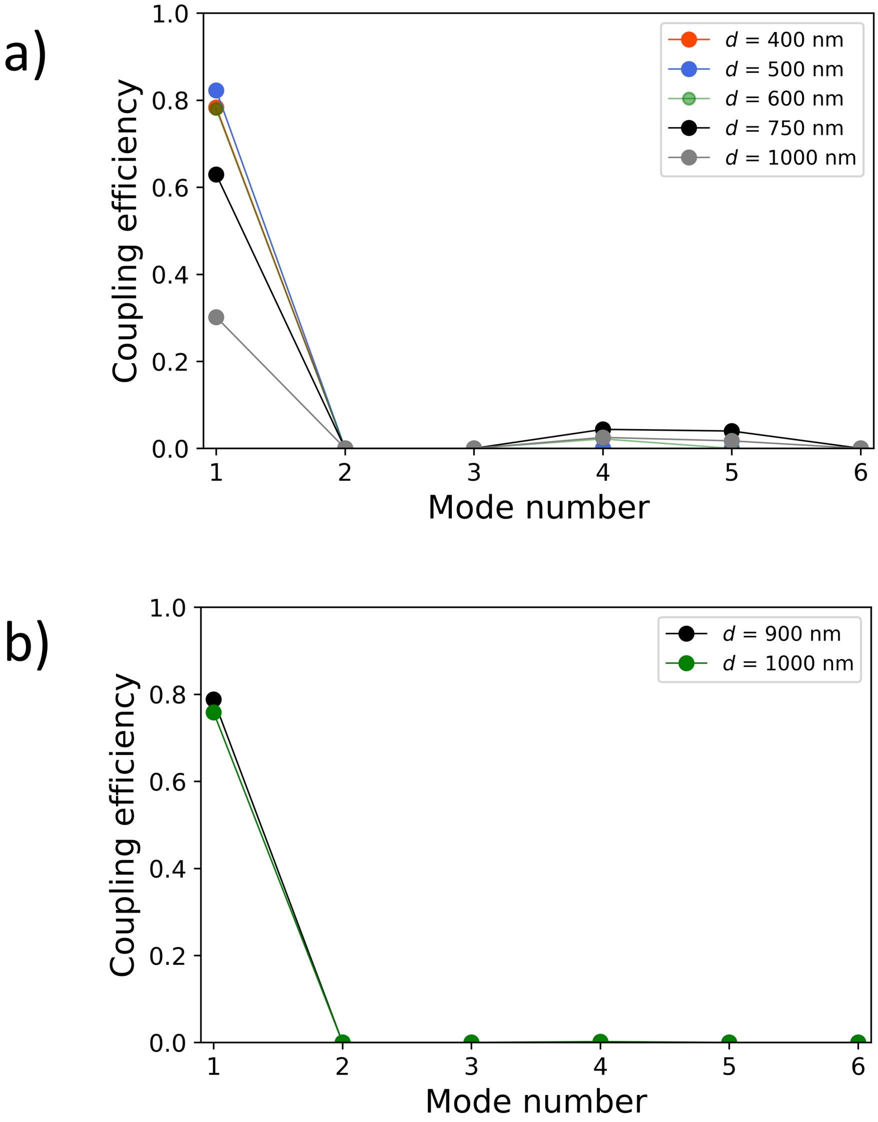

Figure 5.4: a) The coupling efficiency of light emitted by a centrally located horizontally polarized dipole into each of the modes shown in Figure 5.3a; the coupling efficiency is evaluated after 10 μm propagation. Single mode operation is observed for waveguide widths of 400 nm and 500 nm. b) The coupling efficiency of light emitted by a 30 nm deep horizontally polarized emitter to each of the modes shown under Figure 5.3b showing single mode operation.

5.2 Photonic coupling in the waveguide

Finite-Difference Time-Domain (FDTD) method is particularly suitable for simulating the expected performance of nanophotonic devices, processes, and materials. This method models the propagation of light by discretizing Maxwell's equations in both time and space coordinates in a leap-frog manner. Owing to high accuracy and broad-frequency response, FDTD method has been widely used as a verification tool for photonic devices over the years. Moreover, FDTD method has been employed to simulate nanocavities in triangular diamond waveguides [129, 130]. Recently, we have used FDTD modeling to analyze color center positioning and Purcell enhancement in triangular SiC waveguides and nanobeam cavities [125]. In this work, as well as in the present manuscript, we have used Lumerical software to perform 3D FDTD electromagnetic simulations, an accurate and widely used tool in academia and industry.

In an attempt to infer the photonic coupling efficiency along the waveguide using our present optical arrangement (collection objective from the top), we performed additional experimental and simulation studies. The basic idea was to infer saturation count rates from V2 centers in the bulk and compare these count rates to emitters in waveguides. Assuming that the total photon emission rate in both cases does not change, and comparing with results from simulations, would then allow to confirm photonic coupling into the waveguide.

Our FDTD model assumes a horizontal dipole emitter in a SiC triangular waveguide (or bulk) studies the light propagation equivalent to the experimental setup. The collection of light into an objective of NA = 0.9 is calculated in a two-step analysis. In the first step, the fraction of light that leaves silicon carbide upwards is evaluated. In the second step, Fourier transform of the electromagnetic field above the structure produces the far-field pattern in k-space, and can be used to calculate the fraction of light that enters the NA = 0.9 objective. The modelling results support the experimental findings and are detailed in Figure 5.5.

In the next step, we performed simulations on the out-coupling efficiency for defects located in 45° underetched 1000 nm wide waveguides. We found that the collectable photon rate depends very strongly on the exact location of the emitter in the waveguides, see Figure 5.6.

Considering the large variability of achievable collection efficiency and the limited accuracy towards inferring each defect's precise position inside the waveguide, made it impossible to faithfully measure the saturation count rate, which was therefore not at-

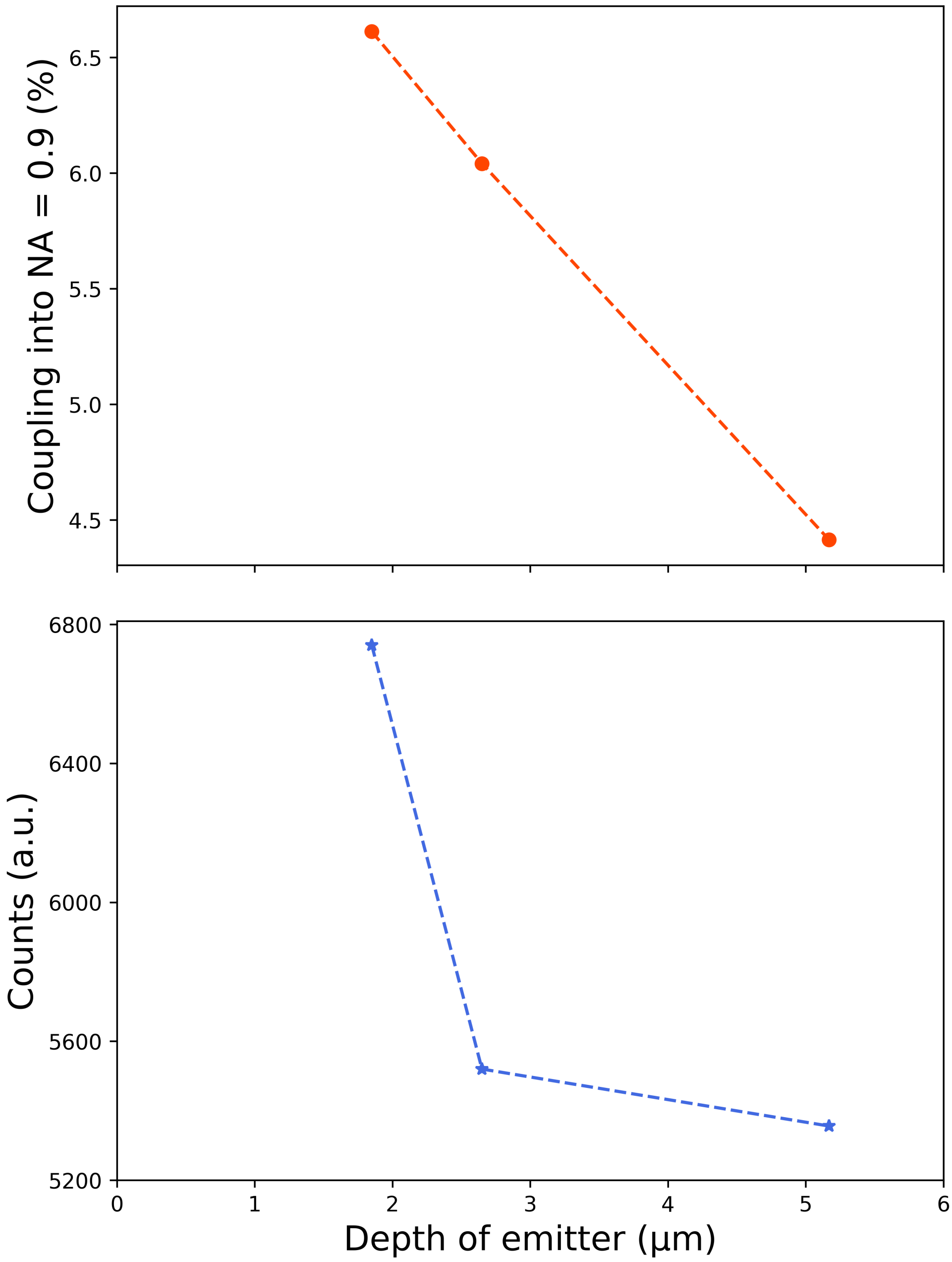

Figure 5.5: Model of an emitter in bulk. The model of a silicon vacancy in SiC bulk at arbitrary depth (top) shows a decreasing trend in collected photons with the increasing depth of the emitter. Experimental results (below) show a similar trend.

tempted.

These simulations provide also a plausible explanation for the observation of less V2 centers in the waveguides compared to the defect density in the bulk. In this sense, we note that we only identify V2 centers that are bright compared to the waveguide's background fluorescence. This means that we observe only these defects that are placed at

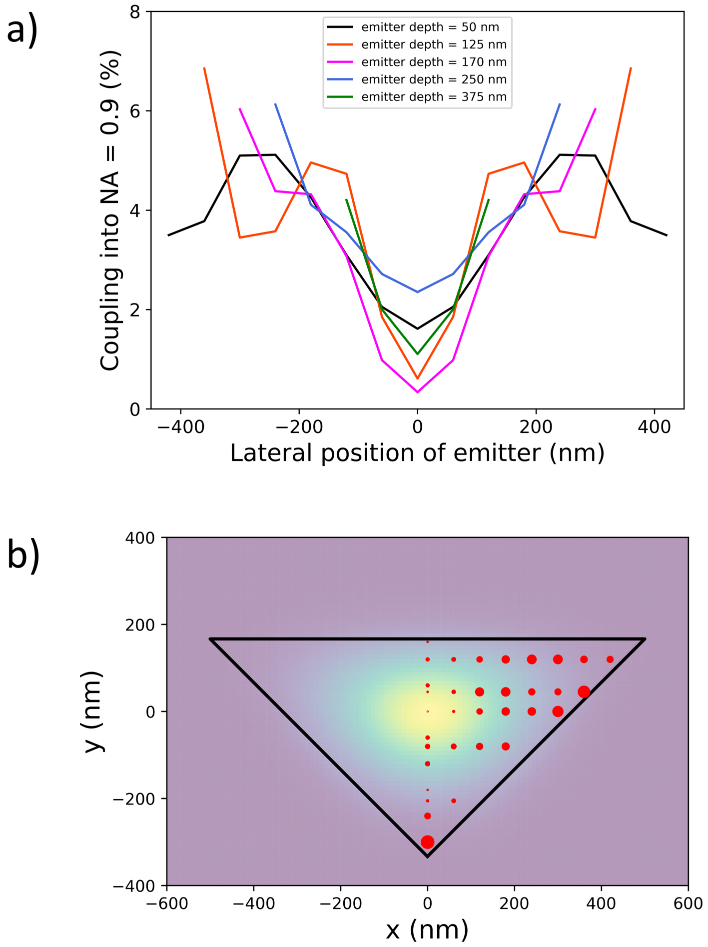

Figure 5.6: a) Model of an emitter in a triangular waveguide. The model of a silicon vacancy in a triangular SiC waveguide reveals that collection efficiency into an objective is higher at the edges of the structure than in its center. This data supports the experimental findings where emitters are identified at the sides of the structure [29]. b) A plausible explanation is that the emitters that couple to the fundamental mode do not scatter light toward the objective. The red dot size is proportional to the light collected by the objective for emitter at that location.

ideal positions in the waveguide, notably those that are close to the waveguides' apices, see Figure 5.6. It is thus very likely that the actual density of negatively charged V2 centers is not modified significantly in the waveguides. As the observed V2 centers show stable optical lines and no ionization, this could indicate that bandbending near the surfaces and edges is not significant.

Chapter 6

Triangular Photonic Devices with Integrated Detectors

Efficient collection and detection of color center emission are key for implementing large-scale quantum information processing technologies. In this chapter, we explore efficient collection and detection in a triangular cross-section SiC waveguide by introducing a photonic crystal mirror (PCM) on its one side and a superconducting nanowire single photon detector (SNSPD) on the other. The optimal nanowire geometries for efficient detection of light from transverse electric and transverse magnetic polarized modes were modeled using the measured optical properties of NbTiN thin films sputtered on 4H-SiC, for the first time. These results are part of the publication titled “Triangular quantum photonic devices with integrated detectors in silicon carbide” [131].

6.1 Photonic crystals for efficient propagation of color center emission in a triangular waveguide

Color centers have an optical dipole-like emission covering a solid angle of 4π [52]. This causes 50 % higher than in spin-entangled photon loss in the triangular cross-section waveguide resulting in low collection efficiency. An *in situ* mirror, capable of reflecting color center emission, should theoretically double the collection efficiency. It is possible to design such a structure artificially by periodic variation of the dielectric contrast, known as the photonic crystal [132]. For enhanced collection, we deliberately open up a gap possessing the NV center emission wavelength in the photonic bands, which is achievable by making a particular choice of PC parameters [133].

Waveguides support light propagation in a particular direction via total internal reflection. We implement 1D PC in our triangular cross-section waveguide to introduce asymmetry for redirecting the color center emission. However, 1D PCMs have mostly been realized in conventional rectangular geometry [100, 134, 135], and photonics with triangular geometry has been focused on making efficient active photonic devices [99, 136, 137]. Photonic band structures in triangular geometry have not been studied in detail. In this light, our recent work provides an insightful explanation of the dispersion relations in SiC triangular geometry [138]. From the band structures obtained from Plane Wave Expansion (PWE) method, we use Finite-Difference Time Domain (FDTD) method to analyze the performance of the triangular-cross section 1D PCM and the dependence of the coupling efficiency to the waveguide mode on the emitter position with respect to the PCM.

6.1.1 Considerations for integrating color centers into triangular cross-section devices

Color centers in SiC have multiple orientations due to the presence of inequivalent lattice sites (h, k). The dipole orientations of the color centers can be parallel (silicon vacancy in SiC) or at an angle (NV center in SiC) to the crystal axis (c-axis). In a photonic device fabricated from commonly available 4H-SiC, grown along the c-plane, this would result in emissions strongly coupling to the fundamental TM (f-TM) mode [60]. On the other hand, it has been shown that using 4H-SiC grown along the a-plane, the color center emission can be predominantly coupled to the fundamental TE (f-TE) mode [52].

Triangular cross-section waveguides support f-TE/TM modes and other higher order modes [99]. The fraction of a color center emission coupling to a supported waveguide mode depends on the position of the emitter within the triangular cross-section. Highest coupling to a mode can be achieved by positioning the emitter at the maximum intensity point of that mode. The maximum intensity point of the f-TE mode is located approximately at the centroid of the triangle, which is an optimal color center position for achieving highest coupling efficiency to the f-TE mode [52, 99].

The depth of the centroid from the surface depends on the width and etch angle of the triangular cross-section waveguide. These dimensions can be decided on the basis of the implantation capabilities, to ensure that the implanted color centers achieve the highest coupling efficiency to the f-TE mode. For a given emission wavelength, a triangular cross-section waveguide has an optimal width at which it has single mode propagation (f-TE), with high ($> 80\,\%$) coupling to the f-TE mode [52]. Single mode propagation in the waveguide is key for applications in QIP [139, 140]. The optimal width of the triangular cross-section devices increases with the etch angle and emission wavelength. Hence, triangular cross-section devices with larger etch angles have more fabrication friendly dimensions. Moreover, they require shallow implantation depths, which causes less damage to the crystal and having an emitter closer to the surface is useful for SNSPD absorption. Advantages like single mode propagation with high coupling efficiency, less damage to the crystal and better detection in SNSPD outweighs the overall effect of the color center emission lost into the f-TM or other modes.

6.1.2 Waveguide design with TE and TM band gap

NV center emission in SiC has both TE- and TM-like components [35]. Therefore, a PCM with polarization-independence is necessary to increase collection efficiency. For broadband reflectivity, such a mirror must have as large a complete photonic band gap as possible [141, 142]. Single mode propagation [139, 140] and positioning of emitter at the centroid of the triangular cross-section [52, 99] ensures that most of the color center emission is coupled into the waveguide. It was shown that 45° etch angle has predicted the best results for the complete band gap [138]. But in this study, an etch angle of 60° was chosen because the optimal emitter position is closer to the top surface, offering realistic implantation depths (70 nm) and efficient absorption in the SNSPDs. Moreover, a 60° etch angle supports single mode propagation for larger dimensions than in the case of 45° [52], resulting in a more fabrication friendly waveguide design. The width of the waveguide was set to 800 nm, as it supports the f-TE and f-TM modes only. The 1D PC was designed using the plane wave expansion (PWE) method [138], and the PC parameters were optimized to achieve complete bandgap for NV center emission wavelengths in 4H-SiC while maintaining nanofabrication-friendly dimensions [131].

6.1.3 SiC waveguide design with a PCM

In this section, we use the PC parameters from the PWE method and simulate a triangular cross-section waveguide with a reflector, using the Finite-Difference Time-Domain (FDTD) package in Lumerical [52, 99]. This allows for a comparison of the band gap position estimated from the two different methods, PWE and FDTD. The FDTD method uses the Fourier transform of the time-domain signal to record the field data in the frequency domain. To increase the collection efficiency of the photons from the ZPL and PSB of the NV center in SiC, the PC parameters were chosen to have a band gap spanning these emission wavelengths. As mentioned in Section 6.1.2, the size of the TM band gap (and thus the complete band gap) is significantly smaller than the size of the TE band gap, limiting the reflected wavelengths of both TE- and TM-like components of the NV center emission.

In this study, we focus on two sets of parameters for the PC 1) complete band gap and 2) NV optimized band gap, for a waveguide with $w = 800\,\text{nm}$ and $\alpha = 60°$. In the first scenario, the complete band gap was achieved using PC parameters of $r = 237\,\text{nm}$ and $a = 593\,\text{nm}$, with a complete band gap from 1268 nm to 1274 nm (TE band gap: 1268 nm to 1579 nm, TM band gap: 1249 nm to 1274 nm), which is outside the emission wavelength range of the NV center. In the second scenario, PC parameters of $r = 213\,\text{nm}$ and $a = 533\,\text{nm}$ were chosen, resulting in both TE (1200 nm to 1494 nm) and TM (1170 nm to

1192 nm) band gaps individually overlapping with the emission wavelength range of NV centers, but no complete band gap.

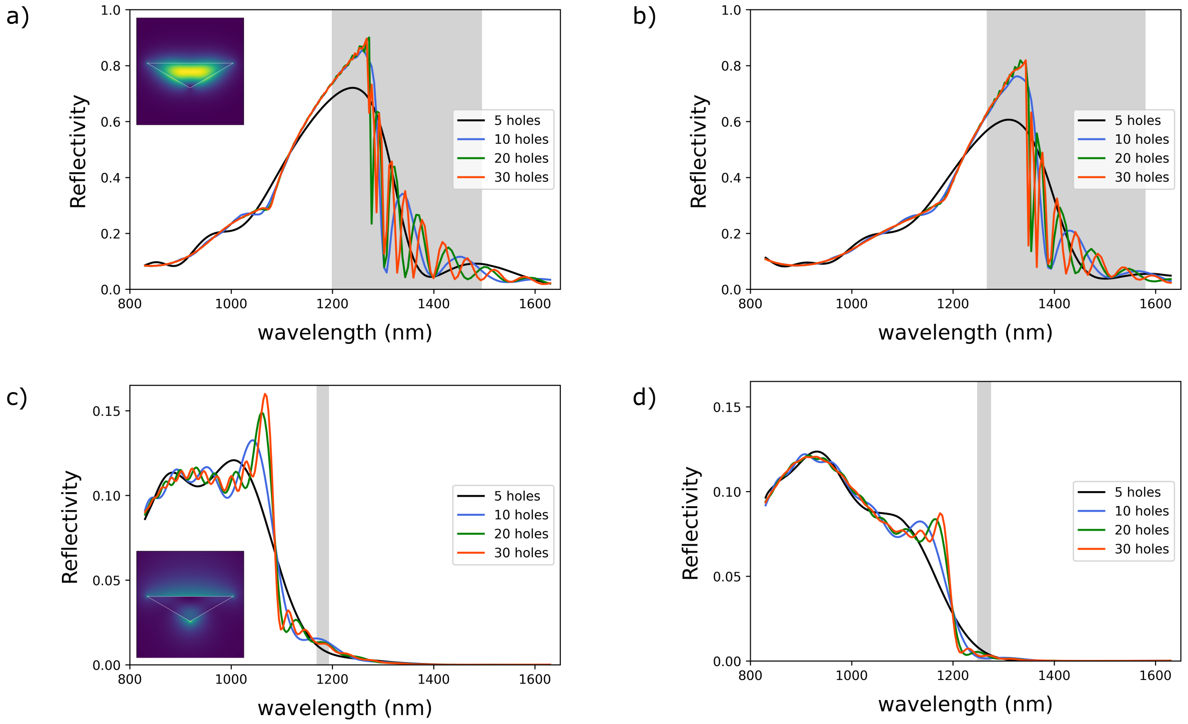

Figure 6.1: The reflectivity of photonic crystal mirror as a function of wavelength for varying number of air holes. Grey regions indicate the band gap values calculated from the PWE method. a) Reflectivity of the fundamental TE mode for a NV optimized design. Inset shows the mode profile of the fundamental TE mode of the waveguide at 1230 nm. b) Reflectivity of the fundamental TE mode for a complete band gap design. c) Reflectivity of the fundamental TM mode for a NV optimized design. Inset shows the mode profile of the fundamental TM mode of the waveguide at 1230 nm. d) Reflectivity of the fundamental TM mode for a complete band gap design.

As the number of air holes increases, the maximum reflectivity of the PCM increases and saturates for 20 air holes, as shown in Figure 6.1a-b. It is observed that the FDTD calculated wavelength for maximum reflectivity deviates from the center of the PWE calculated bandgap (grey region) [143]. The reflectivity curve has a full width half maximum of ∼200 nm, large enough to reflect the ZPL and the entire PSB of the color center emission. At 1230 nm, the NV optimized design has ∼85 % reflectivity for the f-TE mode. The reflectivity at a given wavelength depends on two factors: 1) the effective index of the f-TE mode (n_{eff}) and 2) the fraction of color center emission coupled into the waveguide. While n_{eff} decreases monotonically with an increased wavelength, the coupling efficiency rises to the optimal point (designed at 1230 nm) and subsequently decreases. The combination of the two effects cause the reflectivity to gradually increase for the short wavelengths and sharply drop for the long wavelengths. In the case of the f-TM modes, the reflectivity values are relatively lower due to the low coupling efficiency to the f-TM mode ($\sim$20 %) and evanescent loss to the surroundings ($n_{\text{eff}} = 1.09$).

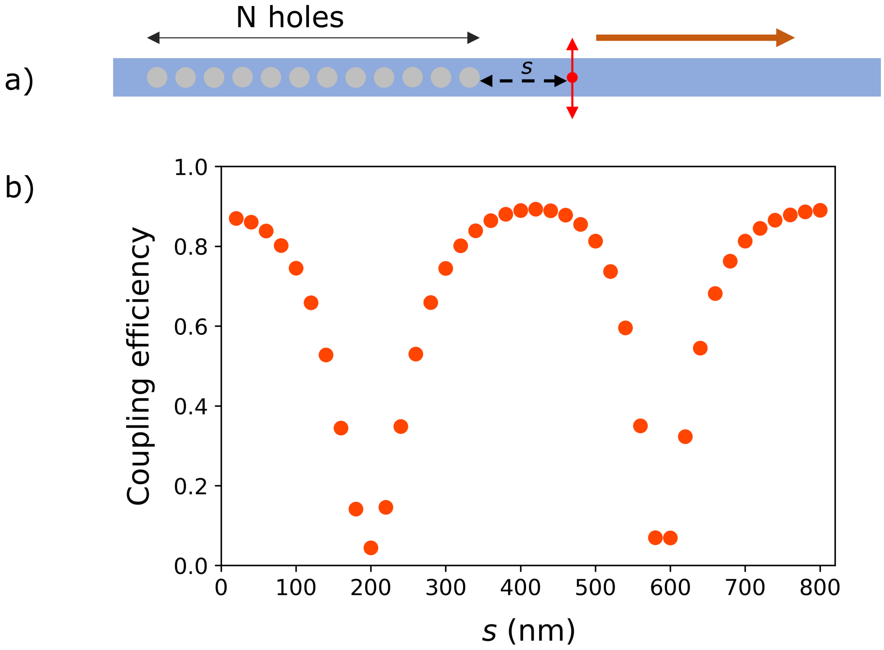

Figure 6.2: a) Top view of the waveguide design with reflector having N air holes. The color center (red dot with red arrows indicating the dipole orientation) is positioned at a distance s from the edge of the first hole and its emission propagation indicated by the arrow (brown). b) The variation of the coupling efficiency of the color center emission to the fundamental TE mode, in the direction of propagation, as a function of the color center's position (s) from the photonic crystal.

When a dipole emitter (1230 nm) is positioned at the centroid of the triangular cross-section ($\sim$70 nm depth) of the waveguide ($w = 800$ nm, $\alpha = 60^\circ$), 44 % of the 50 % light in each direction of the waveguide is coupled to the f-TE mode ($n_{\text{eff}} = 1.574$). In the presence of a PCM, the 50 % dipole emission directed toward the PCM is reflected back towards the emitter, causing interference with the emission propagating in the waveguide region (indicated by a brown arrow in Figure 6.2a). We observe that as the distance between the emitter and the PCM (s) is varied, the total light coupled to the f-TE mode varies periodically, as shown in Figure 6.2b. Constructive (destructive) interference occurs if the additional distance $2s$ traveled by the reflected wave results in a phase difference that is an even (odd) multiple of π. The periodicity of the coupling efficiency matches with the calculated value ($\lambda/n_{\text{eff}} = 390\,\text{nm}$) and the maximum coupling efficiency of 89 % is achieved for values of s that are integer multiples of ∼390 nm. There exists a 200 nm region with coupling efficiency >75 %. Thus, any randomly positioned emitter in the waveguide has at least 50 % chance of being at a position with high coupling efficiency.

6.2 Integrated SNSPDs for efficient detection of light in triangular waveguides

For single-photon detection, SNSPDs [144] provide unrivaled performance metrics such as high detection efficiency, including at 1550 nm wavelength [145], high count rate, low dark-count rate [146], and high temporal resolution [147]. As such, they have found many applications in quantum communication and information processing as well as in high energy physics for charged particle detection [148–150]. Compared to the top-illumination of meander SNSPDs and the enhancement of their detection efficiency by use of an optical cavity with a mirror underneath [151, 152], short waveguide integrated SNSPDs avoid coupling losses when being interfaced with on-chip devices and provide smaller recovery times as a result of their lower kinetic inductance [153, 154]. Due to their superior performance metrics, in this section we study the potential of integrating SNSPDs onto triangular cross-section SiC waveguides to detect single-photon emission from color centers embedded in the waveguide. The NbTiN thin films in this work were sputtered over 4H-SiC substrates and the optical and transport properties were measured by our collaborators [131].

6.2.1 Model of an integrated SNSPD with a triangular cross-section SiC waveguide

In this section, we look into the absorption efficiency of NbTiN based SNSPDs integrated on top of a triangular cross-section SiC waveguides based on the experimental measurements conducted on the NbTiN films [131]. This provides an upper limit for the achievable system detection efficiency of such an integrated detector. The absorption of color center emission (TE- or TM-like) for different configurations of NbTiN was modeled using the FDTD package in Lumerical software. The NbTiN was modeled using a complex permittivity model with (n, k) values obtained from the ellipsometry measurements of the NbTiN thin films on 4H-SiC [131]. The top and cross-section view of a single strip of NbTiN integrated on top of a triangular cross-section waveguide are shown in Figure 6.3a. The single strip has length l, width w, and thickness t, positioned at the center of the top surface of the waveguide.

When the width of the NbTiN strip ($l = 10\,\mu\text{m}$, $t = 6\,\text{nm}$) is increased, the absorption of the f-TE mode remains the same for widths greater than 100 nm and the absorption of the f-TM mode increases as the width increases, as shown in Figure 6.3b. It should be noted that the absorption of the NbTiN strip is sensitive to the polarization of the mode in the waveguide. The evanescent fields of the f-TE mode are concentrated around the center of the top surface (inset of Figure 6.1a), and therefore no changes in absorption are observed for larger SNSPD widths. In comparison, the evanescent fields of the f-TM mode are spread across the entire width of the waveguide (inset of Figure 6.1c), requiring larger widths of NbTiN for efficient absorption. As the length ($w = 100\,\text{nm}$, $t = 6\,\text{nm}$) and thickness ($w = 100\,\text{nm}$) of the NbTiN strip increases, the absorption of both the f-TE and f-TM mode increases, as shown in Figure 6.3c-d. Although larger thicknesses would result in better absorption, the single photon detection efficiency decreases [155], which is critical for applications in QIP.

Typical SNSPD based detectors have nanowires fabricated into a meander shape to increase the optical detection area. To this end, we modeled single loop and double loop

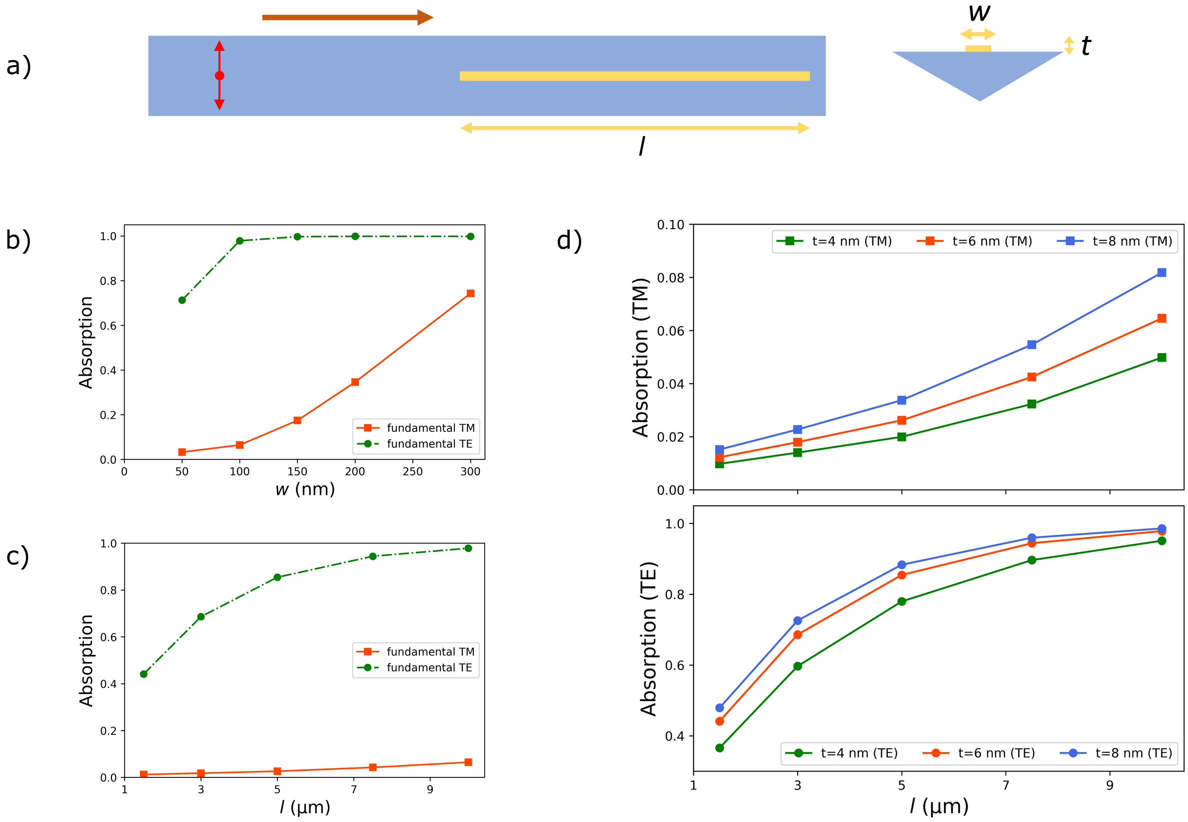

Figure 6.3: Simulated absorption of a single strip NbTiN layer. a) Top and cross-section view of a single strip NbTiN (yellow) with length l, width w and thickness t, integrated on a triangular cross-section SiC waveguide (blue). Red dot indicates the color center and red arrows denotes its dipole orientation. Absorption of the fundamental TE and fundamental TM modes of the triangular waveguide as a function of b) width ($l = 10\,\mu\text{m}$, $t = 6\,\text{nm}$). c) length ($w = 100\,\text{nm}$, $t = 6\,\text{nm}$). d) thickness ($w = 100\,\text{nm}$).

configurations of NbTiN integrated on top of a triangular cross-section SiC waveguides, as shown in Figures 6.4a, 6.4b, respectively. For a single loop NbTiN ($l = 10\,\mu\text{m}$, $w = 100\,\text{nm}$, $t = 6\,\text{nm}$), as the spacing between two adjacent arms d increases, the absorption of the f-TE mode remains constant and the absorption of the f-TM mode increases rapidly, as shown in Figure 6.4c. The absorption of the double loop NbTiN ($w = 100\,\text{nm}$, $d = 100\,\text{nm}$, $t = 6\,\text{nm}$) is higher than the single loop NbTiN, with a significant improvement in the absorption of the f-TM mode, as shown in Figure 6.4d. The polarization sensitivity of the double loop SNSPD at $l = 10\,\mu\text{m}$ almost disappears, thus having identical detection efficiencies for both f-TE and f-TM modes.

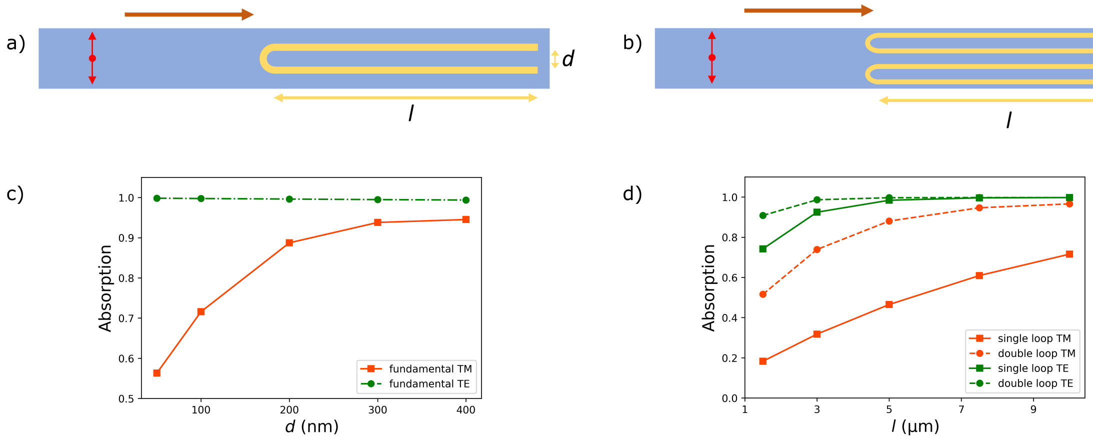

Figure 6.4: a) Top-view of a single loop NbTiN (yellow) with length l, spacing between adjacent arms d, on a triangular cross-section SiC waveguide (blue). b) Top-view of a double loop NbTiN (yellow) with length L, spacing between two adjacent arms d, on a triangular cross-section SiC waveguide (blue). Red dot indicates the color center and red arrows denotes its dipole orientation. c) Absorption of the fundamental TE and fundamental TM modes of the triangular waveguide as a function of spacing between adjacent arms, d ($l = 10\,\mu\mathrm{m}$, $w = 100\,\mathrm{nm}$, $t = 6\,\mathrm{nm}$). d) Comparison of absorption of fundamental TE and fundamental TM modes of the triangular waveguide as a function of length, for single loop and double loop NbTiN ($w = 100\,\mathrm{nm}$, $d = 100\,\mathrm{nm}$, $t = 6\,\mathrm{nm}$).

6.3 Discussion

The results presented in this paper demonstrate scalable approaches to efficiently collect and detect color center emission in triangular cross-section SiC devices for applications in QIP. Triangular cross-section devices are promising for chip scale integration of color center photonics. Moreover, these devices have a rich parameter space (etch angle, width) for optimal color center integration. At a given emission wavelength, there exists an optimal width for each triangular cross-section (with an etch angle alpha) such that the waveguide supports single mode propagation [52], which is important for applications in QIP. The polarization of the color center emission depends on the dipole orientation of the color center with respect to the c-axis. Using 4H-SiC grown along a-plane, most of the color center emission (silicon vacancy, divacancy, nitrogen vacancy) can be coupled into the f-TE mode.

Furthermore, the coupling of the color center emission can be improved by positioning the color center at the maximum intensity point of the f-TE mode, which is around the centroid of the triangular cross-section. Color centers are generated in SiC through implantation of high energy projectiles like electrons, protons, neutrons, ions. The implantation energy and the mass of the implanted particle determine the implantation damage done to the crystal, which can only be partially recovered through annealing [83]. Triangular cross-section devices can be designed depending on the implantation energies available, while still maintaining the single mode propagation and emitter's position at the centroid of the triangular cross-section. The waveguide simulated in this work ($w = 800\,\mathrm{nm}$, $\alpha = 60°$) has single mode propagation, with $\sim 44\,\%$ of the $50\,\%$ dipole emission (1230 nm) along one direction of the waveguide coupled to the f-TE mode.

The collection efficiency ($\sim 44\,\%$) on one end of the designed waveguide can be further improved using a photonic crystal mirror. The periodic variation of the dielectric constant (air holes) in a PC results in a photonic band gap for both TE- and TM-like modes in the waveguide. In a parallel work, a thorough photonic bandgap analysis using PWE method shows that the PCs can be used for a variety of applications and that their dimensions can be scaled depending on the color center emission wavelength [138]. In triangular cross-section PCMs, the TE bandgap is an order of magnitude larger than the TM bandgap, consequently a relatively much smaller complete bandgap. Therefore, a more effective approach for using the PCs as reflectors of c-axis oriented color center emission is to fabricate them in a-plane SiC substrates [52]. This would ensure that a large portion of any color center emission is coupled to the f-TE mode, reflecting frequencies spanning the ZPL and PSB of the color center emission. FDTD analysis shows that the position of the emitter relative to the PCM determines whether there is constructive/destructive interference in the waveguide region. We highlight that using the PCM proposed in this paper, a randomly positioned emitter has a higher collection efficiency compared to a symmetric waveguide ($\sim 44\,\%$) for $75\,\%$ of cases.

Efficient detection is another important factor for boosting the success rates of QIP protocols. SNSPDs offer a scalable approach for integrating detectors onto photonic devices. On-chip detection using SNSPDs can reduce optical losses, latency, and wiring complexity involved in off-chip detection [156]. As a basis for SiC waveguide integrated

SNSPDs, we investigated, for the first time, the optical and electrical properties of NbTiN thin films for SNSPD applications on 4H-SiC substrates. While the absorption of the NbTiN films is significantly higher on SiC than on SiO_2 substrates (up to 50 % for photons of 1680 nm), the magneto-electrical properties of the films, and thus presumably also of the detectors, are similar. Provided that the fabrication of SNSPDs on SiC waveguides is of similar quality as on SiO_2 substrates, we expect that they provide comparable electrical performance and simultaneously enhanced system detection efficiency due to higher absorption in the film, making SiC waveguide integrated SNSPDs a promising candidate for on-chip photon detection in QIP.

Chapter 7

Triangular Cross-Section Beam Splitters in Silicon Carbide

The existing QIP algorithms require error correction and heralded measurements to process information reliably and efficiently. Hence, one of the near-term goals is to build on-chip programmable photonic mesh networks to perform fault-tolerant QIP [157–159]. The successful implementation of such quantum mesh photonic hardware requires efficient single photon generation, manipulation, entanglement, and detection [115, 131, 160]. Beamsplitters (BS) play a crucial role in on-chip photonic QIP circuits for generating multiphoton correlation [158, 161] and can be used to realize several important operations like entanglement generation and single-photon interferometry (Hong-Ou-Mandel and Hanbury Brown-Twiss). Moreover, a universal quantum computer with linear optical quantum computing protocols has been proposed using BS, phase shifters, single photon sources, and photo-detectors [162]. Among the most studied forms of BS such as Y-branch, directional coupler (DC), and multi mode interferometer (MMI), DC is the most suited for on-chip QIP as it can function with single-mode waveguides [163]. In this work, we model low-loss beam splitters for the aforementioned quantum optical operations and test the experimental feasibility of the designs by fabricating triangular waveguides in an ion beam etching process to identify suitable designs for short-term implementation. These results are part of the publication titled "Triangular Cross-Section Beam Splitters in Silicon Carbide for Quantum Information Processing" [164].

7.1 Single mode triangular cross-section waveguide

Color center emission is dipole-like and such emission can couple to fundamental TE (f-TE), fundamental TM (f-TM) and other higher order modes that are supported in triangular cross-section waveguides [99]. It has been shown that for each etch angle there exists an optimal width for single mode (f-TE) propagation in triangular cross-section waveguides [29], which is a necessity for QIP applications [165]. So, to achieve high coupling efficiencies for color center emission, the color center should be positioned in a single mode waveguide at the maximum electric field (E-field) intensity point of the f-TE mode[29, 131], which is at the centroid of the triangle.

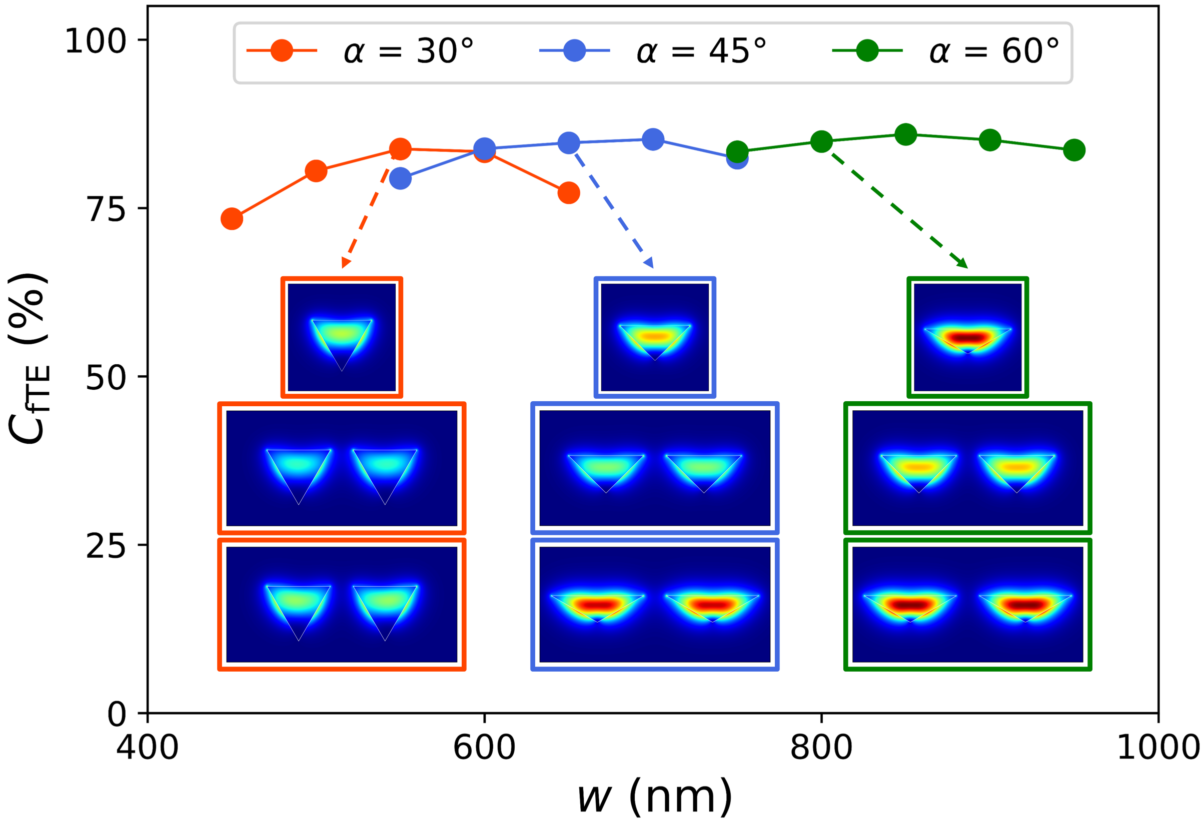

Figure 7.1: The coupling of a TE oriented dipole emission at the centroid of the triangular profile into the f-TE mode ((C_{fTE})) as a function of the waveguide width for three etch angles (α). Insets show electric field intensity profiles of the f-TE mode, TE supermode 1 and TE supermode 2 (top to bottom), at optimal waveguide widths supporting single mode propagation, for $\alpha = 30°, 45°, 60°$. The electric field intensity of the TE supermodes were plotted for adjacent identical waveguides with 200 nm gap between them.

We use FDTD package in Lumerical software to estimate the coupling efficiency of color center emission into the f-TE mode (C_{fTE}) for different widths (w) and etch angles (α) of a triangular cross-section waveguide (the angle at the apex of the triangle is 2α). We position the dipole emitter at the centroid of the triangle with an emission wavelength of 1230 nm. We find that for each α there exists a width with highest coupling ($> 80\%$) to the f-TE mode as shown in Figure 7.1. For our 50:50 BS simulations, we choose the optimal width values ($w = 550$ nm, 650 nm, 800 nm for $\alpha = 30°, 45°, 60°$ respectively) slightly lower than the widths with the highest C_{fTE}. The reason being that the waveguides with lower width have slightly higher evanescent fields (top panels of inset in Figure 7.1), necessary to create meaningful coupling between the adjacent waveguides in the BS, while only slightly reducing C_{fTE} ($< 1\%$).

The mode profile of the waveguide f-TE (f-TM) mode has a E-field intensity maximum closer to the top surface (apex) [99]. As the waveguide width decreases, the E-field intensity maximum of the f-TM mode moves closer to the apex and becomes evanascent (not supported in the waveguide). Using MODE package in Lumerical software, we find that at these optimal widths for $\alpha = 45°$ and $60°$, the waveguide supports only the f-TE mode. However, for $\alpha = 30°$, both f-TE and f-TM modes are supported in the waveguide at the optimal and smaller widths. The height of the triangle varies inversely with α and hence the widths needed for the f-TM to become evanescent are much smaller than the optimal width for $\alpha = 30°$.

In this paper, we design a 50:50 BS using two identical triangular cross-section waveguides with three regions: 1) input and output - where the waveguides are far apart with zero electromagnetic interaction, on either ends of the BS, 2) bent waveguide region, and 3) coupling region - where the waveguides are close enough to electromagnetically interact, as shown in Figure 7.2a. When light is injected into the f-TE mode of one of the waveguides on the input side (top left), it propagates through the straight and bent regions of that waveguide. When it reaches the coupling region, some of the light in the top waveguide is coupled into the bottom waveguide as it propagates along. Then the light in both the waveguides pass through the bent and straight regions to reach the output ports (through and drop ports). The proportion of light coupled into the bottom waveguide is determined by the coupling strength between the individual waveguide modes and the length of the waveguides in the coupling region.

When two identical waveguides are close to each other, the individual modes (f-TE) in each of the waveguides superimpose to form a supermode. The coupling between the two waveguides can be analyzed in terms of a pair of TE supermodes, as shown in the inset of Figure 7.1. For a BS with power P_0 in one of the waveguide at the beginning of the coupling region, the coupling length (L_C) required for a power P_2 to couple into the other waveguide is given by:

$$L_\mathrm{C} = \frac{\lambda_0}{\pi \Delta n_\mathrm{eff}} \sin^{-1}\sqrt{\frac{P_2}{P_0}} \tag{7.1}$$

where λ_0 is the free space wavelength, Δn_eff is the difference in effective refractive in-

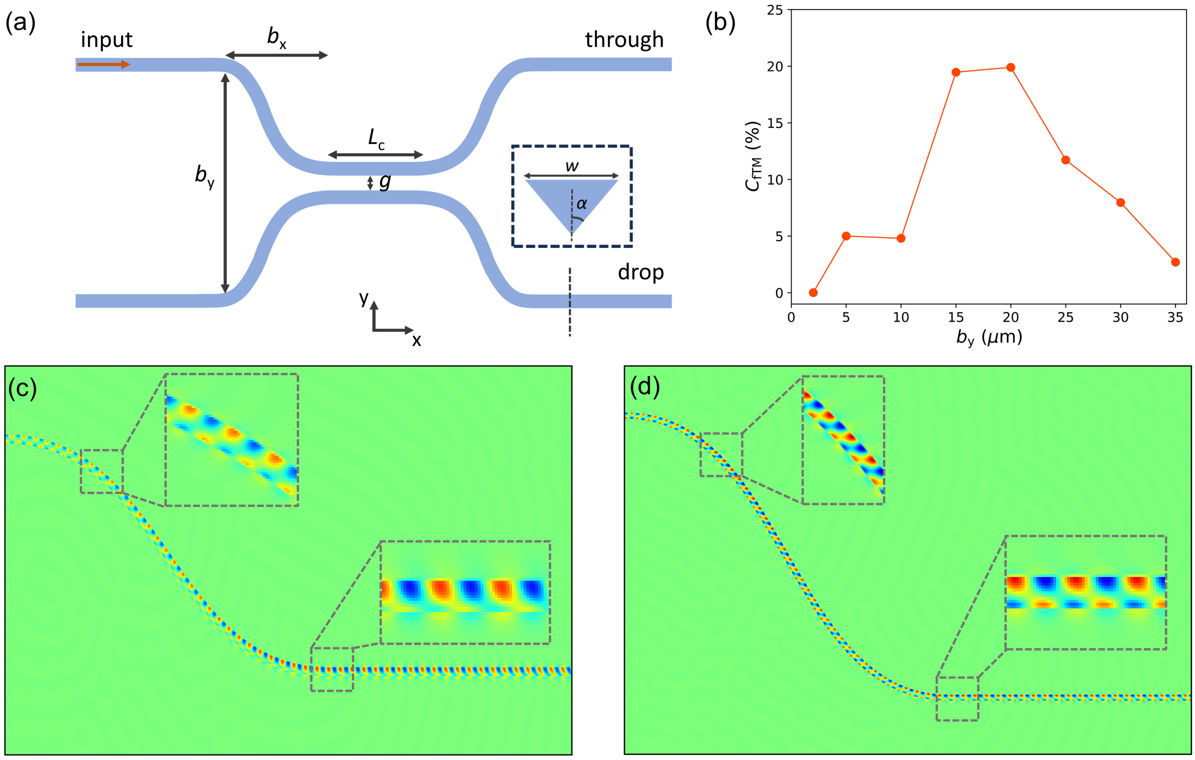

Figure 7.2: (a) Top view of the S-bend BS in 4H-SiC and the inset shows the triangular cross-section geometry. (b) The fraction of the f-TE input mode coupling to f-TM (C_fTM) mode along the bend with variations in bend y-span (b_y) for $\alpha = 30°$, $w = 550$ nm, and $L_\mathrm{C} = 30$ μm. (c)-(d) Propagation of E_z field in the xy plane of the structure described in (b) for b_y values of 20 μm and 35 μm, respectively.

dicies of the two TE supermodes [166]. The coupling length is inversely proportional to the coupling strength between the waveguides given by Δn_{eff}, which in turn depends on the confinement of the individual waveguide modes and gap between the individual waveguides in the coupling region. For a 50:50 BS, where there is 50% light in both the waveguides after the coupling region, the ratio P_2/P_0 equals 0.5. We use MODE package in Lumerical software to estimate the effective index of the two TE supermodes, for calculating the theoretical values of L_{C} for various BS geometries studied in the following section.

7.2 Integrated 4H-SiC beam splitter in triangular geometry

Recent advances in on-chip splitting mostly include rectangular or slab waveguides [163]. For performing QIP with integrated color centers in 4H-SiC, we construct the BS structure with symmetric triangular cross-section single mode S-bend waveguides with an overlap region to enable DC. Figure 7.2a shows the top view schematic of the BS with coupling length L_{C}, gap between the waveguides in the coupling region g, S-bend x-span b_{x}, S-bend y-span b_{y}, and the inset shows the triangular waveguide cross-section with w and α. In this paper, we investigate 50:50 BS in triangular cross-section waveguides with α = 30°, 45°, 60°, can be fabricated with the state-of-the-art processes, by varying the gap g between waveguides and consequently L_{C}.

In Lumerical FDTD simulations (mesh size = 30 nm), we choose 20 μm for b_{x} and 10 μm for b_{y}, where b_{x} corresponds to the terminal points and b_{y} corresponds to the curvature control points of the S-bend (Bézier curve), for $\alpha = 45°, 60°$. For $\alpha = 30°$, we need to account for potential higher-order mode conversion due to the bending curvature as the n_{eff}, one of the most important parameters for understanding mode propagation, of the f-TE and the f-TM modes are virtually the same in the waveguides with $\alpha = 30°$. Hence, the f-TE mode can transform into the f-TM due to identical n_{eff} and inter-mode coupling via bends [167]. Keeping $b_\mathrm{x} = 20$ μm constant, we vary b_y for modulating the bend curvature of the $\{\alpha, w, L_\mathrm{C}\} = \{30°, 550$ nm, 30 μm$\}$ BS structure.

To test the inter-mode coupling (cross-talk), we inject via the f-TE mode at the input port and collect via the f-TM mode at the through port of the BS. It is observed in Figure 7.2b that coupling to the f-TM mode (C_fTM) initially increases with the increase in b_y and after reaching a maximum value of $\sim 20\%$ for $b_\mathrm{y} = 20$ μm, C_fTM gradually decreases dropping down to 2.7% with $b_\mathrm{y} = 35$ μm. This trend occurs due to the expansion of the curved path with increasing b_y, however, after the inversion point, the bending becomes so gradual that the S-bend mimics a straight path. For a better understanding of the f-TE and f-TM mode coupling, we also study the E_z fields of the minimum and maximum C_fTM as E_z field is a good indicator of the existence of the TE and TM modes [138]. Figure 7.2c shows that at the starting point of the bending region with $b_\mathrm{y} = 20$ μm, E_z has a nodal plane in the triangular waveguide which corresponds to the f-TE mode and at the ending point, E_z field starts to develop in the waveguide, confirming the coupling to the f-TM mode. On the other hand, for b_y value of 35 μm, there is a constant E_z nodal plane indicating the f-TE mode throughout the S-bend, depicted in Figure 7.2d, which makes this bend structure suitable for maintaining the single mode propagation in the BS.

The above discussions lead us to the optimal selection of w and b_y of the 50:50 BS for each α. We choose 650 nm and 800 nm as w for $\alpha = 45°$, $60°$ respectively with $b_\mathrm{y} = 10$ μm in order to maximize the coupling and maintain single mode propagation for establishing a suitable environment for QIP with the triangular cross-section BS. For $\alpha = 30°$ waveguides, we pick $w = 550$ nm and $b_\mathrm{y} = 35$ μm to achieve similar outcomes. We vary the gap g from 50 nm to 400 nm for exploring a range of designs. Figure 7.3a shows that with increasing g, L_C shoots up rapidly for all three etch angles, experiencing minor losses ($< 1.5\%$) upon propagation through the entire BS. We observe another interesting phenomenon that L_C for the 50:50 BS with $\alpha = 60°$ is dramatically longer than the $\alpha = 30°$ and $\alpha = 45°$ BS for a particular g when $g \geq 200$ nm. As a result, owing to smaller footprints, $\alpha = 30°$ and $\alpha = 45°$ BS appear as better candidates than the $\alpha = 60°$ BS for

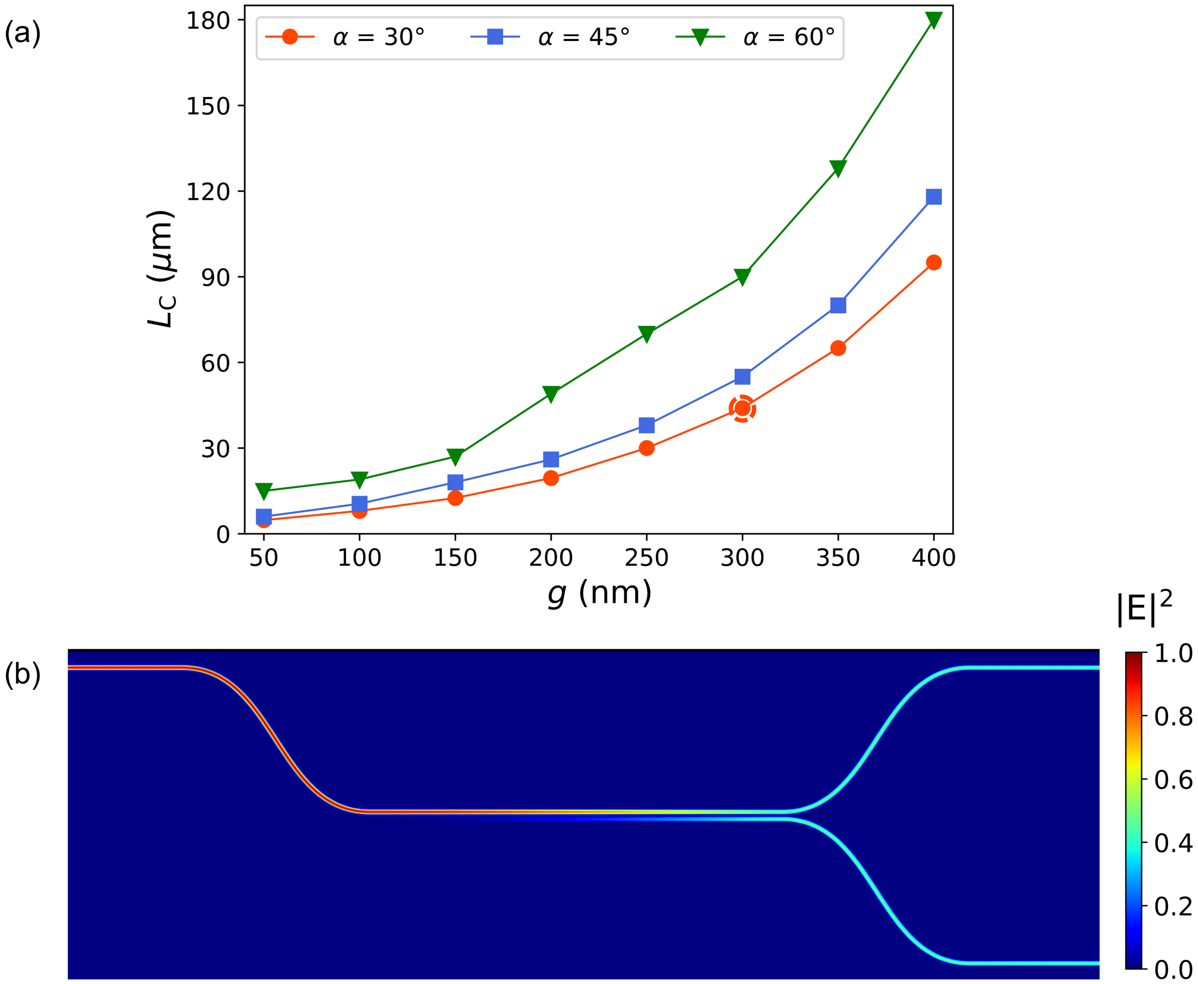

Figure 7.3: (a) L_C values for 50:50 splitting with an increasing gap g in $\alpha = 30°, 45°, 60°$ BS. (b) Top view of the E-field intensity profile for the integrated 50:50 BS SiC structure with $\{\alpha, w, b_x, b_y, g, L_C\} = \{30°, 550\text{ nm}, 20\ \mu\text{m}, 35\ \mu\text{m}, 300\text{ nm}, 44\ \mu\text{m}\}$ indicated by dashed circle in Figure 7.3a.

integrated quantum mesh photonic circuitry.

7.3 Fabrication of closely spaced triangular waveguides in 4H-SiC

Triangular cross-section photonics has previously been fabricated in SiC through Faraday cage assisted etching method [29, 43, 44] suitable for chip-scale integration of color centers with no degradation in color-center properties compared to bulk substrate[29]. This approach could be brought to wafer-scale using the ion beam etching [46]. Therefore, we test a new ion beam etching process to fabricate triangular cross-section waveguides in 4H-SiC, with varying gaps between waveguides (100 nm, 200 nm, 300 nm, 500 nm). This provides an insight into what spacing between the waveguides in the coupling region of the simulated 50:50 BS are fabrication friendly, using the ion beam etch process.

We use electron beam lithography to define the patterns on 4H-SiC substrates and then the pattern is transferred to a 120 nm thick nickel hard mask deposited using an electron beam evaporation, through a lift-off process. Triangular cross-section waveguides are then fabricated by ion beam etch using SF_6 and O_2 chemistry. We use focused ion beam (FIB) - scanning electron microscope (SEM) to confirm the triangular cross-section of the fabricated waveguides, as shown in the inset of Figure 7.4d. We measure the etch angle (α) of these waveguides to be 30°. For adjacent waveguides with gaps of 100 nm and 200 nm, we observe no substantial etch in the region between the waveguides, as shown in Figure 7.4a-b. For waveguide gaps $\geq$ 300 nm (300 nm, 500 nm), the fabricated waveguides have triangular cross-sections, as shown in Figure 7.4c-d. The lack of etching in the region between the waveguides for smaller waveguide gaps may be due to the inability of the ions which are incident at an angle on the substrate, to reach well below the surface level of the substrate, and also reduced etching caused by mass-transport issues in those closely spaced regions.

7.4 Discussion

The modeling results presented in this paper offer an approach to build low-loss triangular cross-section 50:50 BS in 4H-SiC necessary to perform key quantum interferometry operations for QIP applications. Here, triangular cross-section photonics provide a scalable route to integrate color centers into quantum photonic devices and circuits. Moreover, high-performance triangular cross-section photonic structures in 4H-SiC like waveguides, waveguides with integrated SNSPDs, photonic crystal mirrors, and photonic crystal cavities that facilitate efficient generation, collection and detection of single photon emission from color centers, necessary for applications in QIP have been demonstrated [29, 99,

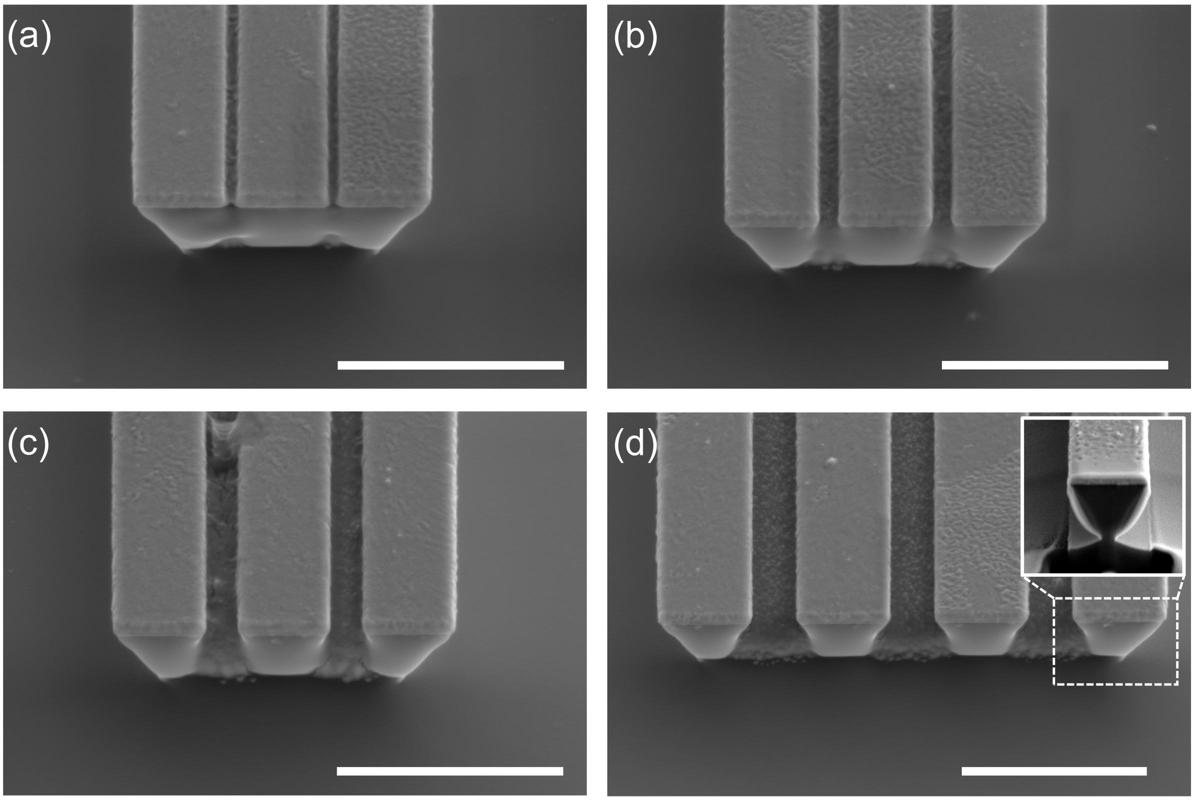

Figure 7.4: The SEM images of ion beam etched waveguides in 4H-SiC. (a)-(c) 800 nm wide waveguides with gaps of 100 nm, 200 nm and 300 nm respectively. (d) 1000 nm wide waveguides with a gap of 500 nm. Inset shows a FIB-SEM of the fabricated 1000 nm waveguide with a triangular cross-section. The scale bar is 2 μm.

131, 138]. Thereby, NV center in 4H-SiC with emission wavelengths near the telecommunications range is most suited for building large-scale quantum communication networks.

Our initial fabrication tests show that triangular cross-section waveguides with gaps greater than 300 nm can be fabricated using the wafer-scale ion beam etch process. From the simulations, we note that for a waveguide gap $g \geq 300$ nm in the coupling region, $\alpha = 30°$ and $45°$, offer 50:50 BS with fabricatable footprints (e.g. coupling region $L_C \leq 50$ μm), for applications in QIP. Here, supporting structures for waveguide suspension would need to be designed. The ion beam etch process conditions could be further optimized to achieve triangular cross-section waveguides with waveguide gap $\leq$ 300 nm, by choosing process conditions that result in a predominantly chemical etch. Under such etch conditions, the byproducts of the etch are volatile gases (SiF_4, CO, CO_2), preventing re-deposition, allowing the etch to continue. When there is a reasonable physical etch component, the sputtered material has a higher chance of re-deposition, especially when the gap between the waveguides is small, resulting in a slower etch or sometimes no etch. Another alternative could be choosing a steeper etch angle, because such waveguides would not require a deep etch to release the structure.

Triangular cross-section photonics in 4H-SiC provides an avenue to achieve efficient chip- and wafer-scale integration of color centers, with very little degradation of color center properties compared to bulk, essential for applications in QIP. Our simulation results demonstrate that 50:50 BS necessary for applications in QIP can be implemented using triangular geometry and our initial etch tests show that ion beam etching is suitable for achieving this.

Chapter 8

Nanopillars with Integrated NV Centers in 4H-SiC

Color centers in bulk emit light in all directions, resulting in significant losses when photons are collected via an objective lens. For the purposes of quantum information processing, increasing the number of collected photons would impact the success rate of entanglement distribution, and the sensitivity of the spin-qubit readout and magnetic sensing. Passive photonic devices, such as nanopillars direct color center emission via total internal reflection, resulting in higher photon collection efficiencies [60]. In this chapter, we model the collection efficiencies of the emission from nitrogen vacancy (NV) color centers in 4H-SiC integrated into nanopillars. Next, we fabricate nanopillars with integrated NV centers and perform photoluminescence and lifetime measurements of the nanopillar-integrated NV centers. These results are part of the publication titled "ICE-CAP: a 3-in-1 integrated cryogenic system for emission, collection and photon-detection from near infrared quantum nanophotonic devices" [98].

8.1 Collection efficiencies of nanopillars

We use the finite-difference time-domain (FDTD) package in Ansys Lumerical to simulate waveguiding properties of SiC nanopillars at the emission wavelengths of the nitrogen vacancy (NV) color center in 4H-SiC. Nanopillars with a height of 1 μm and diameters varying from 300-1100 nm were simulated, with a dipole emitter positioned at the lateral and longitudinal center of the nanopillar. We observe that the nanopillar guides the dipole emission towards the top of the nanopillar as shown in Figure 8.1. We calculated the light collection efficiency of the color center emission for an objective with numerical aperture of 0.85, positioned above the nanopillar. Collection efficiencies for a horizontally and vertically oriented dipole were simulated and these values were used to calculate the coupling efficiencies for the dipole oriented at an angle 71° to the vertical axis. The vertical (*hh, kk*) and 71° to the vertical axis (*hk, kh*) orientations of the dipole represent the configurations of the NV center in 4H-SiC. The light collection efficiency varies as a function of nanopillar diameter and the dipole source orientation inside the nanopillar, as shown in Figure 8.2. We find that the nanopillars boost the light collection efficiencies by at least an order of magnitude compared to values for a color center at the same depth (500 nm below the surface) in the bulk.

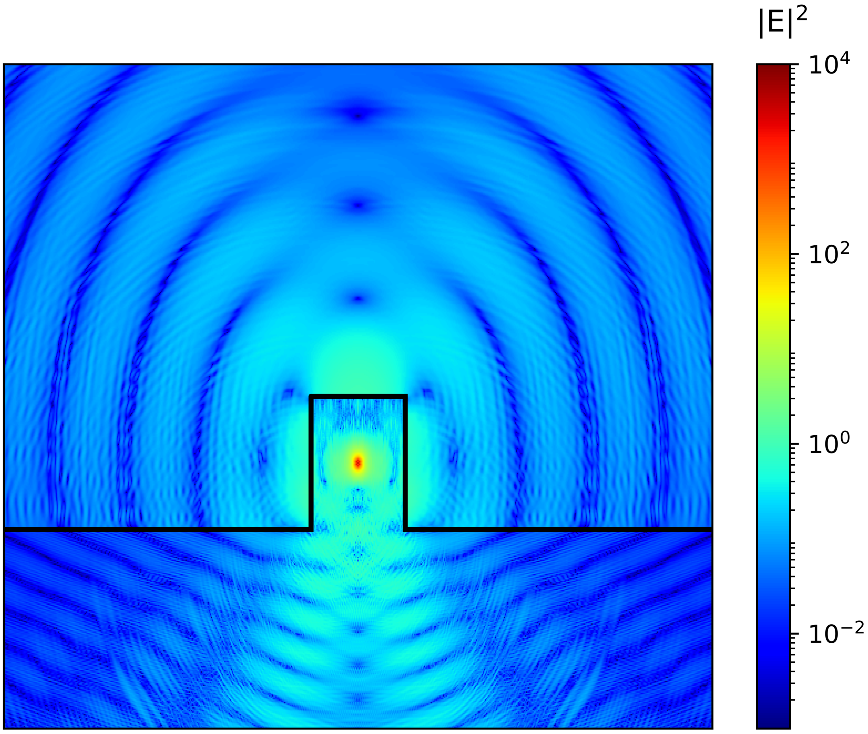

Figure 8.1: Simulated electric field intensity profile of a vertically oriented electric dipole emission positioned at the center of a 850 nm diameter nanopillar.

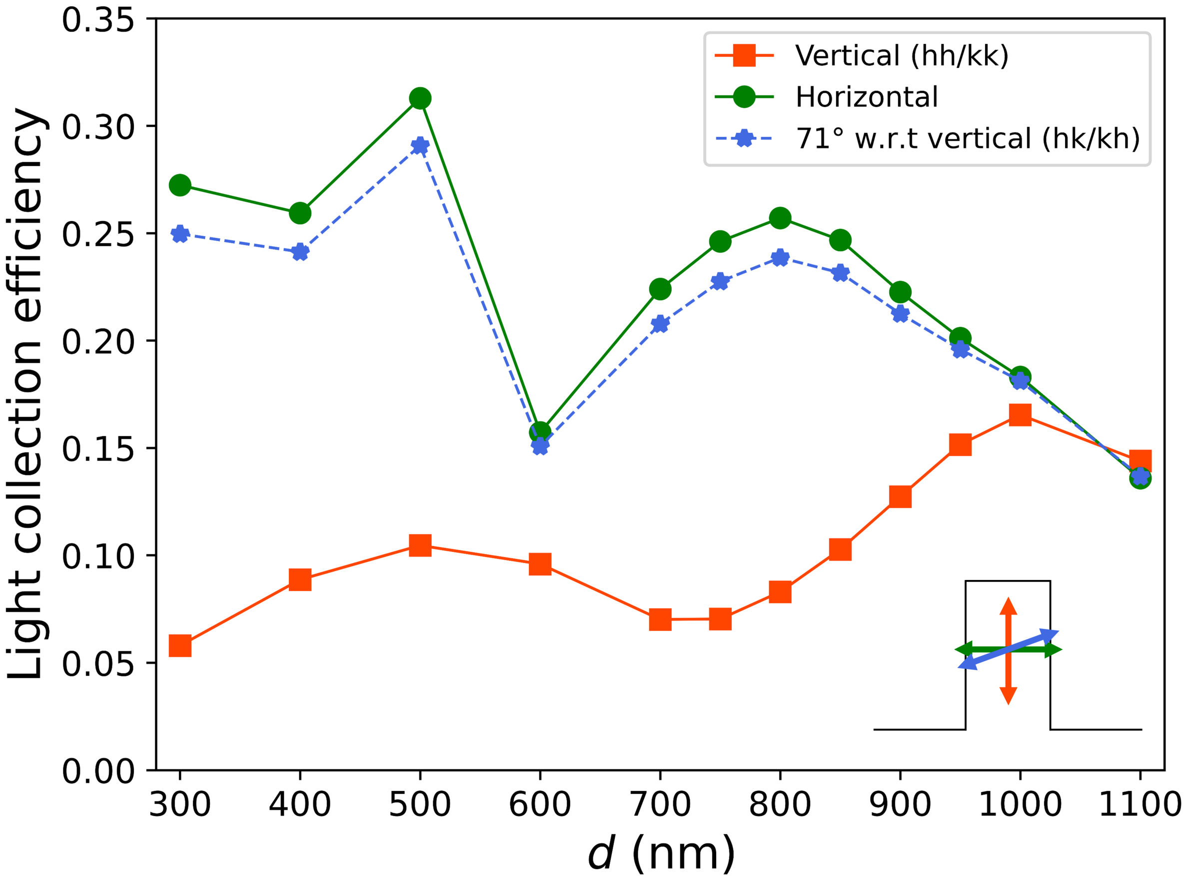

Figure 8.2: Simulated values of light collection efficiency as a function of the nanopillar diameter, for different orientations of the NV dipole inside the nanopillar (inset).

8.2 Nanopillar fabrication

The 4H-SiC samples were first commercially implanted (CuttingEdge Ions, LLC) with $^{14}N^{+}$ ions at an energy of 375 keV and a dose of 1×10^{14} cm^{-2} [33], to generate a peak nitrogen concentration at a depth of 500 nm, as calculated by stopping and range of ions in matter (SRIM) simulations. The implants were then activated by annealing the samples in a 1-inch Lindberg Blue tube furnace at 1050 °C in nitrogen atmosphere for 60 minutes [33]. We then patterned arrays of circular holes in a 350 nm PMMA layer, with diameters ranging from 300-1100 nm, using e-beam lithography. A 5 nm titanium adhesion layer followed by a 50 nm nickel hard mask layer were then e-beam evaporated and lifted off to transfer the circular patterns to this metal layer. Nanopillars were etched into SiC through an inductively coupled plasma reactive ion etching (ICP-

RIE) in a Oxford PlasmaLab 150 Inductively Coupled Etcher Fluorine, involving SF_6 and O_2 chemistry [60]. The ICP-RIE parameters described in Chapter 3 were used to achieve an etch rate of ~300 nm/min and a pillar height of 1 μm. Finally, the metal layer was removed by etching the samples in Transene's nickel and titanium etchants. Scanning electron microscope (SEM) images of the fabricated nanopillars are shown in Figure 8.3a-b.

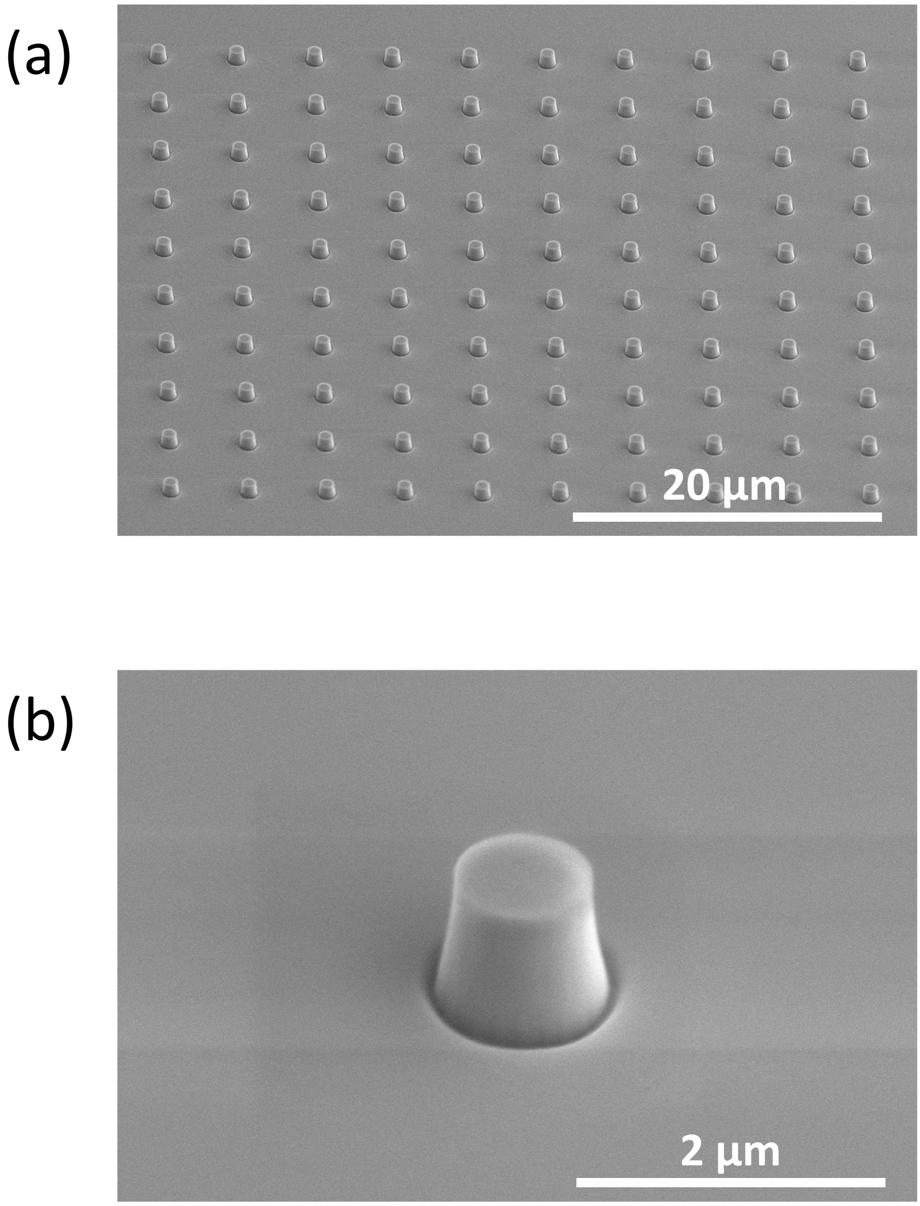

Figure 8.3: a) SEM image of an array of 850 nm diameter SiC nanopillars (scale bar = 20 μm), b) SEM image of a single 850 nm diameter SiC nanopillar (scale bar = 2 μm).

8.3 Optical Measurements

To characterize the NV centers in the fabricated nanopillars, we performed photoluminescence (PL) measurements in the ICECAP system [98]. First, we confirmed the presence of color centers in the sample by taking the PL spectrum of both the divacancy and the NV center regions. These color center species have four ZPLs due to four possible nonequivalent lattice sites for the defect complexes associated with each species. Figure 8.4a has the results of one such measurement performed at 1.56 K with a pump laser of 785 nm; the ZPLs of both species of color center agree with the literature values [19, 20, 53, 168]. For the rest of the measurements, we use an 1150 nm longpass filter to remove the divacancy signal.

As a test of the SNSPDs, we focused on an area of the chip that has both fabricated nanopillars and an unetched area, and performed a 2D photoluminescence scan across it. We show that not only are the single-photon detectors detecting signal to the PL scan, but also that there appears to be enhanced collection from the pillars compared to the unetched bulk, as expected from the simulations reported in Section 8.2. The completely etched area in between these two regions of interest shows no light collection because the etching depth is greater than the color center implantation depth, so any NV centers that were present have been etched away. The results of this scan are shown in Figure 8.4b.

We also measured the lifetime of the NV centers in the 600 nm diameter nanopillars at a series of low temperatures; plots of these measurements are shown in Figure 8.4c. Each decay was fit to a biexponential function $A_1 \exp(-t/\tau_1) + A_2 \exp(-t/\tau_2)$, where A_1, A_2, and τ_1 are fitting parameters and $\tau_2 \approx 0.54$ ns is fixed as the decay rate of the pump laser pulse, which was measured separately. This is necessary because back-reflections of pump light off the surface of the sample are simultaneous with color center emission. This back-reflection is significantly attenuated by a 1150 nm longpass filter prior to detection, but is still present in the data due to its vastly greater initial brightness relative to the NV center emission. We find a lifetime $\tau = (2.2 \pm 0.4)$ ns across the temperature range 1.56-2.5 K. This agrees with previously reported values of NV center lifetimes of (2.1 ± 0.1)

ns [33] and 2.21 ns [34]. The first value was extracted PL lifetime measurement at room temperature and 10 K in an ensemble bulk sample. The second value was extracted from a $g^{(2)}(0)$ measurement of a single NV center at 10 K [34]. Previous measurements of NV center lifetimes under different excitation powers may provide insight into the slight variation of lifetimes vs. temperature reported in this work [33]; as such, additional laser stabilizing techniques may resolve this discrepancy.

To check if the enhanced collection mentioned above includes photons emitted from NV centers, a comparison of measured NV center ZPL amplitudes extracted from the PL spectra from the 600 nm pillars and from the bulk area of a second chip of 4H-SiC that underwent a similar nitrogen implantation process (targeted at 80 nm depth) and annealing parameters as the nanopillar chip. Each ZPL peak was fit to a Lorentzian. The percent increase in amplitudes for each ZPL were 17±3% for the *kh* peak, 22±3% for *hh*, 63±5% for *kk*, and 0.2±10% for the *hk* peak, confirming statistically significant enhanced collection for all ZPLs but that of the *hk* orientation. This is without accounting for the fact that the number of emitters in the excited ensemble in the nanopillar is several-fold smaller than in the bulk due to the laser spot size being larger than the pillar cross-section. Another important conclusion drawn from the PL spectra comparison study is that no ZPL broadening was observed, as the widths of each of the Lorentzians calculated from the nanopillar PL spectrum were no greater than those calculated from the bulk PL spectrum. Therefore, even if the fabrication methods do induce small amounts of strain into the surrounding bulk material, NV centers are robust to it, which is encouraging news in terms of the development of integrated nanophotonic systems for these telecom-emitting color centers.

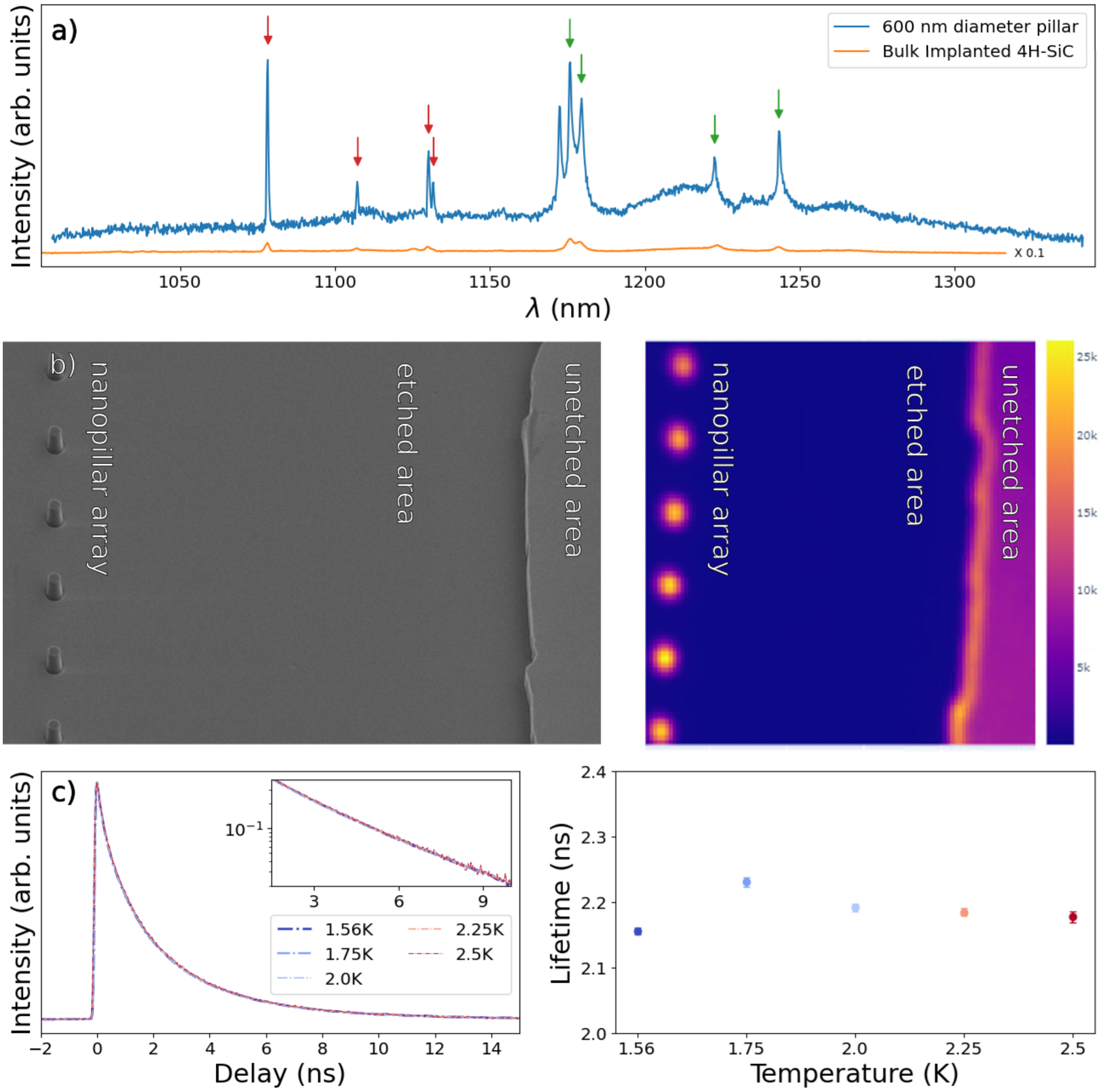

Figure 8.4: Measurements performed at cryogenic temperatures (1.56 - 2.5 K) with a 785 nm laser at 5 mW power. a) Photoluminescence spectrum of a 4H-SiC chip with integrated color centers. Divacancy (VV^0) ZPLs (1070 - 1130 nm) are marked with red arrows. NV center ZPLs (1170 - 1245 nm) are marked with green arrows. b) Left: SEM image of a section on the chip with both fabricated nanopillar structures and an unetched area. Right: 2D PL scan of same section. Color bar signifies photon detection counts. c) NV center ensemble lifetime measurements for a range of temperatures and the extracted lifetime values from an exponential fit. Error bars are one standard deviation of the fit. Inset: log-linear plots of each lifetime measurement.

Chapter 9

Wafer-Scale Nanofabrication of Triangular Photonics in 4H-SiC

The most desirable color centers, in terms of optical stability and homogeneity of quantum emitters, are found in bulk substrates. However, this poses fabrication challenges due to a lack of an undercutting layer necessary to create suspended devices such as micro- and nano-resonators. A leading approach to creating suspended devices in bulk substrates involves angle-etching methods which produce triangular cross-section devices [169]. FDTD modeling, as discussed in the previous chapters, has shown that this geometry supports single-mode waveguide propagation, high-quality factor optical resonators, photonic band gap formation, and highly efficient integration with superconducting nanowire single photon detectors. Chip-scale experiments based on Faraday cage angle-etching have shown that optical and spin properties of color centers in silicon carbide remain intact upon integration with triangular waveguides [29]. Bringing this process to wafer-scale requires a change in approach. In this chapter, we demonstrate a wafer-scale nanofabrication process applied to an arbitrary SiC substrate. The key innovation is the development of an angle-etch process in an Ion Beam Etching tool, which produces suspended nanodevices with triangular cross-sections.

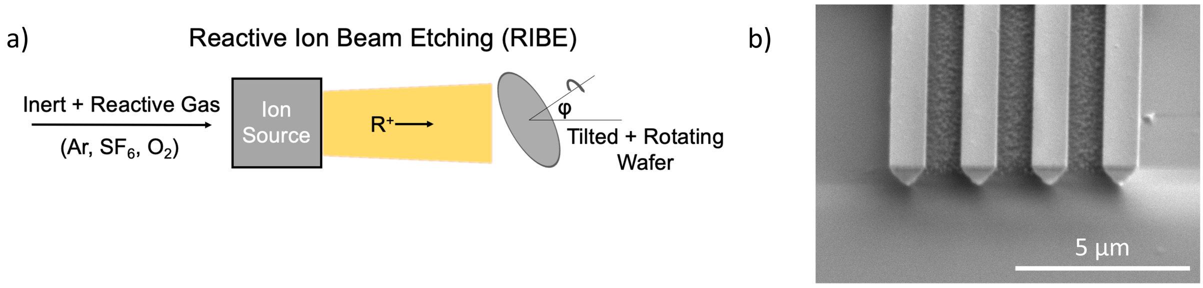

Figure 9.1: a) The schematics of the key Reactive Ion Beam Etching (RIBE) nanofabrication step for wafer-scale SiC angle-etch. b) SEM image of an array of closely spaced, identical triangular cross-section waveguides fabricated using RIBE process.

9.1 Wafer-scale reactive ion beam etching process in silicon carbide

The key fabrication step in angle-etching silicon carbide at scale is the Reactive Ion Beam Etching (RIBE) process with a rotating tilted wafer. As illustrated in Figure 9.1a, this method accelerates Ar ions for the physical etch and reactive species, such as SF_6 and O_2, for the chemical etch. The tilt of the wafer defines the etch angle, and its rotation assures all sides are uniformly etched through, providing a device undercut. This process can be done directly after the Ni mask lift-off or can be preceded by a high-selectivity (>100:1) top-down etch in an inductively-coupled plasma reactive ion etcher, resulting in a deeper overall undercut.

The process begins by patterning the photonic structures in a 350 nm PMMA resist layer using e-beam lithography. A 5 nm titanium adhesion layer followed by a 120 nm nickel hard mask layer were then e-beam evaporated and lifted off to transfer the circular patterns to this metal layer. The SiC chips with Ni patterns are then etched using RIBE in Intlvac Nanoquest II. The optimized RIBE process parameters are: beam voltage = 300 V, accelerating voltage = 120 V, beam current = 110 mA, RF power = 150 W, $Ar/SF_6/O_2$ flow rates = 10/10/2.5 sccm, etch time = 2 etch cycles of 35 minutes each with 2 minutes cooling time between the two etch cycles. The etch process produced identical triangular cross-section waveguides on a 5 mm x 5 mm SiC chip, as shown in

Figure 9.1b.

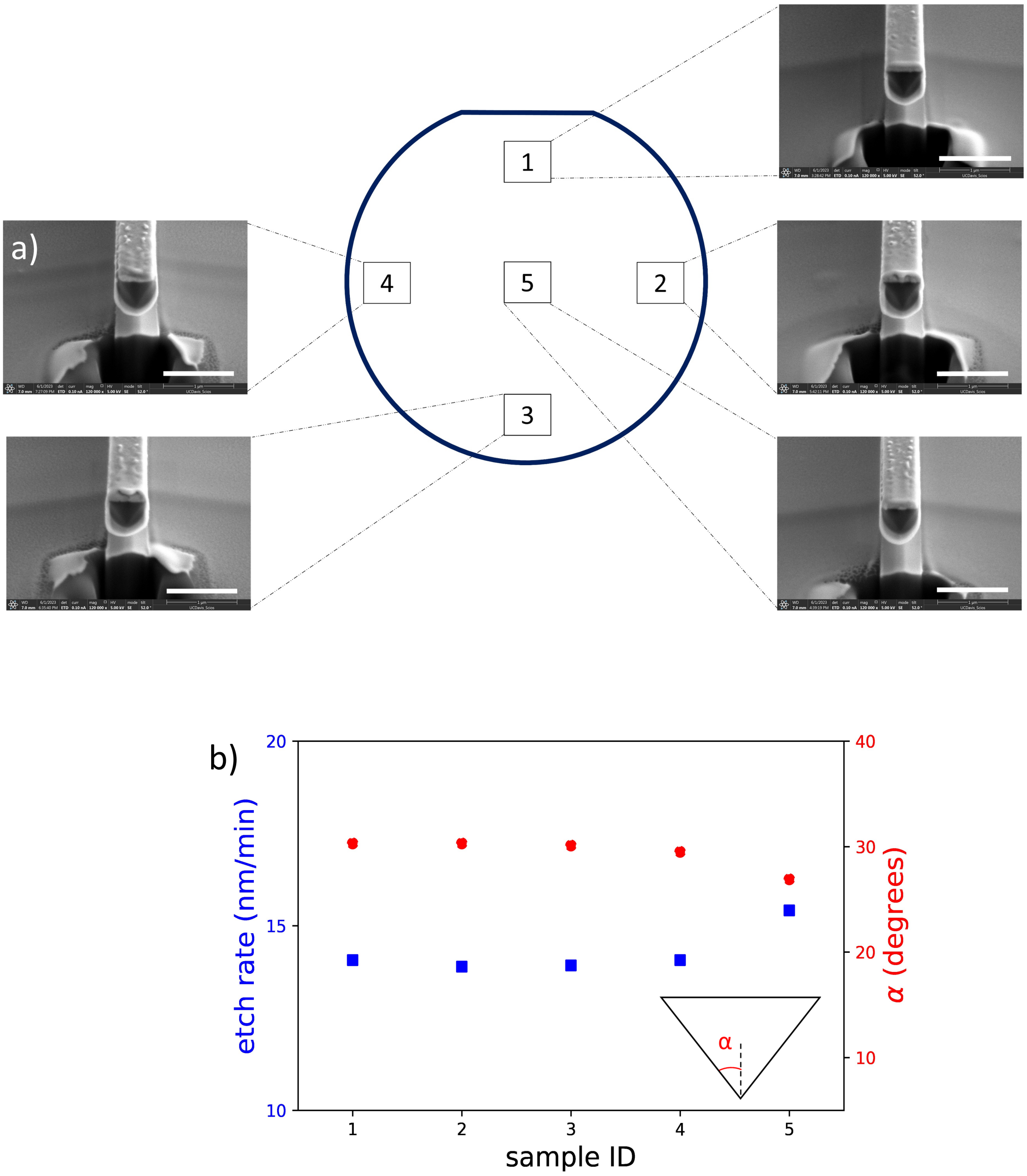

Figure 9.2: a) The profiles of fabricated devices from different numbered sections on the wafer. b) The achieved etch rate and etch angle (α) uniformity across different parts of the wafer, showing 4% and 4.4% variability, respectively.

To test the wafer scalability of this process, five silicon carbide dies were placed across a 6-inch silicon carrier wafer, at locations that mimic the center and circumference of a 4-inch wafer, as shown in Figure 9.2a. The RIBE process generated a uniform profile of 500-1000 nm in width, with a triangular device cross-section, an etch angle (α) of $(29.4 \pm 1.3)^\circ$, an etch rate of (14.3 ± 0.6) nm/min, and an etch selectivity of 8:1, as shown in Figure 9.2b. The etch angle scales linearly with the tilt angle of the substrate holder, as shown in Figure 9.3. Figure 9.4 displays a variety of active and passive photonic devices in 4H-SiC fabricated using this process. We measured the photoluminescence spectrum from the fabricated triangular cross-section photonic devices with integrated color centers, as shown in Figure 9.5. The spectrum includes ZPLs from both implanted NV centers and naturally occurring divacancy centers.

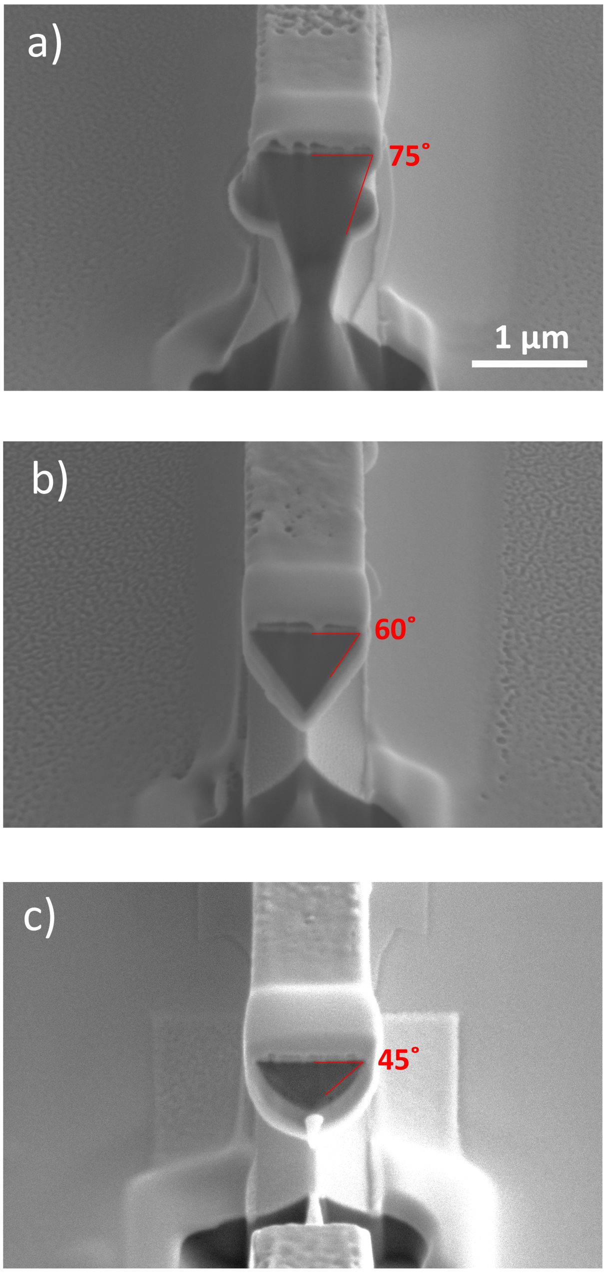

Figure 9.3: The profiles of a 1μm waveguide fabricated with the same RIBE process at substrate tilt angles of a) 30°, b) 45°, and c) 60°.

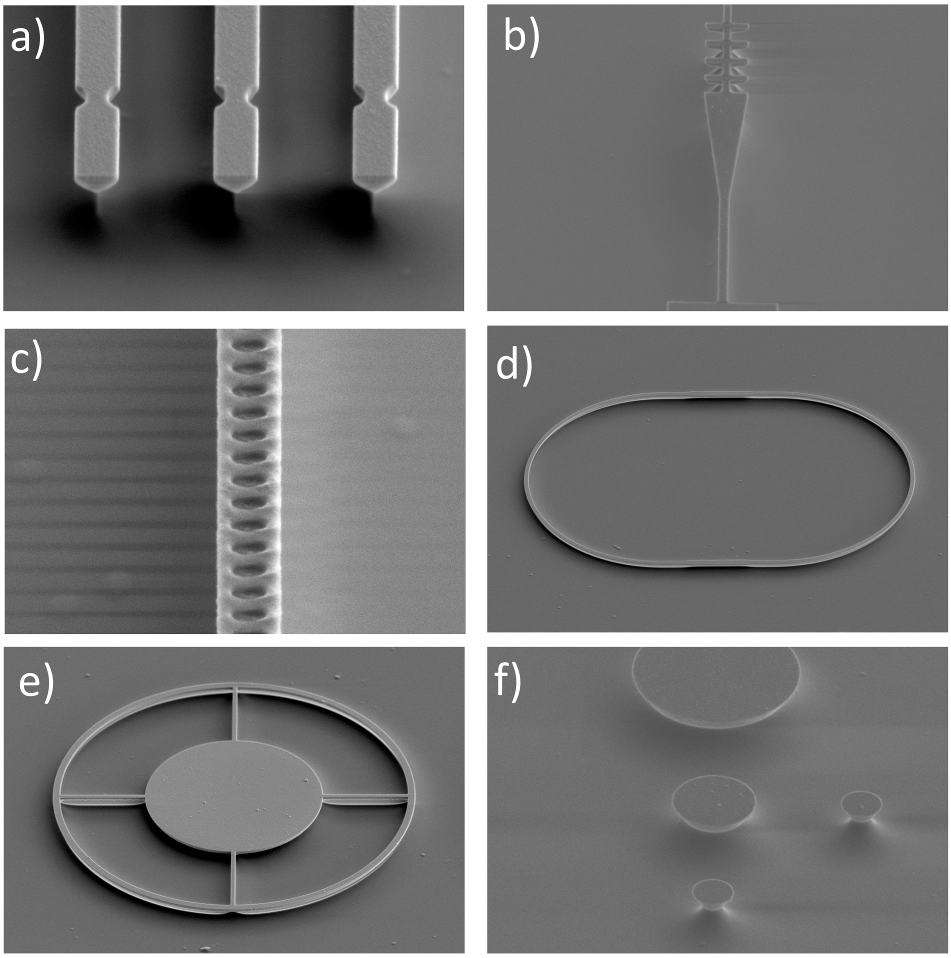

Figure 9.4: SEM images of nanofabricated SiC devices in the wafer-scale angle-etch RIBE process: a) waveguides with notch couplers, b) fish-bone grating coupler, c) photonic crystal cavity, d) racetrack resonator, e) microring resonator, and f) microdisk resonator.

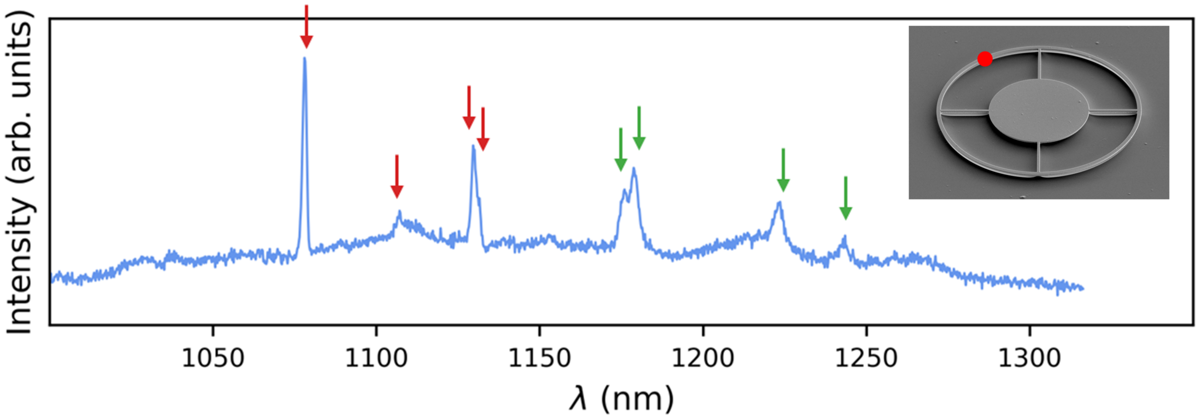

Figure 9.5: Photoluminescence spectrum of an angle-etched 4H-SiC ring resonator with integrated color centers at 7 K. Divacancy (VV^0) ZPLs (1070 - 1130 nm) are marked with red arrows. NV center ZPLs (1170 - 1245 nm) are marked with green arrows. (Inset) SEM image of the triangular cross-section ring resonator fabricated using the optimized RIBE process, red dot indicating the spot from which photoluminescence was measured.

9.2 Discussion

To our knowledge, this is the first demonstrated wafer-scale angle-etch process on an arbitrary SiC substrate with integrated color centers, which is key to the integration of well defined quantum emitters with photonic devices. Most importantly, the color center spectral properties are preserved upon integration into triangular cross-section devices fabricated using the wafer-scale RIBE process developed in this study. The versatility of the approach lends itself to a variety of patterning techniques (e-beam, photolithography), up to 6-inch commercially available wafers, natural, pre-implanted as well as isotopically purified SiC substrates, thus supporting long-lived spin qubits with uniform optical interface. We believe this method has a potential to produce key quantum photonic devices for quantum communication, computation and sensing, thereby advancing the complexity of quantum circuit produced in a substrate.

Chapter 10

Outlook

Triangular photonics holds promise for large-scale implementations of quantum information processing technologies. The modeling results in the previous chapters of this dissertation highlighted that triangular photonics promote efficient emission, collection, and detection of the single photons emitted by color centers in SiC, while preserving the spin-optical properties of the color centers [29], making them front-runner for scalable nanophotonic integration of color centers. Coupled with the demonstration of wafer-scale etch process using ion beam etching to produce triangular photonics in bulk SiC, and a suitable SNSPD material (NbTiN), opens up the possibility of fabricating an on-chip quantum quantum photonic circuits, such as, on-chip Hong-Ou-Mandel (HOM) interferometer and waveguide-integrated SNSPDs for on-chip single-photon detection, as shown in Figure 10.1.

Triangular cross-section photonics in 4H-SiC, fabricated through wafer-scale ion beam etch process with integrated color centers, can be used to demonstrate key experiments in QIP (quantum repeaters), such as high generation rate for single photons, heralded entanglement purification, very high-fidelity initialization, single-shot readout and entangling gates, and qubit registers, shown using color center-integrated triangular photonics in diamond. The single-photon emission and collection efficiencies, which determine the success rate of the aforementioned experiments, would certainly benefit from optimal and deterministic generation of color centers within these photonic structures. Controllable defect generation methods such as focused ion beam [84], laser writing [85, 86],

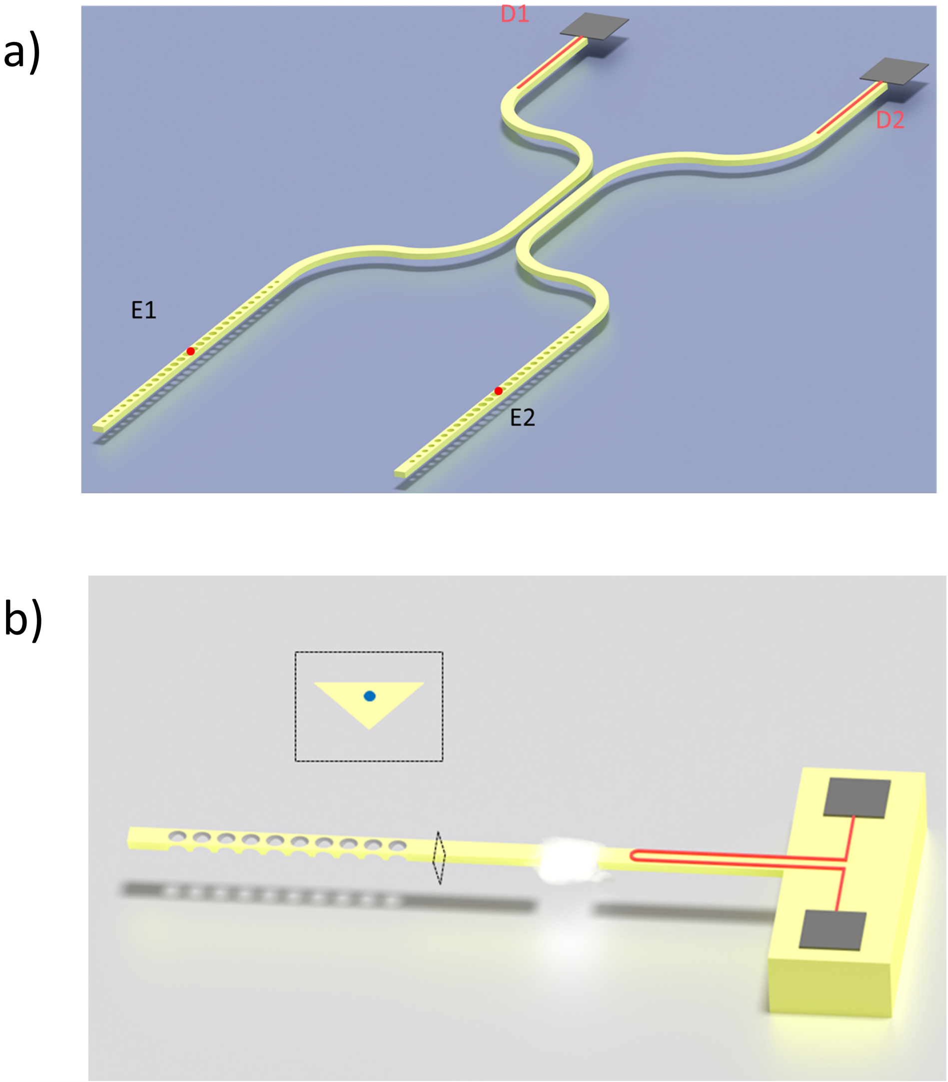

Figure 10.1: a) Perspective figure showing a concept of the on-chip realization of the HOM setup. Single color centers (E1, E2) are positioned at the center of an asymmetric cavity, resonant with the ZPL of the emitters. The emission into an asymmetric cavity preferentially propagates to one side coupling into the waveguide. The HOM interference occurs in the central region where the waveguide arms propagate in proximity mimicking a beam-splitter. The coincidence counts are measured using SNSPDs (D1, D2) that couple evanscently to the waveguide signal [137]. b)Illustration of SNSPD integrated onto a photonic device with a color center. Single color center is positioned in the waveguide region such that the dipole emission reflected by the photonic crystal mirror constructively interferes with the dipole emission into the waveguide region. The cloud region in the waveguide represents the segment where the pump light is filtered (e.g. by a ring oscillator or an inversely designed structure) to prevent any SNSPD saturation. Single photon detection is performed by the SNSPDs through absorption of the dipole emission in the waveguide. (Inset) The cross-section view of the structure, showing the color center (blue) optimally positioned at the centroid of the triangular waveguide profile. [131]

proton beam writing [88], and ion implantation on patterned substrates [89] should be explored. Improving single-photon detection efficiencies through coupling-efficient triangular waveguide-fiber designs [45] or integration of SNSPDs onto triangular photonics would further boost the success rate of these measurement protocols [115, 170]. Furthermore, color centers in 4H-SiC with emission wavelengths in the telecommunication bands should be studied for their ability to be sent over the existing fiber optic cable network over long distance with minimum losses.

Mesh photonics is a novel approach to quantum photonic circuits where numerous photonic components are interconnected in a mesh-like structure, offering the creation of large-scale quantum networks with synchronized operations. A wafer-scale nanofabrication process, discussed in this work, that can produce high-performance photonic components enables the fabrication of a large number of identical photonic systems on a scale previously unattainable.

Bibliography

[1] Yuriy Makhlin, Gerd Scöhn, and Alexander Shnirman. “Josephson-junction qubits with controlled couplings”. In: *nature* 398.6725 (1999), pp. 305–307.

[2] Denis Vion et al. “Manipulating the quantum state of an electrical circuit”. In: *Science* 296.5569 (2002), pp. 886–889.

[3] Andreas Wallraff et al. “Strong coupling of a single photon to a superconducting qubit using circuit quantum electrodynamics”. In: *Nature* 431.7005 (2004), pp. 162–167.

[4] David J Wineland et al. “Experimental issues in coherent quantum-state manipulation of trapped atomic ions”. In: *Journal of research of the National Institute of Standards and Technology* 103.3 (1998), p. 259.

[5] Chris Monroe et al. “Demonstration of a fundamental quantum logic gate”. In: *Physical review letters* 75.25 (1995), p. 4714.

[6] David Kielpinski et al. “A decoherence-free quantum memory using trapped ions”. In: *Science* 291.5506 (2001), pp. 1013–1015.

[7] K v Klitzing, Gerhard Dorda, and Michael Pepper. “New method for high-accuracy determination of the fine-structure constant based on quantized Hall resistance”. In: *Physical review letters* 45.6 (1980), p. 494.

[8] A Yu Kitaev. “Fault-tolerant quantum computation by anyons”. In: *Annals of physics* 303.1 (2003), pp. 2–30.

[9] Eytan Grosfeld and Ady Stern. “Observing Majorana bound states of Josephson vortices in topological superconductors”. In: *Proceedings of the National Academy of Sciences* 108.29 (2011), pp. 11810–11814.

[10] Nicholas C Harris et al. “Quantum transport simulations in a programmable nanophotonic processor”. In: *Nature Photonics* 11.7 (2017), pp. 447–452.

[11] Robert Stockill et al. “Phase-tuned entangled state generation between distant spin qubits”. In: *Physical Review Letters* 119.1 (2017), p. 010503.

[12] Natasha Tomm et al. “A bright and fast source of coherent single photons”. In: *Nature Nanotechnology* 16.4 (2021), pp. 399–403.

[13] Hannes Bernien et al. “Heralded entanglement between solid-state qubits separated by three metres”. In: *Nature* 497.7447 (2013), pp. 86–90.

[14] Bas Hensen et al. “Loophole-free Bell inequality violation using electron spins separated by 1.3 kilometres”. In: *Nature* 526.7575 (2015), pp. 682–686.

[15] Matteo Pompili et al. “Realization of a multinode quantum network of remote solid-state qubits”. In: *Science* 372.6539 (2021), pp. 259–264.

[16] MH Abobeih et al. “Fault-tolerant operation of a logical qubit in a diamond quantum processor”. In: *arXiv preprint arXiv:2108.01646* (2021).

[17] Mihir K Bhaskar et al. “Experimental demonstration of memory-enhanced quantum communication”. In: *Nature* 580.7801 (2020), pp. 60–64.

[18] CE Bradley et al. “A ten-qubit solid-state spin register with quantum memory up to one minute”. In: *Physical Review X* 9.3 (2019), p. 031045.

[19] SA Zargaleh et al. “Evidence for near-infrared photoluminescence of nitrogen vacancy centers in 4H-SiC”. In: *Physical Review B* 94.6 (2016), p. 060102.

[20] HJ Von Bardeleben et al. “Identification and magneto-optical properties of the NV center in 4H-SiC”. In: *Physical Review B* 92.6 (2015), p. 064104.

[21] Soroush Abbasi Zargaleh et al. “Nitrogen vacancy center in cubic silicon carbide: A promising qubit in the 1.5 μ m spectral range for photonic quantum networks”. In: *Physical Review B* 98.16 (2018), p. 165203.

[22] Kh Khazen et al. “High-resolution resonant excitation of NV centers in 6H-SiC: A matrix for quantum technology applications”. In: *Physical Review B* 100.20 (2019), p. 205202.

[23] Lukas Spindlberger et al. “Optical properties of vanadium in 4H silicon carbide for quantum technology”. In: *Physical Review Applied* 12.1 (2019), p. 014015.

[24] Gary Wolfowicz et al. “Vanadium spin qubits as telecom quantum emitters in silicon carbide”. In: *Science Advances* 6.18 (2020), eaaz1192.

[25] Naoya Morioka et al. “Spin-controlled generation of indistinguishable and distinguishable photons from silicon vacancy centres in silicon carbide”. In: *Nature Communications* 11.1 (2020), pp. 1–8.

[26] Wenzheng Dong, MW Doherty, and Sophia E Economou. “Spin polarization through intersystem crossing in the silicon vacancy of silicon carbide”. In: *Physical Review B* 99.18 (2019), p. 184102.

[27] Roland Nagy et al. “High-fidelity spin and optical control of single silicon-vacancy centres in silicon carbide”. In: *Nature Communications* 10.1 (2019), pp. 1–8.

[28] Ren-Zhou Fang et al. “Experimental Generation of Spin-Photon Entanglement in Silicon Carbide”. In: *arXiv preprint arXiv:2311.17455* (2023).

[29] Charles Babin et al. “Fabrication and nanophotonic waveguide integration of silicon carbide colour centres with preserved spin-optical coherence”. In: *Nature materials* 21.1 (2022), pp. 67–73.

[30] David J Christle et al. “Isolated spin qubits in SiC with a high-fidelity infrared spin-to-photon interface”. In: *Physical Review X* 7.2 (2017), p. 021046.

[31] Christopher P Anderson et al. “Five-second coherence of a single spin with single-shot readout in silicon carbide”. In: *arXiv preprint arXiv:2110.01590* (2021).

[32] Alexandre Bourassa et al. “Entanglement and control of single nuclear spins in isotopically engineered silicon carbide”. In: *Nature Materials* 19.12 (2020), pp. 1319–1325.

[33] Jun-Feng Wang et al. “Coherent control of nitrogen-vacancy center spins in silicon carbide at room temperature”. In: *Physical Review Letters* 124.22 (2020), p. 223601.

[34] Zhao Mu et al. “Coherent manipulation with resonant excitation and single emitter creation of nitrogen vacancy centers in 4H silicon carbide”. In: *Nano Letters* 20.8 (2020), pp. 6142–6147.

[35] Jun-Feng Wang et al. “Experimental optical properties of single nitrogen vacancy centers in silicon carbide at room temperature”. In: *ACS Photonics* 7.7 (2020), pp. 1611–1616.

[36] Fadis Murzakhanov et al. “Room temperature coherence properties and 14N nuclear spin readout of NV centers in 4H–SiC”. In: *Applied Physics Letters* 124.3 (2024).

[37] Jun-Feng Wang et al. “Experimental Optical Properties of Single Nitrogen Vacancy Centers in Silicon Carbide at Room Temperature”. In: *ACS Photonics* 7.7 (2020), pp. 1611–1616.

[38] David O Bracher, Xingyu Zhang, and Evelyn L Hu. “Selective Purcell enhancement of two closely linked zero-phonon transitions of a silicon carbide color center”. In: *Proceedings of the National Academy of Sciences* 114.16 (2017), pp. 4060–4065.

[39] Alexander L Crook et al. “Purcell enhancement of a single silicon carbide color center with coherent spin control”. In: *Nano Letters* 20.5 (2020), pp. 3427–3434.

[40] Daniil M Lukin et al. “4H-silicon-carbide-on-insulator for integrated quantum and nonlinear photonics”. In: *Nature Photonics* 14.5 (2020), pp. 330–334.

[41] Greg Calusine, Alberto Politi, and David D Awschalom. "Silicon carbide photonic crystal cavities with integrated color centers". In: *Applied Physics Letters* 105.1 (2014), p. 011123.

[42] Greg Calusine, Alberto Politi, and David D Awschalom. "Cavity-enhanced measurements of defect spins in silicon carbide". In: *Physical Review Applied* 6.1 (2016), p. 014019.

[43] Michael J Burek et al. "Free-standing mechanical and photonic nanostructures in single-crystal diamond". In: *Nano Letters* 12.12 (2012), pp. 6084–6089.

[44] Bong-Shik Song et al. "High-Q-factor nanobeam photonic crystal cavities in bulk silicon carbide". In: *Applied Physics Letters* 113.23 (2018), p. 231106.

[45] Marcel Krumrein et al. "Precise characterization of a silicon carbide waveguide fiber interface". In: *arXiv preprint arXiv:2401.06096* (2024).

[46] Haig A Atikian et al. "Freestanding nanostructures via reactive ion beam angled etching". In: *APL Photonics* 2.5 (2017), p. 051301.

[47] Hosung Seo et al. "Quantum decoherence dynamics of divacancy spins in silicon carbide". In: *Nature Communications* 7.1 (2016), pp. 1–9.

[48] Sen Yang et al. "High-fidelity transfer and storage of photon states in a single nuclear spin". In: *Nature Photonics* 10.8 (2016), pp. 507–511.

[49] P Neumann et al. "Multipartite entanglement among single spins in diamond". In: *Science* 320.5881 (2008), pp. 1326–1329.

[50] E Sörman et al. "Silicon vacancy related defect in 4H and 6H SiC". In: *Physical Review B* 61.4 (2000), p. 2613.

[51] Erik Janzén et al. "The silicon vacancy in SiC". In: *Physica B: Condensed Matter* 404.22 (2009), pp. 4354–4358.

[52] Charles Babin et al. "Fabrication and nanophotonic waveguide integration of silicon carbide colour centres with preserved spin-optical coherence". In: *Nature Materials* 21.1 (2022), pp. 67–73.

[53] William F Koehl et al. “Room temperature coherent control of defect spin qubits in silicon carbide”. In: *Nature* 479.7371 (2011), pp. 84–87.

[54] NT Son et al. “Photoluminescence and Zeeman effect in chromium-doped 4H and 6H SiC”. In: *Journal of Applied Physics* 86.8 (1999), pp. 4348–4353.

[55] William F Koehl et al. “Resonant optical spectroscopy and coherent control of Cr^{4+} spin ensembles in SiC and GaN”. In: *Physical Review B* 95.3 (2017), p. 035207.

[56] Berk Diler et al. “Coherent control and high-fidelity readout of chromium ions in commercial silicon carbide”. In: *npj Quantum Information* 6.1 (2020), pp. 1–6.

[57] Andreas Gällström, Björn Magnusson, and Erik Janzén. “Optical identification of Mo related deep level defect in 4H and 6H SiC”. In: *Materials Science Forum*. Vol. 615. Trans Tech Publ. 2009, pp. 405–408.

[58] Tom Bosma et al. “Identification and tunable optical coherent control of transition-metal spins in silicon carbide”. In: *npj Quantum Information* 4.1 (2018), pp. 1–7.

[59] Carmem M Gilardoni et al. “Spin-relaxation times exceeding seconds for color centers with strong spin–orbit coupling in SiC”. In: *New Journal of Physics* 22.10 (2020), p. 103051.

[60] Marina Radulaski et al. “Scalable quantum photonics with single color centers in silicon carbide”. In: *Nano Letters* 17.3 (2017), pp. 1782–1786.

[61] Melissa A Guidry et al. “Optical parametric oscillation in silicon carbide nanophotonics”. In: *Optica* 7.9 (2020), pp. 1139–1142.

[62] Matthias Widmann et al. “Coherent control of single spins in silicon carbide at room temperature”. In: *Nature Materials* 14.2 (2015), pp. 164–168.

[63] F Sardi et al. “Scalable production of solid-immersion lenses for quantum emitters in silicon carbide”. In: *Applied Physics Letters* 117.2 (2020), p. 022105.

[64] RA Parker et al. “Infrared erbium photoluminescence enhancement in silicon carbide nano-pillars”. In: *Journal of Applied Physics* 130.14 (2021), p. 145101.

[65] Erika Janitz, Mihir K Bhaskar, and Lilian Childress. “Cavity quantum electrodynamics with color centers in diamond”. In: *Optica* 7.10 (2020), pp. 1232–1252.

[66] Johannes Borregaard, Anders Søndberg Sørensen, and Peter Lodahl. “Quantum networks with deterministic spin–photon interfaces”. In: *Advanced Quantum Technologies* 2.5-6 (2019), p. 1800091.

[67] Andreas Reiserer and Gerhard Rempe. “Cavity-based quantum networks with single atoms and optical photons”. In: *Reviews of Modern Physics* 87.4 (2015), p. 1379.

[68] I Diniz et al. “Strongly coupling a cavity to inhomogeneous ensembles of emitters: Potential for long-lived solid-state quantum memories”. In: *Physical Review A* 84.6 (2011), p. 063810.

[69] Winnie N Ye and Yule Xiong. “Review of silicon photonics: history and recent advances”. In: *Journal of Modern Optics* 60.16 (2013), pp. 1299–1320.

[70] Robin Karhu et al. “CVD growth and properties of on-axis vanadium doped semi-insulating 4H-SiC epilayers”. In: *Journal of Applied Physics* 125.4 (2019), p. 045702.

[71] Gabriel Ferro. “3C-SiC heteroepitaxial growth on silicon: the quest for holy grail”. In: *Critical Reviews in Solid State and Materials Sciences* 40.1 (2015), pp. 56–76.

[72] David O Bracher, Xingyu Zhang, and Evelyn L Hu. “Selective Purcell enhancement of two closely linked zero-phonon transitions of a silicon carbide color center”. In: *Proceedings of the National Academy of Sciences* 114.16 (2017), pp. 4060–4065.

[73] C. T. Nguyen et al. “Quantum Network Nodes Based on Diamond Qubits with an Efficient Nanophotonic Interface”. In: *Phys. Rev. Lett.* 123 (18 Oct. 2019), p. 183602. DOI: `10.1103/PhysRevLett.123.183602`. URL: `https://link.aps.org/doi/10.1103/PhysRevLett.123.183602`.

[74] P.-J. Stas et al. “Robust multi-qubit quantum network node with integrated error detection”. In: *Science* 378.6619 (2022), pp. 557–560. DOI: `10.1126/science.add9771`. eprint: `https://www.science.org/doi/pdf/10.1126/science.add9771`. URL: `https://www.science.org/doi/abs/10.1126/science.add9771`.

[75] C. T. Nguyen et al. “An integrated nanophotonic quantum register based on silicon-vacancy spins in diamond”. In: *Phys. Rev. B* 100 (16 Oct. 2019), p. 165428. DOI: `10.1103/PhysRevB.100.165428`. URL: `https://link.aps.org/doi/10.1103/PhysRevB.100.165428`.

[76] E. N. Knall et al. “Efficient Source of Shaped Single Photons Based on an Integrated Diamond Nanophotonic System”. In: *Phys. Rev. Lett.* 129 (5 July 2022), p. 053603. DOI: `10.1103/PhysRevLett.129.053603`. URL: `https://link.aps.org/doi/10.1103/PhysRevLett.129.053603`.

[77] Beibei Zeng et al. “Cryogenic packaging of nanophotonic devices with a low coupling loss <1 dB”. In: *Applied Physics Letters* 123.16 (Oct. 2023), p. 161106. ISSN: 0003-6951. DOI: `10.1063/5.0170324`. eprint: `https://pubs.aip.org/aip/apl/article-pdf/doi/10.1063/5.0170324/18171283/161106\_1\_5.0170324.pdf`. URL: `https://doi.org/10.1063/5.0170324`.

[78] B. Machielse et al. “Quantum Interference of Electromechanically Stabilized Emitters in Nanophotonic Devices”. In: *Phys. Rev. X* 9 (3 Aug. 2019), p. 031022. DOI: `10.1103/PhysRevX.9.031022`. URL: `https://link.aps.org/doi/10.1103/PhysRevX.9.031022`.

[79] D. R. Assumpcao et al. “Deterministic creation of strained color centers in nanostructures via high-stress thin films”. In: *Applied Physics Letters* 123.24 (Dec. 2023), p. 244001. ISSN: 0003-6951. DOI: `10.1063/5.0171558`. eprint: `https://pubs.aip.org/aip/apl/article-pdf/doi/10.1063/5.0171558/18253176/244001\_1\_5.0171558.pdf`. URL: `https://doi.org/10.1063/5.0171558`.

[80] Eric Bersin et al. "Telecom Networking with a Diamond Quantum Memory". In: *PRX Quantum* 5 (1 Jan. 2024), p. 010303. DOI: `10.1103/PRXQuantum.5.010303`. URL: `https://link.aps.org/doi/10.1103/PRXQuantum.5.010303`.

[81] Kane Yee. "Numerical solution of initial boundary value problems involving Maxwell's equations in isotropic media". In: *IEEE Transactions on antennas and propagation* 14.3 (1966), pp. 302–307.

[82] Allen Taflove and Morris E Brodwin. "Numerical solution of steady-state electromagnetic scattering problems using the time-dependent Maxwell's equations". In: *IEEE transactions on microwave theory and techniques* 23.8 (1975), pp. 623–630.

[83] M Gurfinkel et al. "Ion implantation and SiC transistor performance". In: *Journal of Applied Physics* 105.8 (2009), p. 084511.

[84] Junfeng Wang et al. "Scalable fabrication of single silicon vacancy defect arrays in silicon carbide using focused ion beam". In: *ACS Photonics* 4.5 (2017), pp. 1054–1059.

[85] Aaron M Day et al. "Laser writing of spin defects in nanophotonic cavities". In: *Nature Materials* (2023), pp. 1–7.

[86] Yu-Chen Chen et al. "Laser writing of scalable single color centers in silicon carbide". In: *Nano Letters* 19.4 (2019), pp. 2377–2383.

[87] AFM Almutairi et al. "Direct writing of divacancy centers in silicon carbide by femtosecond laser irradiation and subsequent thermal annealing". In: *Applied Physics Letters* 120.1 (2022), p. 014003.

[88] H Kraus et al. "Three-dimensional proton beam writing of optically active coherent vacancy spins in silicon carbide". In: *Nano Letters* 17.5 (2017), pp. 2865–2870.

[89] Junfeng Wang et al. "Efficient generation of an array of single silicon-vacancy defects in silicon carbide". In: *Physical Review Applied* 7.6 (2017), p. 064021.

[90] James F Ziegler, Matthias D Ziegler, and Jochen P Biersack. “SRIM–The stopping and range of ions in matter (2010)”. In: *Nuclear Instruments and Methods in Physics Research Section B: Beam Interactions with Materials and Atoms* 268.11-12 (2010), pp. 1818–1823.

[91] FA Khan and I Adesida. “High rate etching of SiC using inductively coupled plasma reactive ion etching in SF 6-based gas mixtures”. In: *Applied physics letters* 75.15 (1999), pp. 2268–2270.

[92] JH Choi et al. “Fabrication of SiC nanopillars by inductively coupled SF_6/O_2 plasma etching”. In: *Journal of Physics D: Applied Physics* 45.23 (2012), p. 235204.

[93] Karen M Dowling, Elliot H Ransom, and Debbie G Senesky. “Profile evolution of high aspect ratio silicon carbide trenches by inductive coupled plasma etching”. In: *Journal of Microelectromechanical Systems* 26.1 (2016), pp. 135–142.

[94] Katarzyna Racka-Szmidt et al. “A review: Inductively coupled plasma reactive ion etching of silicon carbide”. In: *Materials* 15.1 (2021), p. 123.

[95] Harold R Kaufman. *Applications of Broad-Beam Ion Sources: An Introduction.* Kaufman & Robinson, 2011.

[96] Haig Avedis Atikian. “Diamond Based Optical Components for High Power Laser Applications”. PhD thesis. Harvard University, 2017.

[97] Randy J Shul and Stephen J Pearton. *Handbook of advanced plasma processing techniques.* Springer Science & Business Media, 2011.

[98] Victoria A Norman et al. “ICECAP: a 3-in-1 integrated cryogenic system for emission, collection and photon-detection from near infrared quantum nanophotonic devices”. In: *arXiv preprint arXiv:2401.10509* (2024).

[99] Sridhar Majety et al. “Quantum photonics in triangular-cross-section nanodevices in silicon carbide”. In: *Journal of Physics: Photonics* 3.3 (2021), p. 034008.

[100] Qimin Quan and Marko Loncar. “Deterministic design of wavelength scale, ultra-high Q photonic crystal nanobeam cavities”. In: *Optics Express* 19.19 (2011), pp. 18529–18542.

[101] Michael J Burek et al. “High quality-factor optical nanocavities in bulk single-crystal diamond”. In: *Nature Communications* 5.1 (2014), pp. 1–7.

[102] Sonia Buckley et al. “Nonlinear frequency conversion using high-quality modes in GaAs nanobeam cavities”. In: *Optics Letters* 39.19 (2014), pp. 5673–5676.

[103] Sonia Buckley et al. “Second-harmonic generation in GaAs photonic crystal cavities in (111)B and (001) crystal orientations”. In: *ACS Photonics* 1.6 (2014), pp. 516–523.

[104] Shota Yamada et al. “Second-harmonic generation in a silicon-carbide-based photonic crystal nanocavity”. In: *Optics Letters* 39.7 (2014), pp. 1768–1771.

[105] Bong-Shik Song et al. “Demonstration of two-dimensional photonic crystals based on silicon carbide”. In: *Optics Express* 19.12 (2011), pp. 11084–11089.

[106] Marina Radulaski et al. “Photonic crystal cavities in cubic (3C) polytype silicon carbide films”. In: *Optics Express* 21.26 (2013), pp. 32623–32629.

[107] Bong-Shik Song et al. “Ultrahigh-Q photonic crystal nanocavities based on 4H silicon carbide”. In: *Optica* 6.8 (2019), pp. 991–995.

[108] David O Bracher and Evelyn L Hu. “Fabrication of high-Q nanobeam photonic crystals in epitaxially grown 4H-SiC”. In: *Nano Letters* 15.9 (2015), pp. 6202–6207.

[109] Shota Yamada et al. “Suppression of multiple photon absorption in a SiC photonic crystal nanocavity operating at 1.55 μm”. In: *Optics Express* 20.14 (2012), pp. 14789–14796.

[110] Jonathan Y Lee, Xiyuan Lu, and Qiang Lin. “High-Q silicon carbide photonic-crystal cavities”. In: *Applied Physics Letters* 106.4 (2015), p. 041106.

[111] Ioannis Chatzopoulos et al. “High-Q/V photonic crystal cavities and QED analysis in 3C-SiC”. In: *ACS Photonics* 6.8 (2019), pp. 1826–1831.

[112] Kirill A Atlasov et al. “Wavelength and loss splitting in directly coupled photonic-crystal defect microcavities”. In: *Optics Express* 16.20 (2008), pp. 16255–16264.

[113] Arka Majumdar et al. “Cavity quantum electrodynamics with a single quantum dot coupled to a photonic molecule”. In: *Physical Review B* 86.4 (2012), p. 045315.

[114] Michael J Burek et al. “Fiber-coupled diamond quantum nanophotonic interface”. In: *Physical Review Applied* 8.2 (2017), p. 024026.

[115] F Martini et al. “Single photon detection with superconducting nanowires on crystalline silicon carbide”. In: *Optics Express* 27.21 (2019), pp. 29669–29675.

[116] Koji Azuma, Kiyoshi Tamaki, and Hoi-Kwong Lo. “All-photonic quantum repeaters”. In: *Nature Communications* 6.1 (2015), pp. 1–7.

[117] Robert Raussendorf and Hans J Briegel. “A one-way quantum computer”. In: *Physical Review Letters* 86.22 (2001), p. 5188.

[118] Sophia E Economou and Pratibha Dev. “Spin-photon entanglement interfaces in silicon carbide defect centers”. In: *Nanotechnology* 27.50 (2016), p. 504001.

[119] M.J. Hartmann, F.G.S.L. Brandão, and M.B. Plenio. “Quantum many-body phenomena in coupled cavity arrays”. In: *Laser & Photonics Reviews* 2.6 (2008), pp. 527–556. DOI: `https://doi.org/10.1002/lpor.200810046`. eprint: `https://onlinelibrary.wiley.com/doi/pdf/10.1002/lpor.200810046`. URL: `https://onlinelibrary.wiley.com/doi/abs/10.1002/lpor.200810046`.

[120] Nikos Fayard et al. “Many-body localization in waveguide QED”. In: *arXiv preprint arXiv:2101.01645* (2021).

[121] Bryan A Myers et al. “Probing surface noise with depth-calibrated spins in diamond”. In: *Physical Review Letters* 113.2 (2014), p. 027602.

[122] Sorawis Sangtawesin et al. “Origins of diamond surface noise probed by correlating single-spin measurements with surface spectroscopy”. In: *Physical Review X* 9.3 (2019), p. 031052.

[123] Daniel Riedel et al. "Deterministic enhancement of coherent photon generation from a nitrogen-vacancy center in ultrapure diamond". In: *Physical Review X* 7.3 (2017), p. 031040.

[124] Maximilian Ruf et al. "Resonant excitation and purcell enhancement of coherent nitrogen-vacancy centers coupled to a Fabry-Perot microcavity". In: *Physical Review Applied* 15.2 (2021), p. 024049.

[125] Yiwen Chu et al. "Coherent optical transitions in implanted nitrogen vacancy centers". In: *Nano letters* 14.4 (2014), pp. 1982–1986.

[126] Péter Udvarhelyi et al. "Spectrally stable defect qubits with no inversion symmetry for robust spin-to-photon interface". In: *Physical Review Applied* 11.4 (2019), p. 044022.

[127] Péter Udvarhelyi et al. "Vibronic states and their effect on the temperature and strain dependence of silicon-vacancy qubits in 4H-SiC". In: *Physical Review Applied* 13.5 (2020), p. 054017.

[128] D Simin et al. "Locking of electron spin coherence above 20 ms in natural silicon carbide". In: *Physical Review B* 95.16 (2017), p. 161201.

[129] Carlo Bradac et al. "Quantum nanophotonics with group IV defects in diamond". In: *Nature communications* 10.1 (2019), p. 5625.

[130] CT Nguyen et al. "Quantum network nodes based on diamond qubits with an efficient nanophotonic interface". In: *Physical review letters* 123.18 (2019), p. 183602.

[131] Sridhar Majety et al. "Triangular quantum photonic devices with integrated detectors in silicon carbide". In: *Materials for Quantum Technology* 3.1 (2023), p. 015004.

[132] John D Joannopoulos, Pierre R Villeneuve, and Shanhui Fan. "Photonic crystals: putting a new twist on light". In: *Nature* 386.6621 (1997), pp. 143–149.

[133] Steven G Johnson et al. "Guided modes in photonic crystal slabs". In: *Physical Review B* 60.8 (1999), p. 5751.

[134] Masaya Notomi, E Kuramochi, and H Taniyama. “Ultrahigh-Q nanocavity with 1D photonic gap”. In: *Optics Express* 16.15 (2008), pp. 11095–11102.

[135] Lijun Huang et al. “Photonic crystal elliptical-hole tapered low-index-mode nanobeam cavities for sensing”. In: *Applied Optics* 57.33 (2018), pp. 9822–9827.

[136] Michael J Burek et al. “High quality-factor optical nanocavities in bulk single-crystal diamond”. In: *Nature Communications* 5.1 (2014), pp. 1–7.

[137] Sridhar Majety et al. “Quantum information processing with integrated silicon carbide photonics”. In: *Journal of Applied Physics* 131.13 (2022).

[138] Pranta Saha, Sridhar Majety, and Marina Radulaski. “Utilizing photonic band gap in triangular silicon carbide structures for efficient quantum nanophotonic hardware”. In: *Scientific Reports* 13.1 (2023), p. 4112.

[139] Roshidah Yusof et al. “Comparative studies of rib waveguide material for quantum communication application”. In: *IOP Conference Series: Materials Science and Engineering* 551.1 (2019), p. 012018.

[140] Marc Westig et al. “Analysis of a single-mode waveguide at sub-terahertz frequencies as a communication channel”. In: *AIP Advances* 10.1 (2020), p. 015008.

[141] Deyin Zhao et al. “Polarization independent broadband reflectors based on cross-stacked gratings”. In: *Optics Express* 19.10 (2011), pp. 9050–9055.

[142] Rongzhou Wang et al. “Effects of shapes and orientations of scatterers and lattice symmetries on the photonic band gap in two-dimensional photonic crystals”. In: *Journal of Applied Physics* 90.9 (2001), pp. 4307–4313.

[143] N Aravantinos-Zafiris et al. “Phononic crystals and elastodynamics: Some relevant points”. In: *AIP Advances* 4.12 (2014), p. 124203.

[144] G. Gol’Tsman et al. “Fabrication and properties of an ultrafast NbN hot-electron single-photon detector”. In: *IEEE Transactions on Applied Superconductivity*. Vol. 11. Mar. 2001, pp. 574–577. DOI: `10.1109/77.919410`. URL: `http://ieeexplore.ieee.org/document/919410/`.

[145] Boris Korzh et al. "Demonstration of sub-3 ps temporal resolution with a superconducting nanowire single-photon detector". In: *Nature Photonics* 14.4 (2020), pp. 250–255. ISSN: 17494893. DOI: `10.1038/s41566-020-0589-x`. URL: `http://dx.doi.org/10.1038/s41566-020-0589-x`.

[146] Hiroyuki Shibata et al. "Ultimate low system dark-count rate for superconducting nanowire single-photon detector". In: *Optics Letters* 40.14 (2015), p. 3428. ISSN: 0146-9592. DOI: `10.1364/ol.40.003428`.

[147] Dileep V. Reddy et al. "Superconducting nanowire single-photon detectors with 98% system detection efficiency at 1550 nm". In: *Optica* 7.12 (2020), p. 1649. ISSN: 2334-2536. DOI: `10.1364/optica.400751`.

[148] Iman Esmaeil Zadeh et al. "Superconducting nanowire single-photon detectors: A perspective on evolution, state-of-the-art, future developments, and applications". In: *Applied Physics Letters* 118.19 (2021).

[149] Lixing You. "Superconducting nanowire single-photon detectors for quantum information". In: *Nanophotonics* 9.9 (2020), pp. 2673–2692. ISSN: 21928614. DOI: `10.1515/nanoph-2020-0186`.

[150] Tomas Polakovic et al. "Unconventional applications of superconducting nanowire single photon detectors". In: *Nanomaterials* 10.6 (2020), pp. 1–20. ISSN: 20794991. DOI: `10.3390/nano10061198`.

[151] F. Marsili et al. "Detecting single infrared photons with 93% system efficiency". In: *Nature Photonics* 7.3 (2013), pp. 210–214. ISSN: 17494885. DOI: `10.1038/nphoton.2013.13`. URL: `http://dx.doi.org/10.1038/nphoton.2013.13`.

[152] L. Redaelli et al. "Design of broadband high-efficiency superconducting-nanowire single photon detectors". In: *Superconductor Science and Technology* 29.6 (2016), pp. 1–10. ISSN: 13616668. DOI: `10.1088/0953-2048/29/6/065016`. URL: `http://dx.doi.org/10.1088/0953-2048/29/6/065016`.

[153] G. Reithmaier et al. "On-chip time resolved detection of quantum dot emission using integrated superconducting single photon detectors". In: *Scientific Reports* 3 (2013), pp. 1–6. ISSN: 20452322. DOI: `10.1038/srep01901`.

[154] *Waveguide-integrated superconducting nanowire single-photon detectors*. Sept. 2018. DOI: `10.1515/nanoph-2018-0059`. URL: `http://www.degruyter.com/view/j/nanoph.2018.7.issue-11/nanoph-2018-0059/nanoph-2018-0059.xml%20https://www.degruyter.com/view/journals/nanoph/7/11/article-p1725.xml`.

[155] M. Hofherr et al. "Intrinsic detection efficiency of superconducting nanowire single-photon detectors with different thicknesses". In: *Journal of Applied Physics* 108.1 (2010). ISSN: 00218979. DOI: `10.1063/1.3437043`.

[156] Faraz Najafi et al. "On-chip detection of non-classical light by scalable integration of single-photon detectors". In: *Nature Communications* 6.1 (2015), pp. 1–8.

[157] Ryan Hamerly, Saumil Bandyopadhyay, and Dirk Englund. "Asymptotically fault-tolerant programmable photonics". In: *Nature Communications* 13.1 (2022), p. 6831.

[158] Mark Dong et al. "Programmable photonic integrated meshes for modular generation of optical entanglement links". In: *npj Quantum Information* 9.1 (2023), p. 42.

[159] Wim Bogaerts et al. "Programmable photonic circuits". In: *Nature* 586.7828 (2020), pp. 207–216.

[160] Samuel Gyger et al. "Reconfigurable photonics with on-chip single-photon detectors". In: *Nature Communications* 12.1 (2021), p. 1408.

[161] Michael Reck et al. "Experimental realization of any discrete unitary operator". In: *Physical Review Letters* 73.1 (1994), p. 58.

[162] Emanuel Knill, Raymond Laflamme, and Gerald J Milburn. "A scheme for efficient quantum computation with linear optics". In: *Nature* 409.6816 (2001), pp. 46–52.

[163] Yuting Xu et al. "Methods and applications of on-chip beam splitting: A review". In: *Frontiers in Physics* 10 (2022), p. 985208.

[164] Sridhar Majety et al. "Triangular Cross-Section Beam Splitters in Silicon Carbide for Quantum Information Processing". In: *arXiv preprint arXiv:2311.07845* (2023).

[165] Carlton M Caves and Peter D Drummond. "Quantum limits on bosonic communication rates". In: *Reviews of Modern Physics* 66.2 (1994), p. 481.

[166] Wu Yuan, Graham E Town, and Ole Bang. "Refractive index sensing in an all-solid twin-core photonic bandgap fiber". In: *IEEE Sensors Journal* 10.7 (2010), pp. 1192–1199.

[167] Long Zhang et al. "Ultrahigh-Q silicon racetrack resonators". In: *Photonics Research* 8.5 (2020), pp. 684–689.

[168] Abram L Falk et al. "Polytype control of spin qubits in silicon carbide". In: *Nature Communications* 4.1 (2013), p. 1819.

[169] Stefania Castelletto et al. "Advances in diamond nanofabrication for ultrasensitive devices". In: *Microsystems & nanoengineering* 3.1 (2017), pp. 1–16.

[170] F Martini et al. "Electro-optical Characterization of Superconducting Nanowire Single-Photon Detectors Fabricated on 3C Silicon Carbide". In: *Journal of Low Temperature Physics* 199.1 (2020), pp. 563–568.